

MULTISCALE MODEL REDUCTION FOR HIGH-CONTRAST FLOW
PROBLEMS

A Dissertation
by
GUANGLIAN LI

Submitted to the Office of Graduate and Professional Studies of
Texas A&M University
in partial fulfillment of the requirements for the degree of
DOCTOR OF PHILOSOPHY

Chair of Committee,	Yalchin Efendiev
Co-Chair of Committee,	Partha Mukherjee
Committee Members,	Raytcho Lazarov
	Jianxian Zhou
Head of Department,	Emil Straube

May 2015

Major Subject: Mathematics

Copyright 2015 Guanglian Li

ABSTRACT

Many applications involve media that contain multiple scales and physical properties that vary in orders of magnitude. One example is a rock sample, which has many micro-scale features. Most multiscale problems are often parameter-dependent, where the parameters represent variations in medium properties, randomness, or spatial heterogeneities. Because of disparity of scales in multiscale problems, solving such problems is prohibitively expensive.

Among the most popular and developed techniques for efficiently solving the global system arising from a finite element approximation of the underlying problem on a very fine mesh are multigrid methods, multilevel methods, and domain decomposition techniques. More recently, a new large class of accurate reduced-order methods has been introduced and used in various applications. These include Galerkin multiscale finite element methods, mixed multiscale finite element methods, multiscale finite volume methods, and mortar multiscale methods, and so on.

In this dissertation, a multiscale finite element method is studied for the computation of heterogeneous problems involving high-contrast, no-scale separation, parameter dependency and nonlinearities. A general formulation of the elliptic heterogeneous problems is discussed, including an oversampling strategy and randomized snapshots generation for a more efficient and accurate computation. Furthermore, a multiscale adaptive algorithm is proposed and analyzed to reduce the computational cost. Then, this multiscale finite element method is extended to the nonlinear high-contrast elliptic problems. Specifically, both continuous and discontinuous Galerkin formulations are considered. In the end, an application to high-contrast heterogeneous Brinkman flow is analyzed.

ACKNOWLEDGEMENTS

I owe my deepest gratitude to the Department of Mathematics, Texas A&M University. Without the generous financial support at the beginning of my graduate study, I would have no chance to pursue my doctorate degree here. Besides, I also thank the Department of Mathematics for providing me the opportunity to meet lots of mathematicians, who have helped and influenced me enormously over the past four years, especially my advisor, Dr. Yalchin Efendiev.

I am extremely fortunate to have Dr. Yalchin Efendiev as my advisor. During my graduate study in Texas A&M University, he has tried his best to help me with my research and study. He serves as a role model for me to follow, especially the way he treats junior researchers. I am also grateful to him for the chances of attending workshops and conferences informed and supported by him.

I would also like to thank Dr. Eric T. Chung, Dr. Raytcho Lazarov, Dr. Partha Mukherjee and Dr. Jianxin Zhou for taking time either serving as my committee or letter writer.

Besides, many thanks go to Dr. Donald Brown, Dr. Juan Galvis, Dr. Michael Prescho and Dr. Ke Shi. They have offered me lots of help during my study and research, and provided me with all kinds of information in our field. Also many thanks to our group and classmates for inspiring and encouraging me.

Last but not least, I want to thank my husband Bangti for his unconditional support and love. I also owe my sister and brother for taking care of my mom while I am not around.

Guanglian Li

April 30, 2015

TABLE OF CONTENTS

	Page
ABSTRACT	ii
ACKNOWLEDGEMENTS	iii
TABLE OF CONTENTS	iv
LIST OF FIGURES	vi
LIST OF TABLES	viii
I. INTRODUCTION	1
I.1 Motivation	1
I.2 Outline of the dissertation	2
II. GENERALIZED MULTISCALE FINITE ELEMENT METHODS. ELLIP- TIC PROBLEMS	5
II.1 Introduction	5
II.2 Preliminaries	8
II.3 Local basis functions	10
II.3.1 Snapshot space	10
II.3.2 Offline space	13
II.3.3 Online space	17
II.4 Global coupling	19
II.5 Discussion on complexity	21
II.6 Randomized snapshot. Efficient calculation of snapshot	22
II.7 Concluding remarks	26
III. ADAPTIVITY FOR GENERALIZED MULTISCALE FINITE ELEMENT METHODS. ELLIPTIC PROBLEMS	27
III.1 Introduction	27
III.2 Preliminaries	29
III.3 A posteriori error estimate and adaptive enrichment	30
III.4 Discussion on complexity	36
III.5 Numerical results	37

III.5.1	Numerical results with harmonic basis	41
III.5.2	Numerical results with spectral basis	45
III.5.3	Numerical results with the L^2 indicator	49
III.5.4	Numerical results using snapshot solutions for the proposed indicator	51
III.6	Convergence analysis	52
III.6.1	Proof of Theorem III.3.1	52
III.6.2	Some auxiliary lemmas	54
III.6.3	Proof of Theorem III.3.3	62
III.7	Concluding remarks	67
IV.	GENERALIZED MULTISCALE FINITE ELEMENT METHODS. NON- LINEAR ELLIPTIC PROBLEMS	68
IV.1	Introduction	68
IV.2	Preliminaries	71
IV.3	CG and DG GMsFEM for nonlinear problems	72
IV.3.1	Local basis functions	72
IV.3.2	Global coupling	73
IV.4	Numerical Results	78
IV.4.1	Parameter-independent permeability field	80
IV.4.2	Parameter-dependent permeability field	88
IV.5	Concluding remarks	90
V.	GENERALIZED MULTISCALE FINITE ELEMENT METHODS. BRINKMAN FLOW	92
V.1	Introduction	92
V.2	Preliminaries	93
V.3	The construction of the space V^{off}	98
V.4	Numerical results	104
V.5	Convergence analysis	109
V.5.1	Stability argument	110
V.5.2	Convergence results	116
V.6	Concluding remarks	122
VI.	CONCLUSIONS	125
	REFERENCES	126

LIST OF FIGURES

FIGURE	Page
II.1 Local snapshot	6
II.2 Decomposition of permeability field	8
II.3 Illustration of a coarse neighborhood and oversampled domain	10
II.4 Permeability fields	15
II.5 Eigenvalue decay on log-scale against the number of eigenvalues. x-axis indicates the number of eigenvalue and y-axis indicates the inverse of the eigenvalue (on log-scale)	16
II.6 Schematic description of basis function construction. Left: subdomain ω_i . Right-Top: Selected eigenvector ψ_i^ℓ corresponding to small eigenvalue. Right-Bottom: product $\chi_i \psi_i^\ell$ where χ_i is the initial basis function of node i	19
II.7 The fine-scale solution and coarse-scale solutions correspond to Figure II.4(b).	26
III.1 Dimension distributions of the last offline space for harmonic basis with permeability field II.4(b).	44
III.2 Dimension distributions of the last offline space for spectral basis with permeability field II.4(b).	48
III.3 Basis distribution and error distribution for harmonic basis with L^2 indicator.	50
IV.1 High-contrast permeability fields	78
IV.2 Decomposition of permeability field IV.1(b)	80
IV.3 Comparison of fine and coarse CG solutions corresponding to Figure IV.1(b)	84

IV.4	Relation between the first discarded eigenvalue and the CG relative energy error; permeability from Figure IV.1(a) (left), permeability from Figure IV.1(b) (right)	84
IV.5	Comparison of fine and coarse DG solutions corresponding to Figure IV.1(b)	87
IV.6	Relation between the first discarded eigenvalue and the DG relative interior energy error; permeability from Figure IV.1(a) (left), permeability from Figure IV.1(b) (right) IV.1(a) and IV.1(b)	87
V.1	Illustration of three types of coarse neighborhoods and coarse element: ω_1 , ω_2 and ω_3 denote the support of partition of unity functions χ .	99
V.2	Four representative inverse permeability fields κ^{-1} .	105
V.3	The fine-scale solution and three coarse-scale solutions with different dimensions of coarse spaces using the inverse permeability field κ^{-1} in Figure V.2 (b).	106

LIST OF TABLES

TABLE	Page
II.1 Randomized GMsFEM Algorithm	23
II.2 Numerical results comparing the results between using all harmonic snapshots and the snapshots generated by random boundary conditions with $p_{\text{bf}} = 4$, κ as shown in Figure II.4(b). In the parenthesis, we show a higher value of the snapshot ratio.	25
III.1 Convergence history for harmonic basis with $\theta = 0.7$ and 18 iterations. The snapshot space has dimension 7300 giving 0.05% and 3.02% weighted L^2 and weighted energy errors. When using 12 basis per coarse inner node, the weighted L^2 and the weighted H^1 errors will be 2.34% and 19.77%, respectively, and the dimension of offline space is 4412.	42
III.2 Convergence history for harmonic basis with $\theta = 0.2$. The number of iterations is 66. The snapshot space has dimension 7300 giving 0.05% and 3.02% weighted L^2 and weighted energy errors. When using 12 basis per coarse inner node, the weighted L^2 and the weighted H^1 errors will be 2.34% and 19.77%, respectively, and the dimension of offline space is 4412.	42
III.3 Convergence history for harmonic basis with $\theta = 0.7$ and the exact indicator. The number of iterations is 23. The snapshot space has dimension 7300 giving 0.05% and 3.02% weighted L^2 and weighted energy errors.	43
III.4 Coarse-grid energy error distribution using harmonic basis with permeability field II.4(b).	44
III.5 Convergence history for spectral basis with $\theta = 0.7$ and 5 iterations. The snapshot space has dimension 3690 giving 0.01% and 2.84% weighted L^2 and weighted energy errors. When using 5 basis per interior coarse node, the weighted L^2 and the weighted energy errors will be 0.09% and 7.40%, respectively, and the dimension of offline space is 1885.	46

III.6	Convergence history for spectral basis with $\theta = 0.2$ and 19 iterations. The snapshot space has dimension 3690 giving 0.01% and 2.84% weighted L^2 and weighted energy errors. When using 5 basis per interior coarse node, the weighted L^2 and the weighted energy errors will be 0.09% and 7.40%, respectively, and the dimension of offline space is 1885.	46
III.7	Convergence history for spectral basis with $\theta = 0.7$ and the exact indicator. The number of iteration is 6. The snapshot space has dimension 3690 giving 0.01% and 2.84% weighted L^2 and weighted energy errors. When using 5 basis per interior coarse node, the weighted L^2 and the weighted energy errors will be 0.09% and 7.40%, respectively, and the dimension of offline space is 1885.	47
III.8	Coarse-grid energy error distribution using spectral basis with permeability field II.4(b).	49
III.9	Convergence history for harmonic basis using the L^2 indicator with $\theta = 0.7$ and 94 iterations. The snapshot space has dimension 7300 giving 0.05% and 3.02% weighted L^2 and weighted energy errors. When using 12 basis per interior coarse node, the weighted L^2 and the weighted energy errors will be 2.34% and 19.77%, respectively, and the dimension of offline space is 4412.	50
III.10	Convergence history for harmonic basis using snapshot space to compute the proposed indicator. We take $\theta = 0.7$ and the algorithm converges in 22 iterations.	51
IV.1	CG relative errors corresponding to the permeability field in Figure IV.1(a)	83
IV.2	CG relative errors corresponding to the permeability field in Figure IV.1(b)	83
IV.3	DG relative errors corresponding to the permeability field in Figure IV.1(a); snapshot space uses l_{init}^K eigenfunctions	86
IV.4	DG relative errors corresponding to the permeability field in Figure IV.1(b); snapshot space uses l_{init}^K eigenfunctions	86
IV.5	DG relative errors corresponding to the permeability field in Figure IV.1(b); snapshot space uses $l_{\text{max}}^K = l_{\text{init}}^K + 3$ eigenfunctions	88

IV.6	CG relative errors corresponding to the parameter-dependent field constructed from Figure IV.2(a) and IV.2(b)	90
IV.7	DG relative errors corresponding to the parameter-dependent field constructed from Figure IV.2(a) and IV.2(b); snapshot space uses l_{init}^K eigenfunctions	90
IV.8	DG relative errors corresponding to the parameter-dependent field constructed from Figure IV.2(a) and IV.2(b); snapshot space uses $l_{\text{max}}^K = l_{\text{init}}^K + 3$ eigenfunctions	91
V.1	Numerical results for problem (V.1) with κ^{-1} in Figure V.2(b). The L^2 -weighted error and energy error are 66.34% and 99.73% for the MsFEM solution. In the simulation, the dimension of the snapshot space is fixed at 4498 with a weighted L^2 and energy relative error 1.26% and 2.13%.	107
V.2	Numerical results for problem (V.1) with κ^{-1} in Figure V.2(a). The L^2 -weighted error and energy error are 74.68% and 130.42% for the MsFEM solution. In the simulation, the dimension of the snapshot space is fixed at 4498 with a weighted L^2 and energy relative error 1.33% and 13.03%.	107
V.3	Numerical results for problem (V.1) with κ^{-1} in Figure V.2(d). The L^2 -weighted error and energy error are 85.25% and 73.85% for the MsFEM solution. In the simulation, the dimension of the snapshot space is fixed at 4498 with a weighted L^2 and energy relative error 1.94% and 3.54%.	108
V.4	Numerical results for problem (V.1) with κ^{-1} in Figure V.2(c). The L^2 -weighted error and energy error are 74.68% and 130.42% for the MsFEM solution. In the simulation, the dimension of the snapshot space is fixed at 4498 with a weighted L^2 and energy relative error 1.47% and 3.75%.	109

I. INTRODUCTION

I.1 Motivation

Heterogeneous media with multiple scales and high-contrast occur in many practical applications, e.g., porous media, material sciences and Li-ion battery. Usually, the medium properties in these applications vary across many scales. Hence, the development and analysis of numerical methods for accurately resolving complex processes in such media is of vital importance.

In practice, ad-hoc approximations are typically made for resolving the effects of the small scales on a computational grid. For example, in multi-phase flow and transport in porous media, the medium properties are averaged on a coarse grid, and thus the important physical phenomena at small scales are approximated instead of calculated accurately. One solution for this type of problem is multiscale methods. There are a variety of multiscale methods, e.g. [1, 11, 44, 50, 51, 54], that efficiently capture multiscale behavior by constructing a reduced representation of the solution space on a coarse grid. While standard multiscale methods have proven effective for a variety of applications (see, e.g., [43, 44, 45, 54]), a new multiscale algorithm is needed for a more complicated setting.

The multiscale finite element methods (MsFEM's) that we consider in this dissertation hinge on the construction of coarse spaces that are spanned by a set of independently computed multiscale basis functions. The multiscale basis functions are then coupled via a respective global formulation in order to compute the solution. In particular, solutions may be computed on a coarse grid while maintaining the fine-scale effects that are embedded into the basis functions.

The organization of this dissertation is as follows. We present the general frame-

work of this multiscale algorithm for high-contrast heterogeneous elliptic flow in Chapter II. We discuss an oversampling strategy which is introduced for reducing the boundary effects associated with multiscale basis functions. Further, we discuss an efficient method of constructing snapshot space based on the randomized SVD theory in this chapter. The multiscale adaptive algorithm aiming at finding a smaller coarse space is given in Chapter III. The application of GMsFEM to nonlinear elliptic equations through continuous Galerkin and discontinuous Galerkin global formulations is presented in Chapter IV. In Chapter V, we develop GMsFEM for Brinkman flow in high-contrast heterogeneous media. In the next section, a brief introduction to each chapter is provided.

I.2 Outline of the dissertation

The general framework for elliptic equations is provided in Chapter II. In the GMsFEM framework, as in many other multiscale model reduction techniques, one divides the computation into two stages, i.e., the offline stage and the online stage. In the offline stage, a reduced dimension space is constructed, and it is then used in the online stage to construct multiscale basis functions. These multiscale basis functions can be re-used for any input parameter to solve the problem on a coarse grid. The main idea behind the construction of the offline and online spaces is to design appropriate local spectral-based selection of important modes that generate the snapshot space. In [36], several general strategies for designing the local spectrum-based selection procedures were proposed. Two strategies are included in this chapter for the completeness.

One strategy that can increase the accuracy of the GMsFEM is oversampling. Oversampling techniques have been developed in the context of the MsFEM [50] and upscaling methods [22]. These techniques use the local solutions in larger domains

to construct multiscale basis functions to alleviate the effect of mismatch between the artificial boundary condition and the nature of the underlying heterogeneities.

One promising strategy for an efficient calculation of the snapshot space is the randomized snapshot space based on the randomized SVD theory. The main idea behind this strategy is that a smaller number of basis can be calculated instead of the whole snapshot space for a given accuracy.

A posteriori error estimates are discussed in Chapter III. We present two types of residual-based error estimators and show their efficiency and reliability. These error estimators are further used to develop an adaptive enrichment algorithm for the linear elliptic equation in high-contrast heterogeneous media. Numerical tests are provided for the validation of the theoretical results.

In Chapter IV, we discuss GMsFEM for nonlinear flow problems. In the numerical solution of nonlinear elliptic problems, the discrete problem is usually formulated as a system of nonlinear algebraic equations and then linearized through strategies such as Newton's method and Picard iteration. The pivotal advantage of this GMsFEM algorithm lies in the efficient construction of a different online space (and an online solution) at each iteration from the same offline space. Our main contribution is that we have successfully extended GMsFEM to nonlinear problems in the context of both a continuous Galerkin and interior penalty discontinuous Galerkin formulations.

In Chapter V, we develop a multiscale simulation technique for Brinkman flows. The Brinkman model is widely accepted in the mathematical modeling of flows in heterogeneous fields, e.g., flows in vuggy carbonate reservoirs, low porosity filtration devices and biomedical hydrodynamic studies [48, 56]. In these applications, the Darcy model is inadequate to capture their essential physics [53, 65], while the Darcy-Stokes interface model is not feasible since the precise information about the location and geometry of the interface between vugs and the porous matrix as well as

experimentally determined values related to the interface conditions are not directly accessible.

The Brinkman flow behaves like a Darcy flow and a Stokes flow for regions with very small permeability values and large permeability values, respectively. Hence, in comparison with the popular Stokes-Darcy interface model, the Brinkman model can describe both a Stokes and a Darcy flow without involving a complex interface condition. Hence, the accuracy and efficiency of the Brinkman flow simulation is of significant practical interest [38, 32, 70, 73].

In Chapter V, we develop an efficient (multiscale) solver based on the GMsFEM framework [36] for the Brinkman flow in heterogeneous media. In this chapter, we focus on the generation of snapshots spaces, and rigorous convergence analysis of the resulting coarse approximation. Further, we establish stability estimate of the mixed GMsFEM (in the form of inf-sup conditions) for the proposed reduced dimension spaces. The convergence analysis extends that for elliptic equations with high-contrast coefficients [42].

II. GENERALIZED MULTISCALE FINITE ELEMENT METHODS. ELLIPTIC PROBLEMS

II.1 Introduction

In this chapter, we will illustrate the GMsFEM framework in the context of a linear elliptic equation in high-contrast flow, and refer to below for an outline of the framework.

1. Offline computation:

- 1.0. Coarse grid generation;
- 1.1. Construction of snapshot space that will be used to compute an offline space.
- 1.2. Construction of a small dimensional offline space by performing dimension reduction in the space of local snapshots.

2. Online computations:

- 2.1. For each input parameter, compute multiscale basis functions;
- 2.2. Solution of a coarse-grid problem for any force term and boundary condition;
- 2.3. Iterative solvers, if needed.

In the offline computation, we first set up a coarse grid where each coarse-grid block consists of a connected union of fine-grid blocks. A starting point for constructing the offline space is the snapshot space. The snapshot space consists of local functions that can represent the solution space. In particular, we need to identify the local features of the solution space (see Figure II.1 for illustration) without

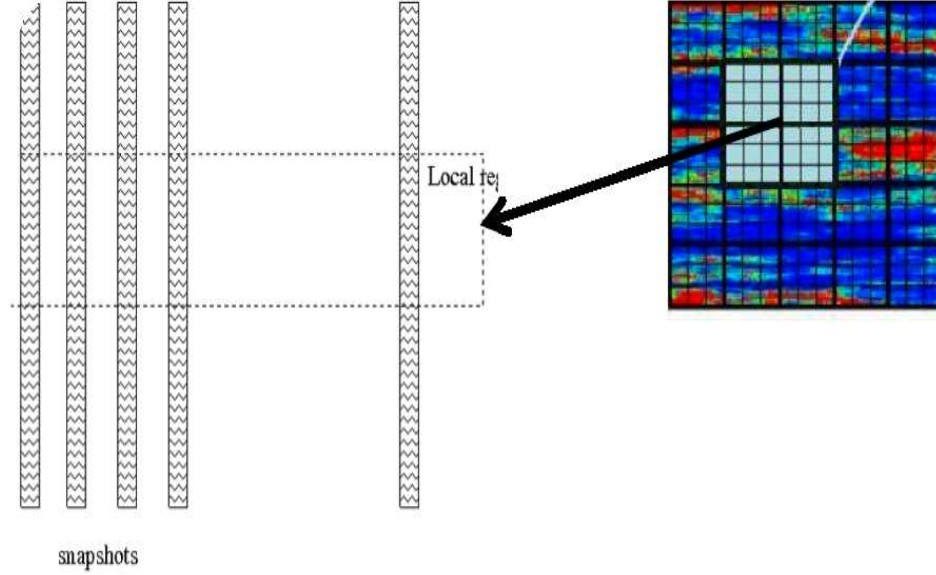


Figure II.1: Local snapshot

computing the solution vectors. The construction of snapshot space in Step 1.1 involves solving local problems for various choices of input parameters or the local fine-grid functions can be used.

The offline space is then extracted from the snapshot space via a spectral decomposition in Step 1.2. This spectral decomposition is typically based on the local eigenvalue problem. The spectral decomposition enables us to select the high-energy elements from the snapshot space by choosing those eigenvectors corresponding to the dominant modes. More precisely, we seek a subspace of the snapshot space such that it can approximate any element of the snapshot space in the appropriate sense defined via auxiliary bilinear forms.

For parameter dependent problems, an online computation is needed. In the online step 2.1, for a given input parameter, we compute the required online coarse space. In general, we want this to be a small dimensional subspace of the offline space. This space is computed by performing a spectral decomposition in the offline

space via an eigenvalue problem. Furthermore, the eigenvectors corresponding to the dominant eigenvalues are identified and used to form the online coarse space. The online coarse space is used within the finite element framework to solve the original global problem.

Further, we investigate the performance of the oversampling strategy in GMs-FEM. Oversampling techniques have been developed in the context of MsFEMs [50] as well as upscaling methods [22]. These techniques use the local solutions in larger domains to construct multiscale basis functions in the context of MsFEM. We borrow that main concept in this chapter. In particular, we use the space of snapshots in the oversampled regions by constructing a snapshot space spanned by harmonic functions or dominant eigenvectors of a local spectral problem formulated in the oversampled domain. Furthermore, we use special local spectral problems to determine the dominant modes in the space of snapshots. This spectral problem is motivated by the analysis and it uses a weighted mass matrix in the oversampled region while the energy (stiffness) matrix is constructed in the target coarse domain.

We also describe the use of multiple local spectral problems for enhancing the accuracy of the approximation and discuss their relation to single spectral problems that use oversampled regions where the latter provides an optimal space.

In the end of this chapter, we consider a snapshot space which consists of harmonic extensions of random boundary conditions defined in a domain larger than the target region motivated by the randomized algorithm presented in [58, 49]. Furthermore, we perform an eigenvalue decomposition in this small space. We study the application of randomized sampling for GMsFEM in conjunction with adaptivity, where local multiscale spaces are adaptively enriched. Convergence analysis is provided in [20]. We present representative numerical results to demonstrate our analysis results.

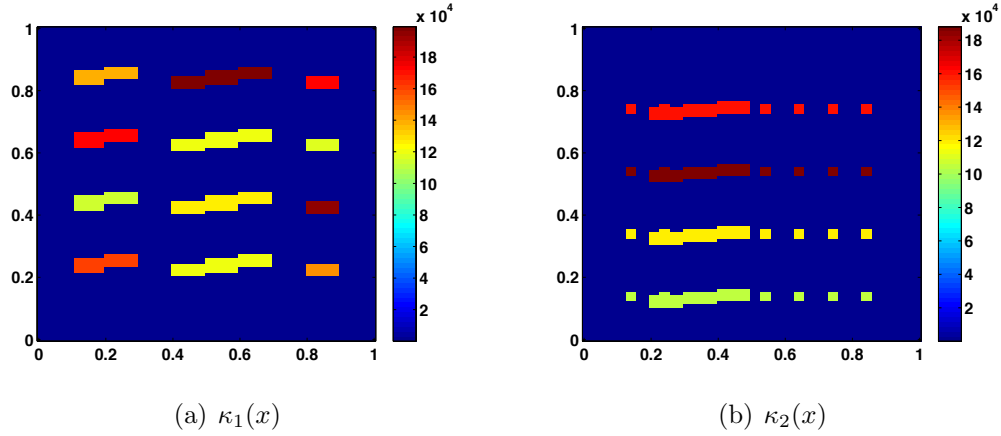


Figure II.2: Decomposition of permeability field

The rest of this chapter is arranged in the following. The problem setup is described in Section II.2. Then we present the calculation of snapshot space, offline space and online space with a flavor of oversampling strategy in Section II.3. The global formulation of the basis in the offline space or online space is shown in Section II.4. We calculate the complexity of GMsFEM for high-contrast flow problems in Section II.5. Finally, an efficient algorithm for the calculation of the snapshot space is presented in Section II.6.

II.2 Preliminaries

We consider elliptic equations of the form

$$-\operatorname{div}(\kappa(x; \mu) \nabla u) = f \text{ in } D, \quad (\text{II.1})$$

where u is prescribed on the boundary ∂D and μ is a parameter. We assume that $\kappa(x; \mu) = \sum_{q=1}^Q \Theta(\mu_q) \kappa_q(x)$ and that the coefficient $\kappa(x; \cdot)$ has multiple scales and high variations (e.g., see Figure II.2).

For the finite element discretization, let \mathcal{T}^H be a usual conforming partition of the

computational domain D into finite elements (triangles, quadrilaterals, tetrahedrals, etc.). We refer to this partition as the coarse grid and assume that each coarse subregion is partitioned into a connected union of fine grid blocks. The fine grid partition will be denoted by \mathcal{T}^h . We use $\{x_i\}_{i=1}^{N_v}$ (where N_v the number of coarse nodes) to denote the vertices of the coarse mesh \mathcal{T}^H , and define the neighborhood of the node x_i by

$$\omega_i = \bigcup \{K_j \in \mathcal{T}^H; \quad x_i \in \overline{K_j}\}. \quad (\text{II.2})$$

See Figure II.3 for an illustration of neighborhoods and elements subordinated to the coarse discretization. In particular, the oversampling technique is used in the construction of local basis functions [40]. We denote by ω_i^+ an oversampled region of $\omega_i \subset \omega_i^+$. In general, we will consider oversampled regions ω_i^+ defined by adding several fine-grid or coarse-grid layers around ω_i .

Next, we briefly outline the global coupling and the role of coarse basis functions for the respective formulations under consideration. In this chapter, we use the continuous Galerkin formulation, and use ω_i as the support of basis functions even though ω_i^+ will be used in constructing multiscale basis functions. For the purpose of this description, we formally denote the basis functions of the online space V_{on} by $\psi_k^{\omega_i}$. The solution will be sought as $u_H(x; \mu) = \sum_{i,k} c_k^i \psi_k^{\omega_i}(x; \mu)$.

Once the basis functions are identified, the global coupling is given through the variational form

$$a(u_H, v; \mu) = (f, v), \quad \text{for all } v \in V_{\text{on}}, \quad (\text{II.3})$$

and

$$a(u, v; \mu) = \int_D \kappa(x; \mu) \nabla u \nabla v.$$

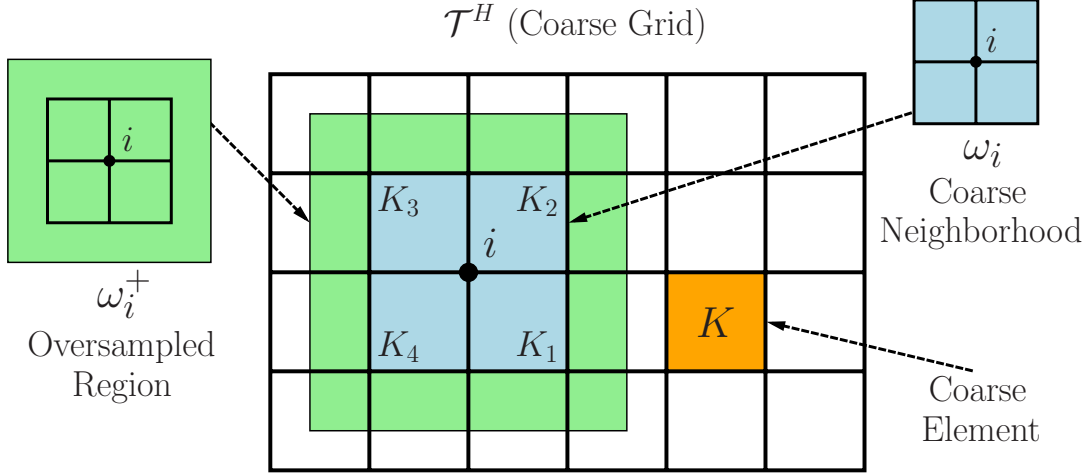


Figure II.3: Illustration of a coarse neighborhood and oversampled domain

II.3 Local basis functions

In this section we describe the offline-online computational procedure, and elaborate on several applicable choices for the associated bilinear forms to be used in the coarse space construction. We will consider both oversampling and non-oversampling spaces.

II.3.1 Snapshot space

We propose several choices for snapshot spaces that are relevant to Galerkin discretization. We refer to [25] for the application of GMsFEM via the mixed finite element method.

II.3.1.1 Harmonic extensions in oversampled region

Our first choice of the snapshot space consists of harmonic extension of fine-grid functions defined on the boundary of ω_i^+ . More precisely, for each fine-grid function, $\delta_l^h(x)$, which is defined by $\delta_l^h(x) = \delta_{l,k}$, $\forall l, k \in J_h(\omega_i^+)$, where $J_h(\omega_i^+)$ denotes the

fine-grid boundary node on $\partial\omega_i^+$ we solve

$$-div(\kappa(x)\nabla\psi_l^{+,snap}) = 0 \quad \text{in } \omega_i^+ \quad (\text{II.4})$$

subject to boundary condition, $\psi_l^{+,snap} = \delta_l^h(x)$ on $\partial\omega_i^+$.

For parameter-dependent one, we can choose several values μ_j , $j = 1, \dots, J$ (J denotes the number of parameters used) to generate the snapshot space separately as above and combine them to obtain the snapshot space (see details in Section II.3.1.2).

Remark II.3.1. *An efficient construction of snapshot space is shown in Section II.6 by an application of the randomized SVD theory.*

II.3.1.2 Local spectral basis

We propose to solve the following Neumann eigenvalue problem on an oversampled domain ω_i^+ :

$$A^+(\mu_j)\psi_{l,j}^{+,snap} = \lambda_{l,j}^{+,snap}S^+(\mu_j)\psi_{l,j}^{+,snap} \quad \text{in } \omega_i^+, \quad (\text{II.5})$$

where μ_j ($j = 1, \dots, J$) is a specified set of fixed parameter values, and we emphasize that the superscript $+$ signifies that the eigenvalue problem is solved in an oversampled coarse subdomain ω_i^+ . The matrices in Eq. (II.5) are defined as

$$\begin{aligned} A^+(\mu_j) &= [a^+(\mu_j)_{mn}] = \int_{\omega_i^+} \kappa(x; \mu_j) \nabla \phi_n \cdot \nabla \phi_m \quad \text{and} \\ S^+(\mu_j) &= [s^+(\mu_j)_{mn}] = \int_{\omega_i^+} \tilde{\kappa}(x; \mu_j) \phi_n \phi_m, \end{aligned} \quad (\text{II.6})$$

where ϕ_n denotes the standard bilinear, fine-scale basis functions and

$$\tilde{\kappa} = \kappa \sum_{i=1}^{N_v} H^2 |\nabla \chi_i^+|^2. \quad (\text{II.7})$$

Here H denotes the coarse mesh size.

Remark II.3.2. *The application of $\tilde{\kappa}$ instead of κ comes from the analysis. We note that the former provides a much more accurate solution than the latter.*

We note that Eq. (II.5) is the discretized form of the continuous equation

$$-\text{div}(\kappa(x; \mu_j) \nabla \psi_{l,j}^{+, \text{snap}}) = \lambda_{l,j}^{+, \text{snap}} \tilde{\kappa}(x; \mu_j) \psi_{l,j}^{+, \text{snap}} \quad \text{in } \omega_i^+.$$

After solving Eq. (II.5), we keep the first L_i eigenfunctions corresponding to the dominant eigenvalues (asymptotically vanishing in this case) to form the space

$$V_{\text{snap}}^+ = \text{span}\{\psi_{l,j}^{+, \text{snap}} : 1 \leq j \leq J \text{ and } 1 \leq l \leq L_i\},$$

for each oversampled coarse neighborhood ω_i^+ . We note that in the case when ω_i is adjacent to the global boundary, no oversampled domain is used. For the sake of simplicity, throughout, we denote continuous and discrete solutions by the same symbol (e.g., $\psi_{l,j}^{+, \text{snap}}$ in the above case).

We reorder the snapshot functions using a single index to create the matrices

$$R_{\text{snap}}^+ = [\psi_1^{+, \text{snap}}, \dots, \psi_{M_{\text{snap}}}^{+, \text{snap}}] \quad \text{and} \quad R_{\text{snap}} = [\psi_1^{\text{snap}}, \dots, \psi_{M_{\text{snap}}}^{\text{snap}}],$$

where ψ_j^{snap} denotes the restriction of $\psi_j^{+, \text{snap}}$ to ω_i , and M_{snap} denotes the total number of functions to keep in the snapshot matrix construction.

Note that the process above to generate local spectral basis is also applied to parameter-independent problems.

II.3.2 Offline space

We will discuss two types of offline spaces where the first one will use one spectral problem in the snapshot space and the other one will use multiple spectral problems in the snapshot space (following Theorem 3.3 of [13]).

II.3.2.1 Offline space using a single spectral problem

In order to construct an oversampled offline space V_{off}^+ or standard neighborhood offline space V_{off} , we perform a dimension reduction in the space of snapshots using an auxiliary spectral decomposition. The main objective is to use the offline space to efficiently (and accurately) construct a set of multiscale basis functions for each μ value in the online stage. More precisely, we seek a subspace of the snapshot space such that it can approximate any element of the snapshot space in the appropriate sense defined via auxiliary bilinear forms.

At the offline stage the bilinear forms are chosen to be *parameter-independent*, such that there is no need to reconstruct the offline space for each μ value. We will consider the following eigenvalue problems in the space of snapshots:

$$A^{\text{off}}\Psi_k^{\text{off}} = \lambda_k^{\text{off}} S^{\text{off}}\Psi_k^{\text{off}} \quad (\text{II.8})$$

$$A^{+, \text{off}}\Psi_k^{\text{off}} = \lambda_k^{\text{off}} A^{\text{off}}\Psi_k^{\text{off}} \quad (\text{II.9})$$

$$A^{\text{off}}\Psi_k^{\text{off}} = \lambda_k^{\text{off}} S^{+, \text{off}}\Psi_k^{\text{off}} \quad (\text{II.10})$$

$$A^{+, \text{off}}\Psi_k^{\text{off}} = \lambda_k^{\text{off}} S^{+, \text{off}}\Psi_k^{\text{off}} \quad (\text{II.11})$$

where

$$\begin{aligned}
A^{\text{off}} &= [a_{mn}^{\text{off}}] = \int_{\omega_i} \bar{\kappa}(x; \mu) \nabla \psi_m^{\text{snap}} \cdot \nabla \psi_n^{\text{snap}} = R_{\text{snap}}^T \bar{A} R_{\text{snap}}, \\
S^{\text{off}} &= [s_{mn}^{\text{off}}] = \int_{\omega_i} \tilde{\kappa}(x; \mu) \psi_m^{\text{snap}} \psi_n^{\text{snap}} = R_{\text{snap}}^T \bar{S} R_{\text{snap}}, \\
A^{+, \text{off}} &= [a_{mn}^{+, \text{off}}] = \int_{\omega_i^+} \bar{\kappa}(x, \mu) \nabla \psi_m^{+, \text{snap}} \cdot \nabla \psi_n^{+, \text{snap}} = (R_{\text{snap}}^+)^T \bar{A}^+ R_{\text{snap}}^+, \\
S^{+, \text{off}} &= [s_{mn}^{+, \text{off}}] = \int_{\omega_i^+} \tilde{\kappa}(x, \mu) \psi_m^{+, \text{snap}} \psi_n^{+, \text{snap}} = (R_{\text{snap}}^+)^T \bar{S}^+ R_{\text{snap}}^+.
\end{aligned}$$

The coefficients $\bar{\kappa}(x, \mu)$ and $\tilde{\kappa}(x, \mu)$ are parameter-averaged coefficients (see [36]). Again, we will take $\tilde{\kappa}(x, \mu) = \bar{\kappa}(x, \mu)$ though one can use multiscale partition of unity functions to compute $\tilde{\kappa}(x, \mu)$ (cf. [41]). We note that \bar{A}^+ and \bar{A} denote analogous fine scale matrices as defined in Eq. (II.5), except that parameter-averaged coefficients are used in the construction, and that A is constructed by integrating only on ω_i .

To generate the offline space we then choose the smallest M_{off} eigenvalues from one of Eqs. (II.8)-(II.11) and form the corresponding eigenvectors in the respective space of snapshots by setting $\psi_k^{+, \text{off}} = \sum_j \Psi_{kj}^{\text{off}} \psi_j^{+, \text{snap}}$ or $\psi_k^{\text{off}} = \sum_j \Psi_{kj}^{\text{off}} \psi_j^{\text{snap}}$ (for $k = 1, \dots, M_{\text{off}}$), where Ψ_{kj}^{off} are the coordinates of the vector Ψ_k^{off} . We then create the offline matrices

$$R_{\text{off}}^+ = [\psi_1^{+, \text{off}}, \dots, \psi_{M_{\text{off}}}^{+, \text{off}}] \quad \text{and} \quad R_{\text{off}} = [\psi_1^{\text{off}}, \dots, \psi_{M_{\text{off}}}^{\text{off}}]$$

to be used in the online space construction.

Our analysis in [40] shows that the convergence of the GMsFEM is proportional to the reciprocal of the eigenvalue that the corresponding eigenvector is not included in the coarse space. We have compared the decay of the reciprocal of eigenvalues for

Eqs. (II.8), (II.9), and (II.11) (by choosing a subdomain for $\kappa(x)$ in Figure II.4(a)).

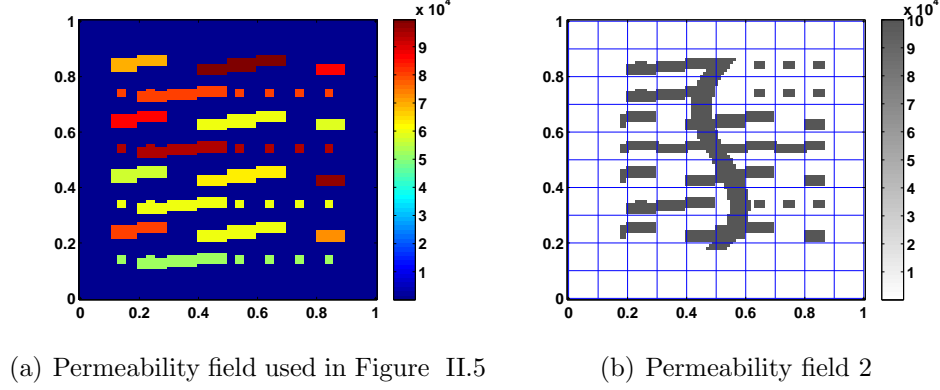


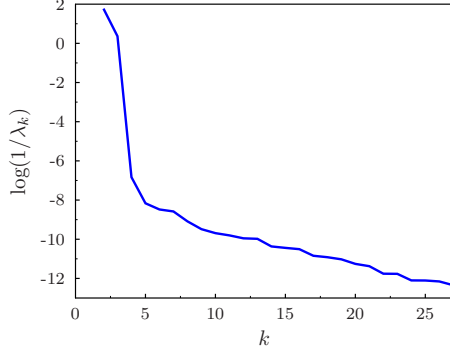
Figure II.4: Permeability fields

We plot the decay of the eigenvalues for a coarse block in Figure II.5 (note logarithmic y-scale). As we observe from this figure that the decay of eigenvalues corresponding to Eq. (II.11) (when oversampling is used in formulating the eigenvalue problem) is faster compared to Eq. (II.8) (when no oversampling is used).

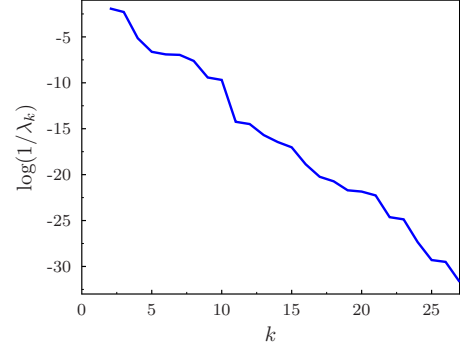
Another view on local spectral problem is that we seek the subspace $V_{\text{off}}^{\omega_i}$ such that for any μ and $\psi \in V_{\text{snapshots}}^{\omega_i}(\mu)$ ($V_{\text{snapshots}}^{\omega_i}(\mu)$ is the space of snapshots which are computed for a given μ), there exists $\psi_0 \in V_{\text{off}}^{\omega_i}$, such that

$$a_{\omega_i}^{\text{off}}(\psi - \psi_0, \psi - \psi_0; \mu) \preceq \delta s_{\omega_i}^{\text{off}}(\psi - \psi_0, \psi - \psi_0; \mu), \quad (\text{II.12})$$

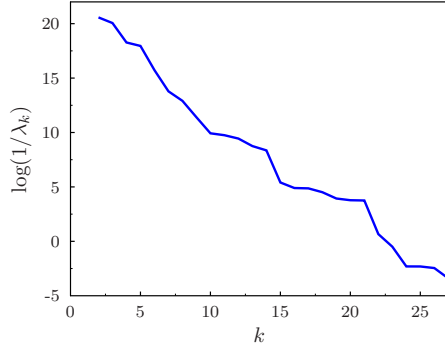
where $a_{\omega_i}^{\text{off}}(\phi, \phi; \mu)$ and $s_{\omega_i}^{\text{off}}(\phi, \phi; \mu)$ are auxiliary bilinear forms. In computations, this involves solving an eigenvalue problem with a mass matrix and the basis functions are selected based on dominant eigenvalues as described above. Note that this eigenvalue problem is formed in the space of snapshots.



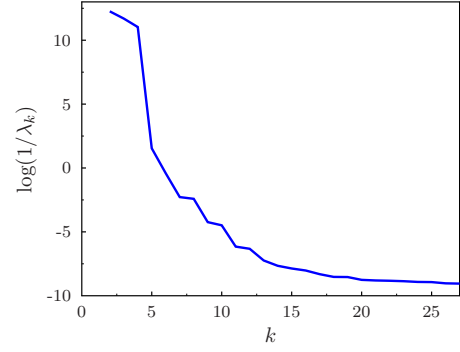
(a) Eigenvalue problem Eq. (II.8) with Harmonic snapshots



(b) Eigenvalue problem Eq. (II.9) with Harmonic snapshots



(c) Eigenvalue problem Eq. (II.11) with Harmonic snapshots



(d) Eigenvalue problem Eq. (II.11) with spectral snapshots

Figure II.5: Eigenvalue decay on log-scale against the number of eigenvalues. x-axis indicates the number of eigenvalue and y-axis indicates the inverse of the eigenvalue (on log-scale)

Remark II.3.3. *In general, $a_{\omega_i}^{\text{off}}$ and $s_{\omega_i}^{\text{off}}$ contain partition of unity functions, penalty terms, and other discretization factors that appear in coarse-grid finite element formulations. The norm corresponding to $s_{\omega_i}^{\text{off}}$ needs to be stronger, in general, to allow the decay of eigenvalues. However, one can also take $s_{\omega_i}^{\text{off}}$ to be weaker.*

II.3.2.2 Offline space using multiple spectral problems

In this subsection, we introduce an offline space that uses both Eq. (II.8) and Eq. (II.11). In particular, we take a union of these eigenvectors to construct an offline space. As described above, we use $\psi_k^{+, \text{off}} = \sum_j \Psi_{kj}^{+, \text{off}} \psi_j^{+, \text{snap}}$ (for $k = 1, \dots, M_{+, \text{off}}$) or $\psi_k^{\text{off}} = \sum_j \Psi_{kj}^{\text{off}} \psi_j^{\text{snap}}$ (for $k = 1, \dots, M_{\text{off}}$), where $\Psi_{kj}^{+, \text{off}}$ are the coordinates of the vector Ψ_k^{off} in Eq. (II.11) and Ψ_{kj}^{off} are the coordinates of the vector Ψ_k^{off} in Eq. (II.8). Then, the offline space is constructed as a union of ψ_k^{off} and $\psi_k^{+, \text{off}}$ after eliminating linearly dependent vectors. Refer to [40] for the convergence of this type of snapshot as well as the numerical tests.

II.3.3 Online space

We only describe the online space using a single spectral problem. One can analogously construct the online space using multiple spectral problems. For the parameter-dependent case, we next construct the associated online coarse space $V_{\text{on}}(\mu)$ for each fixed μ value on each coarse subdomain. In principle, we want this to be a small dimensional subspace of the offline space for computational efficiency.

The online coarse space will be used within the finite element framework to solve the original global problem, where a continuous Galerkin coupling of the multiscale basis functions is used to compute the global solution. In particular, we seek a subspace of the respective offline space such that it can approximate any element of the offline space in an appropriate sense. We note that at the online stage, the bilinear forms are chosen to be *parameter-dependent*. Similar analysis as in Section

II.3.2 motivates the following eigenvalue problems posed in the offline space:

$$A^{\text{on}}(\mu)\Psi_k^{\text{on}} = \lambda_k^{\text{on}} S^{\text{on}}(\mu)\Psi_k^{\text{on}} \quad (\text{II.13})$$

$$A^{+, \text{on}}(\mu)\Psi_k^{\text{on}} = \lambda_k^{\text{on}} A^{\text{on}}(\mu)\Psi_k^{\text{on}} \quad (\text{II.14})$$

$$A^{\text{on}}(\mu)\Psi_k^{\text{on}} = \lambda_k^{\text{on}} S^{+, \text{on}}(\mu)\Psi_k^{\text{on}} \quad (\text{II.15})$$

where

$$A^{\text{on}}(\mu) = [a^{\text{on}}(\mu)_{mn}] = \int_{\omega_i} \kappa(x; \mu) \nabla \psi_m^{\text{off}} \cdot \nabla \psi_n^{\text{off}} = R_{\text{off}}^T A(\mu) R_{\text{off}},$$

$$S^{\text{on}}(\mu) = [s^{\text{on}}(\mu)_{mn}] = \int_{\omega_i} \tilde{\kappa}(x; \mu) \psi_m^{\text{off}} \psi_n^{\text{off}} = R_{\text{off}}^T S(\mu) R_{\text{off}},$$

$$A^{+, \text{on}}(\mu) = [a_{mn}^{+, \text{on}}(\mu)] = \int_{\omega_i^+} \kappa(x, \mu) \nabla \psi_m^{+, \text{off}} \cdot \nabla \psi_n^{+, \text{off}} = (R_{\text{off}}^+)^T A^+(\mu) R_{\text{off}}^+,$$

$$S^{+, \text{on}}(\mu) = [s_{mn}^{+, \text{on}}(\mu)] = \int_{\omega_i^+} \tilde{\kappa}(x, \mu) \psi_m^{+, \text{off}} \psi_n^{+, \text{off}} = (R_{\text{off}}^+)^T S^+(\mu) R_{\text{off}}^+,$$

and $\kappa(x; \mu)$ and $\tilde{\kappa}(x; \mu)$ are now parameter dependent. Again, we will take $\tilde{\kappa}(x, \mu) = \kappa(x, \mu)$ in our simulations though one can use multiscale partition of unity functions to compute $\tilde{\kappa}(x, \mu)$ (cf. [41]).

To generate the online space we then choose the smallest M_{on} eigenvalues from one of Eqs. (II.13)-(II.15) and form the corresponding eigenvectors in the offline space by setting $\psi_k^{\text{on}} = \sum_j \Psi_{kj}^{\text{on}} \psi_j^{\text{off}}$ (for $k = 1, \dots, M_{\text{on}}$), where Ψ_{kj}^{on} are the coordinates of the vector Ψ_k^{on} .

At the online stage, for each parameter value, multiscale basis functions are computed based on each local coarse region. In particular, for each ω_i and for each input parameter, we will formulate a quotient for finding a subspace of $V_{\text{on}}^{\omega_i}(\mu)$ where the space will be constructed for each μ (independent of source terms). We seek a subspace $V_{\text{on}}^{\omega_i}(\mu)$ of $V_{\text{off}}^{\omega_i}$ such that for each $\psi \in V_{\text{off}}^{\omega_i}$, there exists $\psi_0 \in V_{\text{on}}^{\omega_i}(\mu)$ such

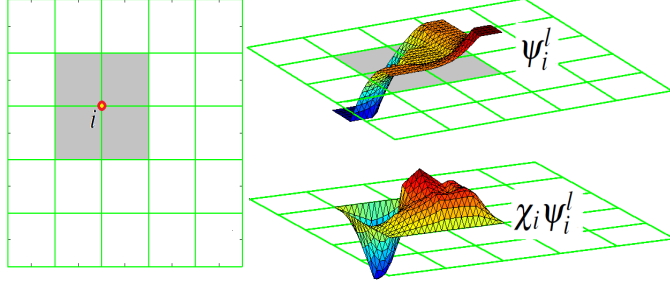


Figure II.6: Schematic description of basis function construction. Left: subdomain ω_i . Right-Top: Selected eigenvector ψ_i^ℓ corresponding to small eigenvalue. Right-Bottom: product $\chi_i \psi_i^\ell$ where χ_i is the initial basis function of node i .

that

$$a_{\omega_i}^{\text{on}}(\psi - \psi_0, \psi - \psi_0; \mu) \preceq \delta s_{\omega_i}^{\text{on}}(\psi - \psi_0, \psi - \psi_0; \mu) \quad (\text{II.16})$$

for some prescribed error tolerance δ (different from the one in the offline stage), and the choices of $a_{\omega_i}^{\text{on}}$ and $s_{\omega_i}^{\text{on}}$. The corresponding eigenvalue problem is formed in the space of offline basis functions.

We note that an assumption as in Remark II.3.3 is needed for obtaining a convergence result and, in general, $a_{\omega_i}^{\text{on}}$ and $s_{\omega_i}^{\text{on}}$ contain partition of unity functions, penalty terms, and other discretization factors that appear in finite element formulations.

II.4 Global coupling

Once multiscale basis functions are constructed, we project the global solution onto the space of basis functions. One can choose different global coupling methods and we present some of them.

Basis functions are computed by selecting a number of eigenvalues (starting with small ones) and multiplying corresponding eigenvectors by χ_i (see Figure II.6 for the illustration).

Galerkin coupling. For a conforming Galerkin formulation, we need to generate

conforming global basis functions. We modify $V_{\text{on}}^{\omega_i}$ by multiplying functions in this space with partition of unity functions χ_i .

We recall that χ_i are initial multiscale basis functions satisfying

$$-\text{div}(\kappa(x; \mu) \nabla \chi_i) = 0 \quad K \in \omega_i \quad (\text{II.17})$$

$$\chi_i = g_i \quad \text{on } \partial K,$$

for all $K \in \omega_i$, where g_i is assumed to be linear.

Remark II.4.1. *Actually, we can use coarse scale nodal basis for the partition of unity function χ_i in the simulation. We admit that the error will increase slightly in this way.*

The subsequent global space has the same dimension defined by $\text{span}_j(\chi_i \psi_j^{\omega_i, \text{on}})$, where $\psi_j^{\omega_i, \text{on}} \in V_{\text{on}}^{\omega_i}(\mu)$ and χ_i is supported in ω_i . Then, the Galerkin approximation can be written as

$$u_{\text{ms}}^G(x; \mu) = \sum_{i,j} c_j^i \chi_i(x) \psi_j^{\omega_i, \text{on}}(x; \mu).$$

If we introduce

$$V_{\text{on}}^G = \text{span}_{i,j}(\chi_i \psi_j^{\omega_i, \text{on}}), \quad (\text{II.18})$$

then Galerkin formulation is given by

$$a(u_{\text{ms}}^G, v; \mu) = (f, v), \quad \forall v \in V_{\text{on}}^G. \quad (\text{II.19})$$

Petrov-Galerkin coupling. We denote $V_{\text{on}}^{\text{PG}} = \text{span}_{i,j}\{\psi_j^{\omega_i}\}$ and write the PG approximation of the solution as

$$u_{\text{ms}}^{\text{PG}}(x; \mu) = \sum_{i,j} c_j^i \psi_j^{\omega_i}(x; \mu).$$

Then the Petrov-Galerkin formulation is given by

$$a(u_{\text{ms}}^{\text{PG}}, v; \mu) = (f, v), \quad \forall v \in V_{\text{on}}^G. \quad (\text{II.20})$$

One can use various other coupling mechanisms, and the application of Symmetric Interior Penalty Discontinuous Galerkin coupling will be discussed in Chapter IV.

II.5 Discussion on complexity

In this section, we will discuss the computational complexity of the GMsFEM for high contrast flow problems. First, the offline and then the online computational complexity will be discussed.

Notice that the offline computations consist of the generation of snapshot space $V_{\text{snap}}^{\omega_i}$. Recall that for each coarse neighborhood ω_i , we have to solve n local problems defined in (II.4), where n is the number of fine-grid boundary nodes of the coarse neighborhoods and is proportional to $(H/h)^{d-1}$, where d is the dimension of the computational domain. Since there are totally N coarse neighborhoods and N is proportional to H^{-d} , the offline stage requires the solution of $O(H^{-1}h^{1-d})$ local problems. For computational times, we assume that each local problem is solved by the conjugate gradient method and the computational times is $O((H/h)^d)$. Thus, the total computational time is $O((H/h)^{d-1}h^{-d})$. We observe that this offline computational time is equivalent to the total computational times for solving the fine grid problem on the whole computational domain $O((H/h)^{d-1})$ times. However, for the offline computational times presented above, we assume that these problems are solved serially. In fact, we achieve much more efficient solves of local problems by computing these in parallel. We emphasize that, even though we spend more time in this offline stage than solving the fine grid problem, the resulting basis functions can be used repeatedly for various source functions and boundary conditions to obtain a

much more reduced global problem. Hence, if one needs to solve the high contrast problem many times, using our GMsFEM is still better than solving the problems directly by discretization on fine grid. Regarding storage complexity, we notice that each basis function needs a space of $O((H/h)^d)$ for storage. Hence, the total storage space is $O((H/h)^{d-1}h^{-d})$.

II.6 Randomized snapshot. Efficient calculation of snapshot

In this section, we introduce an efficient algorithm for the calculation of the snapshot space. The calculation of snapshot spaces may be costly if many local problems are required to solve. We show that this efficiency can be achieved using a moderate quantity of local solutions (or snapshot vectors) with random boundary conditions on oversampled regions with zero forcing.

In the following, we generate inexpensive snapshots using random boundary conditions. That is, instead of solving Eq. (II.4) for each fine boundary node, we solve a small number of local problems imposed with random boundary conditions,

$$\psi_{l,\omega_i}^{+,\text{rsnap}} = r_l \text{ on } \partial\omega_i^+, \quad (\text{II.21})$$

where r_l are independent identically distributed (i.i.d.) standard Gaussian random vectors on the fine-grid nodes of the boundary. Then, we can obtain the local random snapshot on the target domain ω_i by restricting the solution of this local problem, $\psi_{l,\omega_i}^{+,\text{rsnap}}$ to ω_i (which is denoted by $\psi_{l,\omega_i}^{\text{rsnap}}$). The space generated by $\psi_{l,\omega_i}^{\text{rsnap}}$ is a subspace of the space generated by all local snapshots $\Psi_{\omega_i}^{\text{snap}}$. Therefore, there exists a random matrix \mathcal{R} with rows composed by the random boundary vectors r_l , such

that,

$$\Psi_{\omega_i}^{\text{rsnap}} = \mathcal{R}\Psi_{\omega_i}^{\text{snap}}. \quad (\text{II.22})$$

Using these snapshots, we follow the procedure in the previous section to generate multiscale basis functions.

We summarize the algorithm in Table II.6. We denote the buffer number $p_{\text{bf}}^{\omega_i}$ for each ω_i and the number of local basis functions by $k_{\text{nb}}^{\omega_i}$ for each ω_i . Later on, we use the same buffer number for all ω_i and simply use the notation p_{bf} .

Table II.1: Randomized GMsFEM Algorithm

Input:	Fine grid size h , coarse grid size H , oversampling size t , buffer number $p_{\text{bf}}^{\omega_i}$ for each ω_i , the number of local basis functions $k_{\text{nb}}^{\omega_i}$ for each ω_i ;
output:	Coarse-scale solution u_H .
	1. Generate oversampling region for each coarse block: \mathcal{T}^H , \mathcal{T}^h , and ω_i^+ ;
	2. Generate $k_{\text{nb}}^{\omega_i} + p_{\text{bf}}^{\omega_i}$ random vectors r_l and obtain randomized snapshots in ω_i^+ (Eq. (II.21)); Add a snapshot that represents the constant function on ω_i^+ ;
	3. Obtain $k_{\text{nb}}^{\omega_i}$ offline basis by a spectral decomposition (Eq. (II.8));
	4. Construct multiscale basis functions and solve (Eq. (II.3)).

We present representative numerical experiments that demonstrate the performance of the randomized snapshots algorithm. We take the domain D as a square, set the forcing term $f = 0$ and use a linear boundary condition for the problem (II.1), that is, $u = x_1 + x_2$ on ∂D where x_i are the Cartesian components of each point. In our numerical simulations, we use a coarse grid of 10×10 blocks, and each coarse grid block is divided into 10×10 fine grid blocks. Thus, the whole computational domain is partitioned by a 100×100 fine grid. We use a few multiscale basis func-

tions per coarse block. These coarse basis set defines the problem size. We assume that the fine-scale solution is obtained by discretizing problem (II.1) by the classical conforming piecewise bilinear elements on the fine grid.

In Table II.2, a comparison between using all snapshots (refer to Eq. (II.4)) and the randomized snapshots (refer to Eq. (II.21)) is shown. The first column shows the dimension of the offline space for each test. We choose 5, 10, 15, 20, and 25 basis functions per each interior node (in addition to the constant eigenvectors) and use an oversampling layer that consists of three fine-grid blocks ($t = 3$). The offline space V_{off} is defined via a local spectral decomposition as specified in Subsection II.3.2. The snapshot ratio is calculated as the number of randomized snapshots divided by the number of the full snapshots. This ratio is displayed in the second column. Here, the total number of snapshots refers to the number of boundary nodes of the oversampled region.

In our numerical results, an oversampled region has 26×26 fine-grid dimension and there are total 104 snapshots if all boundary nodes are used. For example, when the dimension of the offline space is 931, we only compute 14 snapshots instead of 104. This ratio gives the information on the computational savings of our algorithm compared to the previous algorithm using all snapshots. The next two columns shows the relative weighted L^2 error and relative energy error using the full snapshots. The weighted L^2 norm and energy norm are defined as

$$\|u\|_{L^2_\kappa} = \left(\int_D \kappa u^2 \right)^{\frac{1}{2}} \quad \text{and} \quad \|u\|_{H^1_\kappa} = \left(\int_D \kappa |\nabla u|^2 \right)^{\frac{1}{2}},$$

respectively. Further, the relative weighted L^2 error and relative energy error using the randomized snapshots are shown in the last two columns.

From Table II.2, we observe that the randomized algorithm converges in the sense

that the relative error decreases as we increase the dimension of the coarse space. Comparing the fourth column with the last column, we conclude that the accuracy when using the randomized snapshots is similar to using all snapshot vectors. The latter has much larger dimension as shown in the second column that shows the percentage of the snapshots computed. Therefore, the proposed method is an order of magnitude faster while having comparable accuracy. For example, when the dimension of the offline space is 931, the accuracy of the methods is comparable while randomized snapshot approach uses only 13.46% of the snapshots. Similar results are obtained when the fine mesh is refined to 200×200 . In particular, with the offline space with the dimension 931 and the snapshot ratio of 10%, we obtain similar $L_\kappa^2(D)$ and $H_\kappa^1(D)$ errors which are 1.28% and 24.02%. Here, p_{bf} refers to the buffer that is used to compute the eigenvectors. For example, $p_{\text{bf}} = 4$ means that we use $n + 4$ snapshots to compute n basis functions for each coarse block.

Table II.2: Numerical results comparing the results between using all harmonic snapshots and the snapshots generated by random boundary conditions with $p_{\text{bf}} = 4$, κ as shown in Figure II.4(b). In the parenthesis, we show a higher value of the snapshot ratio.

dim(V_{off})	Snapshot ratio (%)	All snapshots (%)		Few randomized snapshots (%)	
		$L_\kappa^2(D)$	$H_\kappa^1(D)$	$L_\kappa^2(D)$	$H_\kappa^1(D)$
526	8.65(15.38)	0.87	18.15	2.81(1.38)	44.95(26.04)
931	13.46	0.64	14.85	1.04	23.61
1336	18.27	0.55	13.59	0.70	18.08
1741	23.08	0.50	12.69	0.64	15.91
2146	27.88	—	—	0.54	14.16

In Figure II.7, the fine-scale solution, coarse-scale solution using all snapshots and coarse-scale solution using randomized snapshots are shown. They are obtained using the second test (when the dimension of the offline space is 931) in Table II.2.

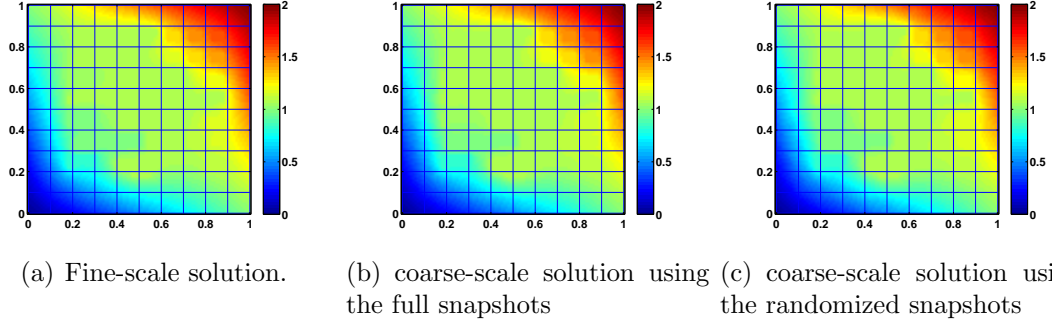


Figure II.7: The fine-scale solution and coarse-scale solutions correspond to Figure II.4(b).

These two coarse-scale solutions are a good approximation of the fine-scale solution.

II.7 Concluding remarks

In this chapter, we briefly introduce the GMsFEM, including the construction of the snapshot space, the offline space, the global formulation, and an efficient calculation of the snapshot space in the context of oversampling strategy based on the randomized SVD theory.

There are several potential improvements in the construction of snapshots that can be done in future. In the construction of harmonic snapshots, we can use network models (see e.g., [15]) to reduce the computational cost. The main idea of network models is to construct a low dimensional network approximation of the solution.

III. ADAPTIVITY FOR GENERALIZED MULTISCALE FINITE ELEMENT METHODS. ELLIPTIC PROBLEMS

III.1 Introduction

In this chapter, we present a posteriori error estimate for the GMSFEM based on the result presented in [26]. In previous findings [42, 40], a priori error bounds for the GMSFEM are derived for linear elliptic equations. It was shown that the convergence rate is proportional to the inverse of the eigenvalue that corresponds to the first eigenvector which is not included in the coarse space. Thus, adding more basis functions will improve the accuracy and it is important to include the eigenvectors that correspond to very small eigenvalues ([42]). Rigorous a posteriori error estimators are needed to perform an adaptive enrichment which is a subject of this chapter. We would like to point out that there are many related activities in designing a posteriori error estimates [28, 30, 5, 52, 63, 69] for global reduced models. The main difference is that our error estimators are based on special local eigenvalue problem and use the eigenstructure of the offline space.

We consider two kinds of error indicators, where one is based on the L^2 -norm of the local residual and the other is based on the weighted H^{-1} -norm (we will also call it H^{-1} -norm based) of the local residual where the weight is related to the coefficient of the elliptic equation. We show that the use of weighted H^{-1} -norm residual gives a more robust error indicator which works well for cases with high contrast media. The convergence analysis of the method is given. In our analysis, we do not consider the error due to the fine-grid discretization of local problems and only study the errors due to the enrichment. In this regard, we assume that the error is largely due to coarse-grid discretization. The fine-grid discretization error can be considered in

general (e.g., as in [5, 30]) and this will give an additional error estimator. The proposed error indicators allow adding multiscale basis functions in the regions detected by the error indicator. The multiscale basis functions are selected by choosing next important eigenvectors (based on the increase of the eigenvalues) from the offline space.

The convergence proof of our adaptive enrichment algorithm is based on the techniques used for proving the convergence of adaptive refinement method for classical conforming finite element methods for second order elliptic problems [17, 59]. Contrary to [59] where mesh refinement is considered, we prove the convergence of our adaptive enrichment algorithm as the approximation space is enriched for a fixed coarse mesh size. The convergence is based on some previously developed spectral estimates. In particular, we use both stability of the coarse-grid projection and the convergence of spectral interpolation. Another key idea is that our error indicators are defined in a variational sense instead of the pointwise residual of the differential equation. By using this variational definition, we avoid the use of the gradient of the multiscale coefficient. Moreover, our convergence analysis does not require that the gradient of the coefficient is bounded, which is not the case for high-contrast multiscale flow problems.

In the proposed error indicators, we consider the use of snapshot space in GMs-FEM. In this case, the residual contains an irreducible error due to the difference between the snapshot solution and the fine-grid solution. We consider the use of snapshot space for approximating the residual error in the case of weighted H^{-1} -norm of the local residual.

We present several numerical tests by considering two different high-contrast multiscale permeability fields. We study both error indicators based on the L^2 -norm of the local residual and the weighted H^{-1} -norm of the local residual. Our

numerical results show that the use of weighted H^{-1} -norm residual gives a more robust error indicator which works well for cases with high contrast media. In our numerical results, we also compare the results obtained by the proposed indicators and the exact error indicator which is computed by considering the energy norm of the difference between the fine-scale solution and the offline solution. Our numerical results show that the use of the exact error indicator gives nearly similar results to the case of using weighted H^{-1} error indicator. In our studies, we also consider the errors between the fine-grid solution and the offline solution as well as the snapshot solution and the offline solution. All cases show that the proposed error indicator is robust and can be used to detect the regions where additional multiscale basis functions are needed.

The rest of this chapter is organized in the following way. In Section III.2, we recall the basic idea of GMsFEM and our main problem. Then in Section III.3, we elaborate the adaptive algorithm and state the main convergence results related to this algorithm and analyze the complexity of this algorithm in Section III.4. In Section III.5, numerical results are illustrated to test the performance of this adaptive algorithm. The proofs of the main results are presented in Section III.6. We conclude with Section III.7.

III.2 Preliminaries

In this chapter, we consider high-contrast flow problems of the form

$$-\operatorname{div}(\kappa(x)\nabla u) = f \quad \text{in } D. \quad (\text{III.1})$$

We assume that $\kappa(x)$ is a heterogeneous coefficient with multiple scales and very high contrast (Figure II.4).

To discretize (III.1), we apply the same notion of fine and coarse grids as intro-

duced in Section II.2. Let V be the conforming finite element space with respect to the fine-scale partition \mathcal{T}^h . We assume $u \in V$ is the fine-scale solution satisfying

$$a(u, v) = (f, v), \quad v \in V, \quad (\text{III.2})$$

where $a(u, v) = \int_D \kappa(x) \nabla u \cdot \nabla v \, dx$, and $(f, v) = \int_D f v \, dx$.

The multiscale solution u_{ms} satisfies

$$a(u_{\text{ms}}, v) = (f, v) \quad \text{for all } v \in V_{\text{off}}. \quad (\text{III.3})$$

We remark that $V_{\text{off}} \subset V$. We emphasize the use of ω_i to denote a coarse neighborhood and K a coarse element. Refer to Chapter II for the construction of the local coarse spaces and the global formulation.

III.3 A posteriori error estimate and adaptive enrichment

In this section, we will derive an a posteriori error indicator for the error $u - u_{\text{ms}}$ in energy norm. We will then use the error indicator to develop an adaptive enrichment algorithm. The a posteriori error indicator gives an estimate of the local error on the coarse grid regions ω_i , and we can then add more basis accordingly to improve the solution.

We will give two kinds of error indicators, one is based on the L^2 -norm of the local residual and the other is based on the weighted H^{-1} -norm of the local residual (for simplicity, we will also call it H^{-1} -norm based indicator). The L^2 -norm residual is also used in the classical adaptive finite element method. In our case, this type of error indicator works well when the coefficient does not contain high contrast region. We will provide a quantitative explanation for this in the next section. On the other hand, the H^{-1} -norm based residual gives a more robust error indicator which works

well for cases with high contrast media. This section is devoted to the derivation of the a posteriori error indicator and the corresponding adaptive enrichment algorithm. The convergence analysis of the method will be given in section III.6.

Next we will give the definitions of the L^2 -based and H^{-1} -based residuals.

L^2 -based residual:

Let ω_i be a coarse grid region. We define a linear functional $Q_i(v)$ on $L^2(\omega_i)$ by

$$Q_i(v) = \int_{\omega_i} f v \chi_i - \int_{\omega_i} a \nabla u_{\text{ms}} \cdot \nabla (v \chi_i). \quad (\text{III.4})$$

The norm of Q_i is defined as

$$\|Q_i\| = \sup_{v \in L^2(\omega_i)} \frac{|Q_i(v)|}{\|v\|_{L^2(\omega_i)}}. \quad (\text{III.5})$$

H^{-1} -based residual:

Let ω_i be a coarse grid region and let $V_i = H_0^1(\omega_i)$. We define a linear functional $R_i(v)$ on V_i by

$$R_i(v) = \int_{\omega_i} f v - \int_{\omega_i} a \nabla u_{\text{ms}} \cdot \nabla v. \quad (\text{III.6})$$

The norm of R_i is defined as

$$\|R_i\|_{V_i^*} = \sup_{v \in V_i} \frac{|R_i(v)|}{\|v\|_{V_i}}, \quad (\text{III.7})$$

where $\|v\|_{V_i} = (\int_{\omega_i} \kappa(x) |\nabla v|^2 dx)^{\frac{1}{2}}$.

We recall that, for each ω_i , the eigenvalues $\lambda_j^{\omega_i}$ are ordered increasingly, and the eigenfunctions corresponding to $\lambda_1^{\omega_i}, \dots, \lambda_{l_i}^{\omega_i}$ are used in the construction of V_{off} . We also define $\tilde{\kappa}_i = \min_{x \in \omega_i} \tilde{\kappa}(x)$.

In section III.6, we will prove the following theorem.

Theorem III.3.1. *Let u and $u_{ms} \in V_{\text{off}}$ be the solutions of the fine scale problem (III.2) and the multiscale problem (III.3) respectively. Assume that*

$$V_{\text{off}} = \text{span}\{\psi_{i,k} : 1 \leq i \leq N \text{ and } 1 \leq k \leq l_i\}$$

where $\psi_{i,k} = \chi_i \psi_k^{\omega_i, \text{off}}$ and l_i is the number of eigenfunctions used for the coarse neighborhood ω_i . Then

$$\|u - u_{ms}\|_V^2 \leq C_{\text{err}} \sum_{i=1}^N \|Q_i\|^2 (\tilde{\kappa}_i \lambda_{l_i+1}^{\omega_i})^{-1}, \quad (\text{III.8})$$

$$\|u - u_{ms}\|_V^2 \leq C_{\text{err}} \sum_{i=1}^N \|R_i\|_{V_i^*}^2 (\lambda_{l_i+1}^{\omega_i})^{-1}. \quad (\text{III.9})$$

where C_{err} is a uniform constant, $\|Q_i\|$ and $\|R_i\|_{V_i^*}$ are respectively the L^2 -based and H^{-1} -based residuals. Moreover, $\lambda_{l_i+1}^{\omega_i}$ denotes the $(l_i + 1)$ -th eigenvalue over coarse neighborhood ω_i , and corresponds to the first eigenvector that is not included in the construction of V_{off} .

From (III.8) and (III.9), we see that the norms $\|Q_i\|$ and $\|R_i\|_{V_i^*}$ give indications on the size of the energy norm error $\|u - u_{ms}\|_V$. Even though (III.8) and (III.9) have the same form, we emphasize that they give different convergence behavior in the high contrast case.

We will now present the adaptive enrichment algorithm. We use $m \geq 1$ to represent the enrichment level and V_{off}^m be the solution space at level m . For each coarse region, we use l_i^m be the number of eigenfunctions used at the enrichment level m for the coarse region ω_i .

Adaptive enrichment algorithm: Choose a fixed number θ with, $0 < \theta < 1$. Choose also an initial offline space V_{off}^1 by specifying a fixed number of basis functions

for each coarse neighborhood, and this number is denoted by l_i^1 . Then, we will generate a sequence of spaces V_{off}^m and a sequence of multiscale solutions u_{ms}^m obtained by solving (III.3). Specifically, for each $m = 1, 2, \dots$, we perform the following calculations:

Step 1: Find the multiscale solution in the current space. That is, find $u_{\text{ms}}^m \in V_{\text{off}}^m$ such that

$$a(u_{\text{ms}}^m, v) = (f, v) \quad \text{for all } v \in V_{\text{off}}^m. \quad (\text{III.10})$$

Step 2: Compute the local residual. For each coarse region ω_i , we compute

$$\eta_i^2 = \begin{cases} \|Q_i\|^2 (\tilde{\kappa}_i \lambda_{l_i^m+1}^{\omega_i})^{-1}, & \text{for } L^2\text{-based residual} \\ \|R_i\|_{V_i^*}^2 (\lambda_{l_i^m+1}^{\omega_i})^{-1}, & \text{for } H^{-1}\text{-based residual} \end{cases}$$

where

$$\begin{aligned} Q_i(v) &= \int_{\omega_i} f v \chi_i - \int_{\omega_i} a \nabla u_{\text{ms}}^m \cdot \nabla (v \chi_i) \\ R_i(v) &= \int_{\omega_i} f v - \int_{\omega_i} a \nabla u_{\text{ms}}^m \cdot \nabla v \end{aligned}$$

and their norms are defined in (III.5) and (III.7) respectively. Next, we re-enumerate the coarse neighborhoods so that the above local residuals η_i^2 are arranged in decreasing order $\eta_1^2 \geq \eta_2^2 \geq \dots \geq \eta_N^2$. That is, in the new enumeration, the coarse neighborhood ω_1 has the largest residual η_1^2 and the coarse neighborhood ω_N has the least residual η_N^2 .

Step 3: Find the coarse regions where enrichment is needed. We choose the smallest integer k such that

$$\theta \sum_{i=1}^N \eta_i^2 \leq \sum_{i=1}^k \eta_i^2. \quad (\text{III.11})$$

The above inequality says that the total residual in the coarse neighborhoods $\omega_1, \omega_2, \dots, \omega_k$ is just larger than a percentage of the total residual, and the percentage θ is a user defined quantity chosen in the beginning of the simulation. These coarse neighborhoods $\omega_1, \omega_2, \dots, \omega_k$ are the regions where the solution contains the largest error.

Step 4: Enrich the space. For each $i = 1, 2, \dots, k$, we add basis function for the region ω_i according to the following rule. Let s be the smallest positive integer such that $\lambda_{l_i^m+s+1}$ is large enough (see the proof of Theorem III.3.3) compared with $\lambda_{l_i^m+1}$. Then we include the eigenfunctions $\Psi_{l_i^m+1}^{\text{off}}, \dots, \Psi_{l_i^m+s}^{\text{off}}$ in the construction of the basis functions. The resulting space is denoted as V_{off}^{m+1} . Mathematically, the space V_{off}^{m+1} is defined as

$$V_{\text{off}}^{m+1} = V_{\text{off}}^m + \text{span } \cup_{i=1}^k \cup_{j=l_i^m+1}^{l_i^m+s} \{\psi_{i,j}\}$$

where $\psi_{i,j} = \chi_i \psi_j^{\omega_i, \text{off}}$ and $\psi_j^{\omega_i, \text{off}} = \sum_{r=1}^{l_i} \Psi_{jr}^{\text{off}} \psi_r^{\text{snap}}$, with $j = l_i^m + 1, \dots, l_i^m + s$, denote the new basis functions obtained by the eigenfunctions $\Psi_{l_i^m+1}^{\text{off}}, \dots, \Psi_{l_i^m+s}^{\text{off}}$. In addition, we set $l_i^{m+1} = l_i^m + s$.

Remark III.3.2. *The algorithm above can be described as follows. We start with an initial space with a small number of basis functions for each coarse grid block. Then we solve the problem and compute the error estimator. We locate the coarse grid blocks with large errors and add more basis functions for these coarse grid blocks. This procedure is repeated until the error goes below a certain tolerance. We remark that the adaptive strategy belongs to the online process, because it is the actual simulation. On the other hand, the generation of basis functions belongs to the offline process.*

About stopping criteria for this algorithm, one can stop the algorithm when the total number of basis functions reach a certain level. On the other hand, one can stop the algorithm when the value of the error indicator goes below a certain tolerance.

We remark that the choice of s above will ensure the convergence of the enrich-

ment algorithm, and in practice, the value of s is easy to obtain. We also remark that the choice of k defined in (III.11) is called the Dorlfer's bulk marking strategy [28]. Moreover, contrary to classical adaptive refinement methods, the total number of basis functions that we can add is bounded by the dimension of the snapshot space. Thus, the condition (III.11) can be modified as follows. We choose the smallest integer k such that

$$\theta \sum_{i=1}^N \eta_i^2 \leq \sum_{i \in I} \eta_i^2,$$

where the index set I is a subset of $\{1, 2, \dots, k\}$ and contains indices j such that l_j^m is less than the maximum number of eigenfunctions for the region ω_j .

We now describe how the norms $\|Q_i\|$ and $\|R_i\|_{V_i^*}$ are computed. Let W_i be the diagonal matrix containing the nodal values of the fine grid cut-off function χ_i in the diagonal. Then the norm $\|Q_i\|$ can be computed as

$$\|Q_i\| = \|W_i(R_0^T F_0 - AR_0^T U_0)\|. \quad (\text{III.12})$$

According to the Riez representation theorem, the norm $\|R_i\|_{V_i^*}$ can be computed as follows. Let z_i be the solution of

$$\int_{\omega_i} a \nabla z_i \cdot \nabla v = R_i(v), \quad \text{for all } v \in V_i. \quad (\text{III.13})$$

Then we have $\|R_i\|_{V_i^*} = \|z_i\|_{V_i}$. Thus, to find the norm $\|R_i\|_{V_i^*}$, we need to solve a local problem on each coarse region ω_i .

Finally, we state the convergence theorem.

Theorem III.3.3. *Let u be the solution of the fine scale problem (III.2) and let u_{ms}^m , $m = 1, 2, \dots$, be the sequence of solutions obtained by the adaptive enrichment algorithm. Then, there are positive constants τ, δ, ρ, L_1 and L_2 such that the following*

contracting property holds

$$\|u - u_{ms}^{m+1}\|_V^2 + \frac{\tau}{1 + \tau\delta L_2} \sum_{i=1}^N S_{m+1}(\omega_i)^2 \leq \varepsilon \left(\|u - u_{ms}^m\|_V^2 + \frac{\tau}{1 + \tau\delta L_2} \sum_{i=1}^N S_m(\omega_i)^2 \right),$$

where $S_m(\omega_i)$ is defined in (III.26) and C_{err} is defined in Theorem III.3.1. Note that $0 < \varepsilon < 1$ and

$$\varepsilon = \max\left(1 - \frac{\theta^2}{L_1(1 + \tau\delta L_2)}, \frac{2C_{err}}{\tau L_1} + \rho\right).$$

We remark that the precise definitions of the constants τ, δ, ρ, L_1 and L_2 are given in Section III.6.

III.4 Discussion on complexity

In this section, we will discuss the complexity of the multiscale enrichment algorithm proposed above. Refer to Section II.5 for the complexity of GMsFEM. We focus on the online computation only in this section for the brevity.

The computational complexity of the online stage can be divided into two parts: (1) the projection of the right hand side onto multiscale space; (2) the computation of the weighted H^{-1} norm of the local residual if the proposed indicator is used. Because the right hand side f is an online quantity, the projection of the right hand side onto the multiscale space at any iteration will require performing calculations on the fine grid. Even though these calculations are inexpensive, our main goal is to keep the computations in the online stage independent of the fine-grid computations. This can be avoided if the right hand side (or a set of right hand sides) can be represented with the multiscale basis functions in the offline stage. For example, if we assume that the right hand side is represented by a few multiscale basis functions, then its projection onto multiscale basis functions in each iteration will require only a few updates. The assumption that the right hand side can be represented by the

multiscale basis function is practical as one can *a priori* determine the space of right hand side functions (e.g., in subsurface applications) and determine its subspace that can be represented accurately using multiscale basis functions. In this regard, our approach shares similarities with *a posteriori* error estimators in reduced basis methods ([66]) where the online stage includes proposing a new parameter μ , in $\kappa(x, \mu)$. As for the computations of the weighted H^{-1} norm of local residual, one can use approximate snapshot spaces to approximate this quantity as we show in Section III.5.4.

III.5 Numerical results

In this section, we will present some numerical experiments to show the performance of the error indicators and the adaptive enrichment algorithm. We take the domain D as a square, set the forcing term $f = 1$ and use a linear boundary condition for the problem (III.1). In our numerical simulations, we use a 20×20 coarse grid, and each coarse grid block is divided into 5×5 fine grid blocks. Thus, the whole computational domain is partitioned by a 100×100 fine grid. We assume that the fine-scale solution is obtained by discretizing (III.1) by the classical conforming piecewise bilinear elements on the fine grid. To test the performance of our algorithm, we consider two permeability fields κ as depicted in Figure II.4. We obtain similar numerical results for these cases, and therefore we will mainly demonstrate the numerical results for the first permeability field (Figure II.4(b)).

Below, we list the indicators used in our simulations. In particular, we will recall the definitions of the L^2 -based and H^{-1} -based error indicators. For comparison purpose, we also use an indicator computed by the exact error in energy norm. We remark that the indicators are computed for each coarse neighborhood ω_i and are defined as follows.

- The indicator constructed using the weighted H^{-1} -based residual is

$$\eta_{\omega_i}^{\text{En}} = \|R_i\|_{V_i^*}^2 (\lambda_{l_i^m+1}^{\omega_i})^{-1} \quad (\text{III.14})$$

and we name it the proposed indicator.

- The indicator constructed using the L^2 -based residual is

$$\eta_{\omega_i}^{\text{L2}} = \|Q_i\|^2 (\tilde{\kappa}_i \lambda_{l_i^m+1}^{\omega_i})^{-1} \quad (\text{III.15})$$

and we name it the L^2 indicator.

- The indicator constructed using the exact energy error is

$$\eta_{\omega_i}^{\text{Ex}} = \|u - u_{\text{ms}}\|_{V_i}^2 \quad (\text{III.16})$$

and name it the exact indicator.

We recall that, in the above definitions, the norms $\|Q_i\|$ and $\|R_i\|_{V_i^*}$ are computed in the way described in (III.12) and (III.13) respectively. For each enrichment level, we will compute the multiscale solution (Step 1) and the corresponding error indicators (Step 2). The indicators $\eta_{\omega_i}^{\text{Ex}}$, $\eta_{\omega_i}^{\text{En}}$ and $\eta_{\omega_i}^{\text{L2}}$ are then ordered in decreasing order. To enrich the approximation space, we select a few coarse neighborhoods such that (III.11) holds for a specific value of θ (Step 3). In our simulations, we consider $\theta = 0.7$ and 0.2 . Finally, for selected coarse neighborhoods, we will enrich the offline space by adding more basis functions (Step 4).

We will consider two types of snapshot spaces, namely the space spanned by all κ -harmonic extensions and the space spanned by all fine-scale conforming piecewise bilinear functions. The sequence of offline basis functions is then obtained by solving

the local spectral problem (II.8) on the space of snapshots. We will call the first type of basis functions as harmonic basis and the second type of basis functions as spectral basis. In addition, we use the notations $\eta_{\omega_i}^{\text{H,En}}$, $\eta_{\omega_i}^{\text{H,L2}}$ and $\eta_{\omega_i}^{\text{H,Ex}}$ to denote the H^{-1} -based, L^2 -based and exact error indicators for the case when the offline space is formed by harmonic basis. Similarly, we use the notations $\eta_{\omega_i}^{\text{U,En}}$, $\eta_{\omega_i}^{\text{U,L2}}$ and $\eta_{\omega_i}^{\text{U,Ex}}$ to denote the H^{-1} -based, L^2 -based and exact error indicators for the case when the offline space is formed by spectral basis (here, superscript U stands for the fact that the snapshot space consists of all fine-grid *unit* vectors).

In the following, we summarize the numerical examples we considered in this chapter.

- **Numerical results with harmonic basis (see Section III.5.1).** We will present numerical results to test the performance of the error indicator $\eta_{\omega_i}^{\text{H, En}}$ and the adaptive enrichment algorithm with $\theta = 0.7$ and $\theta = 0.2$. We also compare our results with the use of $\eta_{\omega_i}^{\text{H,Ex}}$ with $\theta = 0.7$.
- **Numerical results with spectral basis (see Section III.5.2).** We will present numerical results to test the performance of the error indicator $\eta_{\omega_i}^{\text{U, En}}$ and the adaptive enrichment algorithm with $\theta = 0.7$ and $\theta = 0.2$. We also compare our results with the use of $\eta_{\omega_i}^{\text{U,Ex}}$ with $\theta = 0.7$.
- **Numerical results with L^2 indicator (see Section III.5.3).** We will present numerical results to test the performance of the error indicator $\eta_{\omega_i}^{\text{H,L2}}$ and the adaptive enrichment algorithm with $\theta = 0.7$.
- **Numerical results when the proposed indicator is computed in the snapshot space (see Section III.5.4).** We will present numerical results to test the performance of the error indicator $\eta_{\omega_i}^{\text{H,En}}$ and the adaptive enrichment

algorithm with $\theta = 0.7$. In this case, the norm $\|R_i\|_{V_i^*}$ is computed in the snapshot space instead of the fine-grid space.

In the following, we will give a brief summary of our conclusions before discussing the numerical results.

- The use of both $\eta_{\omega_i}^{\text{H, En}}$ and $\eta_{\omega_i}^{\text{U, En}}$ gives a convergent sequence of numerical solutions. This verifies the convergence of our adaptive GMsFEM.
- The performance of the proposed indicators $\eta_{\omega_i}^{\text{H, En}}$ and $\eta_{\omega_i}^{\text{U, En}}$ is similar to that of the exact indicators $\eta_{\omega_i}^{\text{H, Ex}}$ and $\eta_{\omega_i}^{\text{U, Ex}}$. Thus, the proposed indicator gives a good estimate of the exact error.
- The performance of the weighted H^{-1} -based indicator is much better than that of the L^2 -based indicator for high-contrast problems.
- The use of the snapshot space to compute $\eta_{\omega_i}^{\text{H, En}}$ and $\eta_{\omega_i}^{\text{U, En}}$ in (III.13) gives similar results compared to the use of local fine-grid solves. Thus, the computations of $\eta_{\omega_i}^{\text{H, En}}$ and $\eta_{\omega_i}^{\text{U, En}}$ can be performed efficiently.
- With the use of $\theta = 0.2$, we obtain more accurate results for the same dimensional offline spaces compared with $\theta = 0.7$.

In the tables listed below, we recall that V_{off} denotes the offline space; u , u_{snap} and u_{off} denote the fine-scale, snapshot and offline solutions respectively. Moreover, to compare the results, we will compute the error $u - u_{\text{off}}$ using the L^2 relative error and the energy relative error, which are defined as

$$\|u - u_{\text{off}}\|_{L_{\kappa}^2(D)} := \frac{\|u - u_{\text{off}}\|_{L^2(V)}}{\|u\|_{L^2(V)}} \quad \text{and} \quad \|u - u_{\text{off}}\|_{H_{\kappa}^1(D)} := \frac{a(u - u_{\text{off}}, u - u_{\text{off}})^{\frac{1}{2}}}{a(u, u)^{\frac{1}{2}}}, \quad (\text{III.17})$$

where the weighted L^2 -norm is defined as $\|u\|_{L^2(V)} = \|\kappa^{\frac{1}{2}}u\|_{L^2(D)}$. We will also compute the error $u_{\text{snap}} - u_{\text{off}}$ using the same norms

$$\begin{aligned}\|u_{\text{snap}} - u_{\text{off}}\|_{L^2_\kappa(D)} &:= \frac{\|u_{\text{snap}} - u_{\text{off}}\|_{L^2(V)}}{\|u_{\text{snap}}\|_{L^2(V)}}, \\ \|u_{\text{snap}} - u_{\text{off}}\|_{H^1_\kappa(D)} &:= \frac{a(u_{\text{snap}} - u_{\text{off}}, u - u_{\text{off}})^{\frac{1}{2}}}{a(u_{\text{snap}}, u_{\text{snap}})^{\frac{1}{2}}}.\end{aligned}\tag{III.18}$$

III.5.1 Numerical results with harmonic basis

In this section, we present numerical examples to test the performance of the proposed indicator $\eta_{\omega_i}^{\text{H,En}}$ and the convergence of our adaptive enrichment algorithm with $\theta = 0.7$ and $\theta = 0.2$. We will also compare our results with the use of the exact indicator $\eta_{\omega_i}^{\text{H,Ex}}$. In the simulations, we take a snapshot space of dimension 7300 giving errors of 0.05% and 3.02% in weighted L^2 and weighted H^1 norms, respectively. Thus, the solution u_{snap} is as good as the fine-scale solution u . For the adaptive enrichment algorithm, the initial offline space has 4 basis functions for each coarse grid node. At each enrichment (Step 4), we will add one basis function for the coarse grid nodes selected in Step 3. We will terminate the iteration when the energy error $\|u - u_{\text{off}}\|_V$ is less than 5% of $\|u - u_{\text{snap}}\|_V$.

In Table III.1 and Table III.2, we present the convergence history of the adaptive enrichment algorithm for $\theta = 0.7$ and $\theta = 0.2$ respectively. For both cases, we see a convergence of the algorithm. For the case $\theta = 0.7$, the algorithm requires 18 iterations to achieve the desired accuracy. The dimension of the corresponding offline space is 3378. Moreover, the error $u - u_{\text{off}}$ in relative weighted L^2 and energy norms are 0.54% and 7.83% respectively, while the error $u_{\text{snap}} - u_{\text{off}}$ in relative weighted L^2 and energy norms are 0.51% and 7.22% respectively. And we see the similarity of the errors $u - u_{\text{off}}$ and $u_{\text{snap}} - u_{\text{off}}$. For the case $\theta = 0.2$, the algorithm requires 66

$\dim(V_{\text{off}})$	$\ u - u_{\text{off}}\ $ (%)		$\ u_{\text{snap}} - u_{\text{off}}\ $ (%)	
	$L^2_\kappa(D)$	$H^1_\kappa(D)$	$L^2_\kappa(D)$	$H^1_\kappa(D)$
1524	4.50	31.29	4.49	34.14
1711	4.24	27.37	4.23	27.19
2434	2.34	20.13	2.36	20.31
2637	1.64	15.43	1.61	15.13
3378	0.54	7.83	0.51	7.22

Table III.1: Convergence history for harmonic basis with $\theta = 0.7$ and 18 iterations. The snapshot space has dimension 7300 giving 0.05% and 3.02% weighted L^2 and weighted energy errors. When using 12 basis per coarse inner node, the weighted L^2 and the weighted H^1 errors will be 2.34% and 19.77%, respectively, and the dimension of offline space is 4412.

$\dim(V_{\text{off}})$	$\ u - u_{\text{off}}\ $ (%)		$\ u_{\text{snap}} - u_{\text{off}}\ $ (%)	
	$L^2_\kappa(D)$	$H^1_\kappa(D)$	$L^2_\kappa(D)$	$H^1_\kappa(D)$
1524	4.50	31.29	4.49	34.14
1646	4.05	26.80	4.04	26.62
1864	3.09	20.34	3.07	20.11
2220	1.24	14.43	1.20	14.11
3135	0.48	7.98	0.45	7.39

Table III.2: Convergence history for harmonic basis with $\theta = 0.2$. The number of iterations is 66. The snapshot space has dimension 7300 giving 0.05% and 3.02% weighted L^2 and weighted energy errors. When using 12 basis per coarse inner node, the weighted L^2 and the weighted H^1 errors will be 2.34% and 19.77%, respectively, and the dimension of offline space is 4412.

iterations to achieve the desired accuracy. The dimension of the corresponding offline space is 3135. Moreover, the error $u - u_{\text{off}}$ in relative weighted L^2 and energy norms are 0.48% and 7.98% respectively, while the error $u_{\text{snap}} - u_{\text{off}}$ in relative weighted L^2 and energy norms are 0.45% and 7.39% respectively. Furthermore, we observe that the use of $\theta = 0.2$ gives the same level of error for a smaller offline space compared with $\theta = 0.7$. Thus, we conclude that a smaller value of θ will give a more economical offline space. To show that our adaptive enrichment algorithm gives a more efficient

scheme, we report some computational results with uniform enrichment. In this case, we use 12 basis functions for each interior coarse grid node giving an offline space of dimension 4412. The relative weighted L^2 and energy errors are 2.32% and 19.53% respectively. From this result, we see that our adaptive enrichment algorithm gives a smaller offline space and at the same time a better accuracy than a scheme with uniform number of basis functions.

$\dim(V_{\text{off}})$	$\ u - u_{\text{off}}\ $ (%)		$\ u_{\text{snap}} - u_{\text{off}}\ $ (%)	
	$L_{\kappa}^2(D)$	$H_{\kappa}^1(D)$	$L_{\kappa}^2(D)$	$H_{\kappa}^1(D)$
1524	4.50	31.29	4.49	34.14
1762	3.96	27.09	3.95	26.91
2333	2.07	19.00	2.04	18.75
2522	1.38	15.12	1.36	14.81
3466	0.46	7.52	0.44	6.89

Table III.3: Convergence history for harmonic basis with $\theta = 0.7$ and the exact indicator. The number of iterations is 23. The snapshot space has dimension 7300 giving 0.05% and 3.02% weighted L^2 and weighted energy errors.

To test the reliability and efficiency of the proposed indicator, we apply the adaptive enrichment algorithm with the exact energy error as indicator and $\theta = 0.7$. The results are shown in Table III.3. In particular, the algorithm requires 19 iterations to achieve the desired accuracy. The dimension of the corresponding offline space is 3466. Moreover, the error $u - u_{\text{off}}$ in relative weighted L^2 and energy norms are 0.46% and 7.52% respectively, while the error $u_{\text{snap}} - u_{\text{off}}$ in relative weighted L^2 and energy norms are 0.44% and 6.89% respectively. Comparing the results in Table III.1 and Table III.3 for the use of the proposed and the exact indicator respectively, we see that both indicators give similar convergence behavior and offline space dimensions.

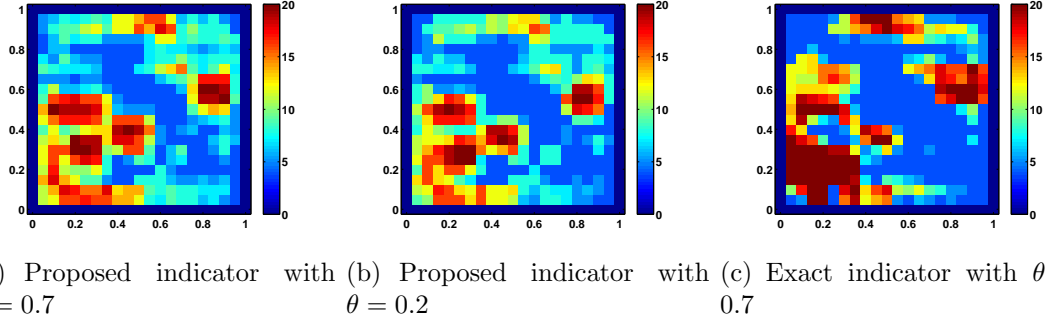


Figure III.1: Dimension distributions of the last offline space for harmonic basis with permeability field II.4(b).

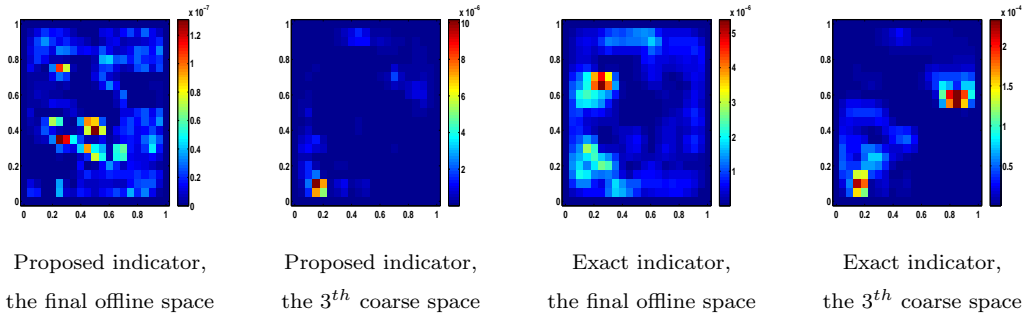


Table III.4: Coarse-grid energy error distribution using harmonic basis with permeability field II.4(b).

In Figure III.1, we display the number of basis functions for each coarse grid node of the last offline spaces for the proposed indicator with $\theta = 0.7$, the proposed indicator with $\theta = 0.2$ and the exact indicator with $\theta = 0.7$. From Figures III.1(a) and III.1(b), we observe a similar dimension distribution for the use of the proposed indicator with $\theta = 0.7$ and $\theta = 0.2$, and the case $\theta = 0.2$ gives a smaller number of basis functions. For the case with the exact indicator, we see from Figure III.1(c) that the dimension distribution follows a similar pattern, but with regions that contain larger number of basis functions.

Finally, we present the energy errors on coarse neighborhoods for $\theta = 0.7$ for

an intermediate offline space and the last offline space of the proposed indicator $\eta_{\omega_i}^{\text{H,En}}$ and the exact indicator $\eta_{\omega_i}^{\text{H,Ex}}$. In Figures III.5.1 and III.5.1, the energy error distributions for the last offline spaces and an intermediate offline space obtained by the proposed indicator are shown respectively. We see how the energy error is reduced by enriching the space from an intermediate step to the final step. A similar situation is also seen from Figures III.5.1 and III.5.1 for the case with the exact indicator.

III.5.2 Numerical results with spectral basis

In this section, we repeat the above tests using the spectral snapshot space instead of the harmonic snapshot space with the proposed indicator $\eta_{\omega_i}^{\text{U,En}}$ and the exact indicator $\eta_{\omega_i}^{\text{U,Ex}}$. The results are presented in Tables III.5, III.6 and III.7. In the simulations, we take a snapshot space of dimension 3690 giving errors of 0.01% and 2.84% in weighted L^2 and energy norms respectively. Thus, the solution u_{snap} is as good as the fine-scale solution u . For the adaptive enrichment algorithm, the initial offline space has 2 basis functions for each coarse grid node. At each enrichment (Step 4), we will add one basis function for the coarse grid nodes selected in Step 3. We will terminate the iteration when the energy error $\|u - u_{\text{off}}\|_V$ is less than 5% of $\|u - u_{\text{snap}}\|_V$.

In Table III.5 and Table III.6, we present the convergence history of the adaptive enrichment algorithm for $\theta = 0.7$ and $\theta = 0.2$ respectively. For both cases, we see a clear convergence of the algorithm. For the case $\theta = 0.7$, the algorithm requires 5 iterations to achieve the desired accuracy. The dimension of the corresponding offline space is 1410. Moreover, the error $u - u_{\text{off}}$ in relative weighted L^2 and energy norms are 0.10% and 7.43% respectively, while the error $u_{\text{snap}} - u_{\text{off}}$ in relative weighted L^2 and energy norms are 0.10% and 6.87% respectively. For the case $\theta = 0.2$, the

$\dim(V_{\text{off}})$	$\ u - u_{\text{off}}\ $ (%)		$\ u_{\text{snap}} - u_{\text{off}}\ $ (%)	
	$L^2_\kappa(D)$	$H^1_\kappa(D)$	$L^2_\kappa(D)$	$H^1_\kappa(D)$
802	0.87	20.15	0.87	19.94
868	0.83	16.51	0.83	16.26
979	0.33	12.62	0.33	12.30
1106	0.32	10.44	0.32	10.05
1410	0.10	7.43	0.10	6.87

Table III.5: Convergence history for spectral basis with $\theta = 0.7$ and 5 iterations. The snapshot space has dimension 3690 giving 0.01% and 2.84% weighted L^2 and weighted energy errors. When using 5 basis per interior coarse node, the weighted L^2 and the weighted energy errors will be 0.09% and 7.40%, respectively, and the dimension of offline space is 1885.

$\dim(V_{\text{off}})$	$\ u - u_{\text{off}}\ $ (%)		$\ u_{\text{snap}} - u_{\text{off}}\ $ (%)	
	$L^2_\kappa(D)$	$H^1_\kappa(D)$	$L^2_\kappa(D)$	$H^1_\kappa(D)$
802	0.87	20.15	0.87	19.94
856	0.83	16.25	0.82	16.00
960	0.34	12.58	0.33	12.26
1116	0.32	10.27	0.32	9.87
1334	0.09	7.55	0.09	6.99

Table III.6: Convergence history for spectral basis with $\theta = 0.2$ and 19 iterations. The snapshot space has dimension 3690 giving 0.01% and 2.84% weighted L^2 and weighted energy errors. When using 5 basis per interior coarse node, the weighted L^2 and the weighted energy errors will be 0.09% and 7.40%, respectively, and the dimension of offline space is 1885.

algorithm requires 19 iterations to achieve the desired accuracy. The dimension of the corresponding offline space is 1334. Moreover, the error $u - u_{\text{off}}$ in relative weighted L^2 and energy norms are 0.09% and 7.55% respectively, while the error $u_{\text{snap}} - u_{\text{off}}$ in relative weighted L^2 and energy norms are 0.09% and 6.99% respectively. Furthermore, we observe that the use of $\theta = 0.2$ gives the same level of error for a smaller offline space compared with $\theta = 0.7$. Thus, we conclude that a smaller value of θ will give a more economical offline space. To show that our adaptive enrichment

algorithm gives a more efficient scheme, we report some computational results with uniform enrichment. In this case, we use 5 basis functions for each interior coarse grid node giving an offline space of dimension 1885. The relative weighted L^2 and energy errors are 0.09% and 7.40% respectively. From this result, we see that our adaptive enrichment algorithm gives a smaller offline space and at the same time a better accuracy than a scheme with uniform number of basis functions.

$\dim(V_{\text{off}})$	$\ u - u_{\text{off}}\ $ (%)		$\ u_{\text{snap}} - u_{\text{off}}\ $ (%)	
	$L^2_{\kappa}(D)$	$H^1_{\kappa}(D)$	$L^2_{\kappa}(D)$	$H^1_{\kappa}(D)$
802	0.87	20.15	0.87	19.94
884	0.42	14.73	0.42	14.45
1000	0.18	12.25	0.18	11.91
1119	0.17	9.83	0.17	9.41
1392	0.10	7.12	0.10	6.53

Table III.7: Convergence history for spectral basis with $\theta = 0.7$ and the exact indicator. The number of iteration is 6. The snapshot space has dimension 3690 giving 0.01% and 2.84% weighted L^2 and weighted energy errors. When using 5 basis per interior coarse node, the weighted L^2 and the weighted energy errors will be 0.09% and 7.40%, respectively, and the dimension of offline space is 1885.

To test the reliability and efficiency of the proposed indicator, we apply the adaptive enrichment algorithm with the exact energy error as indicator and $\theta = 0.7$. The results are shown in Table III.7. In particular, the algorithm requires 6 iterations to achieve the desired accuracy. The dimension of the corresponding offline space is 1392. Moreover, the error $u - u_{\text{off}}$ in relative weighted L^2 and energy norms are 0.10% and 7.12% respectively, while the error $u_{\text{snap}} - u_{\text{off}}$ in relative weighted L^2 and energy norms are 0.10% and 6.53% respectively. Comparing the results in Table III.5 and Table III.7 for the use of the proposed and the exact indicator respectively, we see that both indicators give similar convergence behavior and offline space dimensions.

We also observe that the exact indicator performs better in this case.

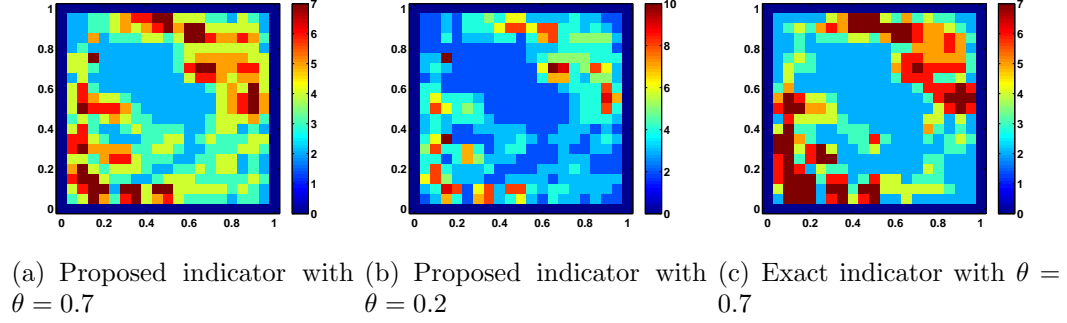


Figure III.2: Dimension distributions of the last offline space for spectral basis with permeability field II.4(b).

In Figure III.2, we display the number of basis functions for each coarse grid node of the last offline spaces for the proposed indicator with $\theta = 0.7$, the proposed indicator with $\theta = 0.2$ and the exact indicator with $\theta = 0.7$. From Figures III.2(a) and III.2(b), we observe a similar dimension distribution for the use of the proposed indicator with $\theta = 0.7$ and $\theta = 0.2$, and the case $\theta = 0.2$ gives a smaller number of basis functions. For the case with the exact indicator, we see from Figure III.2(c) that the dimension distribution follows a similar pattern, but with regions that contain larger number of basis functions.

Finally, we present the energy errors on coarse neighborhoods for $\theta = 0.7$ for an intermediate offline space and the last offline space of the proposed indicator $\eta_{\omega_i}^{\text{H,En}}$ and the exact indicator $\eta_{\omega_i}^{\text{H,Ex}}$. In Figures III.5.2 and III.5.2, the energy error distributions for the last offline spaces and an intermediate offline space obtained by the proposed indicator are shown respectively. We see clearly that how the energy error is reduced by enriching the space from an intermediate step to the final step. A similar situation is also seen from Figures III.5.2 and III.5.2 for the case with the

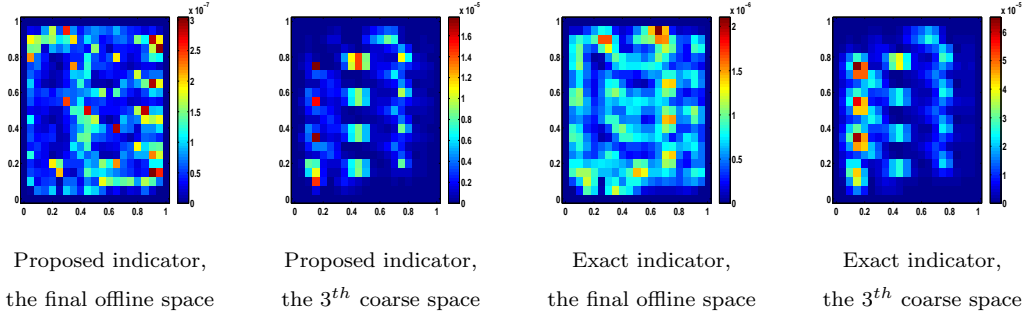


Table III.8: Coarse-grid energy error distribution using spectral basis with permeability field II.4(b).

exact indicator.

III.5.3 Numerical results with the L^2 indicator

In this section, we present some numerical simulations to test the performance of the L^2 indicator. We note that this is the most natural error indicator, as it is more efficient to compute and is widely used for classical adaptive finite element methods [59]. However, this indicator does not work well for high contrast coefficients. In the simulation, we will conduct the same test as in Section III.5.1 with the indicator replaced by $\eta_{\omega_i}^{\text{H},L^2}$.

In Table III.9, we present the convergence history of the adaptive enrichment algorithm for $\theta = 0.7$, and we observe a clear convergence of the algorithm. Notice that, the algorithm requires 94 iterations to achieve the desired accuracy. The dimension of the corresponding offline space is 4509. If we compare these results to the case with the proposed indicator, we see that the L^2 indicator will give a much larger offline space and a larger number of iterations, in order to achieve a similar accuracy.

Finally we will compare the basis function and error distributions for the L^2 indicator with those for the proposed indicator. In Figure III.3(a), the number of

$\dim(V_{\text{off}})$	$\ u - u_{\text{off}}\ $ (%)		$\ u_{\text{snap}} - u_{\text{off}}\ $ (%)	
	$L^2_\kappa(D)$	$H^1_\kappa(D)$	$L^2_\kappa(D)$	$H^1_\kappa(D)$
1524	4.50	31.29	4.49	31.14
1913	3.59	26.88	3.57	26.69
2513	2.43	21.46	2.43	20.89
3006	1.11	17.11	1.12	16.83
4509	0.06	7.97	0.04	7.37

Table III.9: Convergence history for harmonic basis using the L^2 indicator with $\theta = 0.7$ and 94 iterations. The snapshot space has dimension 7300 giving 0.05% and 3.02% weighted L^2 and weighted energy errors. When using 12 basis per interior coarse node, the weighted L^2 and the weighted energy errors will be 2.34% and 19.77%, respectively, and the dimension of offline space is 4412.

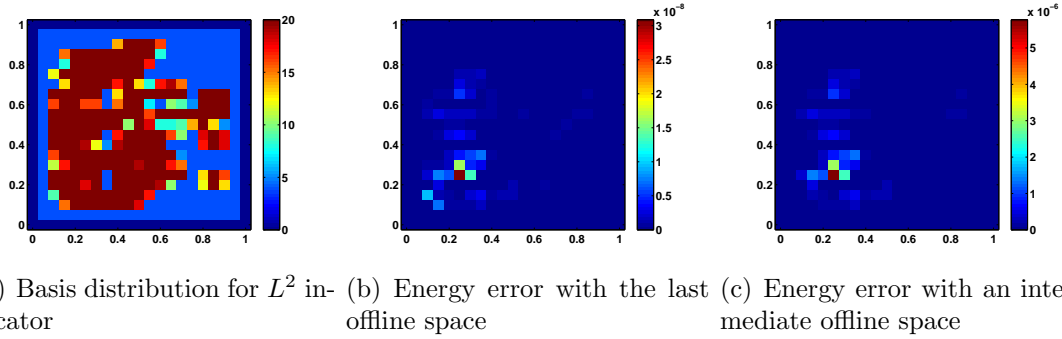


Figure III.3: Basis distribution and error distribution for harmonic basis with L^2 indicator.

basis functions for each coarse node is shown. We observe that the distribution is similar to the case with the proposed indicator shown in Figure III.1(a). We also observe that the number of basis functions for the L^2 indicator is much larger than that for the proposed indicator. In Figures III.3(b) and III.3(c), the energy error distributions for the last offline spaces and an intermediate offline space obtained by the L^2 indicator are shown respectively. We see clearly that how the energy error is reduced by enriching the space from an intermediate step to the final step. However, we also see a very slow decay in energy error for the L^2 indicator.

III.5.4 Numerical results using snapshot solutions for the proposed indicator

In this section, we present numerical tests to show that our adaptive method is equally good when the proposed indicator $\eta_{\omega_i}^{\text{H,En}}$ is computed in the snapshot space. In particular, we will solve the local problems (III.13) in the space of snapshots instead of the fine scale space, in order to reduce the computational costs. We will again repeat the same test as in Section III.5.1. In Table III.10 we present the convergence history of the adaptive enrichment algorithm with $\theta = 0.7$, and observe a clear convergence of the algorithm. Moreover, the algorithm requires 22 iterations to achieve the desired accuracy. The dimension of the corresponding offline space is 3688. In addition, the error $u - u_{\text{off}}$ in relative weighted L^2 and energy norms are 0.17% and 7.83% respectively, while the error $u_{\text{snap}} - u_{\text{off}}$ in relative weighted L^2 and energy norms are 0.14% and 7.26% respectively. If we compare these results with those for the proposed indicator (see Table III.1), we see the use of snapshot space to compute the error indicator will give a similar offline space and accuracy, but with a larger number of iterations.

$\dim(V_{\text{off}})$	$\ u - u_{\text{off}}\ $ (%)		$\ u_{\text{snap}} - u_{\text{off}}\ $ (%)	
	$L_{\kappa}^2(D)$	$H_{\kappa}^1(D)$	$L_{\kappa}^2(D)$	$H_{\kappa}^1(D)$
1524	7.60	50.86	7.59	50.75
1772	4.18	27.08	4.18	26.90
2398	2.41	20.59	2.39	20.36
2824	1.28	13.98	1.25	13.64
3688	0.17	7.83	0.14	7.26

Table III.10: Convergence history for harmonic basis using snapshot space to compute the proposed indicator. We take $\theta = 0.7$ and the algorithm converges in 22 iterations.

III.6 Convergence analysis

In this section, we will give the proofs for the a posteriori error estimates (III.8)-(III.9) and the convergence of the adaptive enrichment algorithm.

For each $i = 1, 2, \dots, N$, we let $P_i : V \rightarrow \text{span}\{\psi_k^{\omega_i, \text{off}}\}$ be the projection defined by

$$P_i v = \sum_{k=1}^{l_i} \left(\int_{\omega_i} \tilde{\kappa} v \psi_k^{\omega_i, \text{off}} \right) \psi_k^{\omega_i, \text{off}}.$$

The projection P_i has following stability bound

$$\|\chi_i(P_i v)\|_{V_i} \leq C_{\text{stab}}^{\omega_i} \|v\|_{V_i} \quad (\text{III.19})$$

where the constant $C_{\text{stab}}^{\omega_i} = \max(1, H^{-1}(\lambda_{l_i+1}^{\omega_i})^{-\frac{1}{2}})$. Moreover the following convergence result holds

$$\|\chi_i(v - P_i v)\|_{V_i} \leq C_{\text{conv}}^{\omega_i} (\lambda_{l_i+1}^{\omega_i})^{-\frac{1}{2}} \|v\|_{V_i} \quad (\text{III.20})$$

where $C_{\text{conv}}^{\omega_i}$ is a uniform constant. We also define the projection $\Pi : V \rightarrow V_{\text{off}}$ by $\Pi v = \sum_{i=1}^N \chi_i(P_i v)$. For the analysis below, we let

$$C_{\text{stab}} = \max_{1 \leq i \leq N} C_{\text{stab}}^{\omega_i} \text{ and } C_{\text{conv}} = \max_{1 \leq i \leq N} C_{\text{conv}}^{\omega_i}.$$

III.6.1 Proof of Theorem III.3.1

Let $v \in V$ be an arbitrary function in the space V . Using (III.2), we have

$$a(u - u_{\text{ms}}, v) = a(u, v) - a(u_{\text{ms}}, v) = (f, v) - a(u_{\text{ms}}, v).$$

Then

$$a(u - u_{\text{ms}}, v) = (f, v) - a(u_{\text{ms}}, v) = (f, v - \Pi v) + (f, \Pi v) - a(u_{\text{ms}}, \Pi v) - a(u_{\text{ms}}, v - \Pi v).$$

Thus, using (III.3), we have

$$a(u - u_{\text{ms}}, v) = (f, v - \Pi v) - a(u_{\text{ms}}, v - \Pi v). \quad (\text{III.21})$$

Writing (III.21) as a sum over coarse regions,

$$a(u - u_{\text{ms}}, v) = \sum_{i=1}^N \left(\int_{\omega_i} f(v - P_i v) \chi_i - \int_{\omega_i} a \nabla u_{\text{ms}} \cdot \nabla ((v - P_i v) \chi_i) \right). \quad (\text{III.22})$$

Using the definition of Q_i , we see that (III.22) can be written as

$$a(u - u_{\text{ms}}, v) = \sum_{i=1}^N Q_i(v - P_i v).$$

Thus, we have

$$a(u - u_{\text{ms}}, v) \leq \sum_{i=1}^N \|Q_i\| \|v - P_i v\|_{L^2(\omega_i)}.$$

Using the definition of $\tilde{\kappa}_i$, we have

$$a(u - u_{\text{ms}}, v) \leq \sum_{i=1}^N (\tilde{\kappa}_i)^{-\frac{1}{2}} \|Q_i\| \|\tilde{\kappa}_i^{\frac{1}{2}}(v - P_i v)\|_{L^2(\omega_i)}.$$

Thus, by the definition of the eigenvalue problem (II.8),

$$a(u - u_{\text{ms}}, v) \leq \sum_{i=1}^N (\tilde{\kappa}_i)^{-\frac{1}{2}} (\lambda_{l_i+1}^{\omega_i})^{-\frac{1}{2}} \|Q_i\| \|v\|_{V_i}.$$

The inequality (III.8) is then followed by taking $v = u - u_{\text{ms}}$ and $\sum_{i=1}^N \|v\|_{V_i}^2 \leq C \|v\|_V^2$.

Using the definition of R_i , we see that (III.22) can be written as

$$a(u - u_{\text{ms}}, v) = \sum_{i=1}^N R_i(\chi_i(v - P_i v)).$$

Thus, we have

$$a(u - u_{\text{ms}}, v) \leq \sum_{i=1}^N \|R_i\|_{V_i^*} \|\chi_i(v - P_i v)\|_{V_i}.$$

Using (III.20),

$$a(u - u_{\text{ms}}, v) \leq C_{\text{conv}} \sum_{i=1}^N \|R_i\|_{V_i^*} (\lambda_{l_i+1}^{\omega_i})^{-\frac{1}{2}} \|v\|_{V_i}.$$

The inequality (III.9) is then followed by taking $v = u - u_{\text{ms}}$ and $\sum_{i=1}^N \|v\|_{V_i}^2 \leq C \|v\|_V^2$.

III.6.2 Some auxiliary lemmas

In this section, we will prove some auxiliary lemmas which are required for the proof of the convergence of the adaptive enrichment algorithm stated in Theorem III.3.3. We use the notation P_i^m to denote the projection operator P_i at the enrichment level m . Specifically, we define

$$P_i^m v = \sum_{k=1}^{l_i^m} \left(\int_{\omega_i} \tilde{\kappa} v \psi_k^{\omega_i, \text{off}} \right) \psi_k^{\omega_i, \text{off}}.$$

In Theorem III.3.1, we see that $\|R_i\|_{V_i^*}$ gives an upper bound of the energy error $\|u - u_{\text{ms}}\|_V$. We will first show that, $\|R_i\|_{V_i^*}$ is also a lower bound up to a correction term. To state this precisely, we define

$$S_m(\omega_i) = (\lambda_{l_i^m+1}^{\omega_i})^{-\frac{1}{2}} \sup_{v \in V_i} \frac{|R_i(v - (P_i^{m+1} v) \chi_i)|}{\|v\|_{V_i}}, \quad (\text{III.23})$$

which is a measure on how small $(v - \chi_i P_i^{m+1} v)$ is. Notice that the residual R_i is

computed using the solution u_{ms}^m obtained at enrichment level m . We omit the index m in R_i to simplify notations. Next, we will prove the following lemma.

Lemma III.6.1. *We have*

$$\|R_i\|_{V_i^*}^2 (\lambda_{l_i^m+1}^{\omega_i})^{-1} \leq 2(C_{\text{stab}}^{\omega_i})^2 (\lambda_{l_i^m+1}^{\omega_i})^{-1} \|u_{\text{ms}}^{m+1} - u_{\text{ms}}^m\|_{V_i}^2 + 2S_m(\omega_i)^2. \quad (\text{III.24})$$

Proof. By linearity

$$R_i(v) = R_i(\chi_i(P_i^{m+1}v)) + R_i(v - \chi_i(P_i^{m+1}v)).$$

Since $\chi_i(P_i^{m+1}v)$ is a test function in the space V_{off}^{m+1} , by the definition of R_i and (III.10), we have

$$\begin{aligned} R_i(\chi_i(P_i^{m+1}v)) &= \int_{\omega_i} f(P_i^{m+1}v)\chi_i - \int_{\omega_i} a \nabla u_{\text{ms}}^m \cdot \nabla((P_i^{m+1}v)\chi_i) \\ &= \int_{\omega_i} a \nabla u_{\text{ms}}^{m+1} \cdot \nabla((P_i^{m+1}v)\chi_i) - \int_{\omega_i} a \nabla u_{\text{ms}}^m \cdot \nabla((P_i^{m+1}v)\chi_i). \end{aligned}$$

Using the stability estimate (III.19),

$$R_i(\chi_i(P_i^{m+1}v)) \leq \|u_{\text{ms}}^{m+1} - u_{\text{ms}}^m\|_{V_i} \| (P_i^{m+1}v)\chi_i \|_{V_i} \leq C_{\text{stab}}^{\omega_i} \|u_{\text{ms}}^{m+1} - u_{\text{ms}}^m\|_{V_i} \|v\|_{V_i}.$$

Thus, we obtain

$$\|R_i\|_{V_i^*} \leq C_{\text{stab}}^{\omega_i} \|u_{\text{ms}}^{m+1} - u_{\text{ms}}^m\|_{V_i} + \sup_{v \in V_i} \frac{|R_i(v - (P_i^{m+1}v)\chi_i)|}{\|v\|_{V_i}}. \quad (\text{III.25})$$

The inequality (III.24) follows from the definition of $S_m(\omega_i)$. \square

We remark that one can replace u_{ms}^{m+1} by u_{snap} and P_i^{m+1} by P_i^{snap} , where P_i^{snap}

is the projection onto the snapshot space defined by

$$P_i^{\text{snap}} v = \sum_{k=1}^{W_i} \left(\int_{\omega_i} \tilde{\kappa} v \psi_k^{\omega_i, \text{off}} \right) \psi_k^{\omega_i, \text{off}}.$$

We also define $S(\omega_i)$ by

$$S(\omega_i) = (\lambda_{l_i^m+1}^{\omega_i})^{-\frac{1}{2}} \sup_{v \in V_i} \frac{|R_i(v - (P_i^{\text{snap}} v) \chi_i)|}{\|v\|_{V_i}}. \quad (\text{III.26})$$

Following the proof of the above lemma, we get

$$\|R_i\|_{V_i^*}^2 (\lambda_{l_i^m+1}^{\omega_i})^{-1} \leq 2(C_{\text{stab}}^{\omega_i})^2 (\lambda_{l_i^m+1}^{\omega_i})^{-1} \|u_{\text{snap}} - u_{\text{ms}}^m\|_{V_i}^2 + 2S(\omega_i)^2,$$

which suggests that $\|R_i\|_{V_i^*}^2 (\lambda_{l_i^m+1}^{\omega_i})^{-1}$ gives a lower bound of the error $\|u_{\text{snap}} - u_{\text{ms}}^m\|_{V_i}^2$ up to a correction term $S(\omega_i)^2$.

To prove Theorem III.3.3, we will need the following recursive properties for $S_m(\omega_i)$.

Lemma III.6.2. *For any $\alpha_R > 0$, we have*

$$S_{m+1}(\omega_i)^2 \leq (1 + \alpha_R) C_R \frac{\lambda_{l_i^m+1}^{\omega_i}}{\lambda_{l_i^{m+1}+1}^{\omega_i}} S_m(\omega_i)^2 + (1 + \alpha_R^{-1}) D_R (\lambda_{l_i^{m+1}+1}^{\omega_i})^{-1} \|u_{\text{ms}}^{m+1} - u_{\text{ms}}^m\|_{V_i}^2, \quad (\text{III.27})$$

where the enrichment level dependent constants C_R and D_R are defined by

$$C_R = (1 + 2C_{\text{conv}}^{\omega_i} (\lambda_{l_i^m+1}^{\omega_i})^{-\frac{1}{2}} (\lambda_{l_i^{m+1}+1}^{\omega_i})^{-\frac{1}{2}})^2 \text{ and } D_R = (C_{\text{stab}}^{\omega_i})^2 (1 + 2C_{\text{conv}}^{\omega_i} (\lambda_{l_i^{m+1}+1}^{\omega_i})^{-\frac{1}{2}})^2.$$

Proof. By direct calculation, we have

$$\begin{aligned}
& \int_{\omega_i} f(v - (P_i^{m+2}v)\chi_i) - \int_{\omega_i} a \nabla u_{\text{ms}}^{m+1} \cdot \nabla (v - (P_i^{m+2}v)\chi_i) \\
&= \int_{\omega_i} f(v - (P_i^{m+1}v)\chi_i) - \int_{\omega_i} a \nabla u_{\text{ms}}^m \cdot \nabla (v - (P_i^{m+1}v)\chi_i) \\
&\quad - \int_{\omega_i} a \nabla (u_{\text{ms}}^{m+1} - u_{\text{ms}}^m) \cdot \nabla (v - (P_i^{m+2}v)\chi_i) \\
&\quad + \int_{\omega_i} f(P_i^{m+1}v - P_i^{m+2}v)\chi_i - \int_{\omega_i} a \nabla u_{\text{ms}}^m \cdot \nabla ((P_i^{m+1}v - P_i^{m+2}v)\chi_i).
\end{aligned} \tag{III.28}$$

By definition of $S_m(\omega_i)$, we have

$$S_m(\omega_i) = (\lambda_{l_i^{m+1}+1}^{\omega_i})^{-\frac{1}{2}} \sup_{v \in V_i} \frac{|\int_{\omega_i} f(v - (P_i^{m+1}v)\chi_i) - \int_{\omega_i} a \nabla u_{\text{ms}}^m \cdot \nabla (v - (P_i^{m+1}v)\chi_i)|}{\|v\|_{V_i}}. \tag{III.29}$$

Multiplying (III.28) by $(\lambda_{l_i^{m+1}+1}^{\omega_i})^{-\frac{1}{2}} \|v\|_{V_i}^{-1}$ and taking supremum with respect to v , we have

$$S_{m+1}(\omega_i) \leq \left(\frac{\lambda_{l_i^{m+1}+1}^{\omega_i}}{\lambda_{l_i^{m+1}+1}^{\omega_i}}\right)^{\frac{1}{2}} S_m(\omega_i) + I_1 + I_2, \tag{III.30}$$

where

$$I_1 = (\lambda_{l_i^{m+1}+1}^{\omega_i})^{-\frac{1}{2}} \sup_{v \in V_i} \frac{|-\int_{\omega_i} a \nabla (u_{\text{ms}}^{m+1} - u_{\text{ms}}^m) \cdot \nabla (v - (P_i^{m+2}v)\chi_i)|}{\|v\|_{V_i}}$$

and

$$\begin{aligned}
& I_2 = \\
& (\lambda_{l_i^{m+1}+1}^{\omega_i})^{-\frac{1}{2}} \sup_{v \in V_i} \frac{|\int_{\omega_i} f(P_i^{m+1}v - P_i^{m+2}v)\chi_i - \int_{\omega_i} a \nabla u_{\text{ms}}^m \cdot \nabla ((P_i^{m+1}v - P_i^{m+2}v)\chi_i)|}{\|v\|_{V_i}}.
\end{aligned}$$

To estimate I_1 , we use the stability estimate (III.19) to obtain

$$\begin{aligned}
& \int_{\omega_i} a \nabla(u_{\text{ms}}^{m+1} - u_{\text{ms}}^m) \cdot \nabla(v - (P_i^{m+2}v)\chi_i) \\
&= \int_{\omega_i} a \nabla(u_{\text{ms}}^{m+1} - u_{\text{ms}}^m) \cdot \nabla v - \int_{\omega_i} a \nabla(u_{\text{ms}}^{m+1} - u_{\text{ms}}^m) \cdot \nabla((P_i^{m+2}v)\chi_i) \\
&\leq C_{\text{stab}}^{\omega_i} \|u_{\text{ms}}^{m+1} - u_{\text{ms}}^m\|_{V_i} \|v\|_{V_i},
\end{aligned}$$

which implies

$$I_1 \leq C_{\text{stab}}^{\omega_i} (\lambda_{l_i^{m+1}+1}^{\omega_i})^{-\frac{1}{2}} \|u_{\text{ms}}^{m+1} - u_{\text{ms}}^m\|_{V_i}.$$

To estimate I_2 , we use the definition of R_i to obtain

$$I_2 \leq (\lambda_{l_i^{m+1}+1}^{\omega_i})^{-\frac{1}{2}} \|R_i\|_{V_i^*} \sup_{v \in V_i} \frac{\|\chi_i(P_i^{m+1}v - P_i^{m+2}v)\|_{V_i}}{\|v\|_{V_i}}.$$

By the convergence bound (III.20) and the fact that $\lambda_{l_i^{m+1}+1}^{\omega_i} < \lambda_{l_i^{m+2}+1}^{\omega_i}$, we have

$$\begin{aligned}
\|\chi_i(P_i^{m+1}v - P_i^{m+2}v)\|_{V_i} &\leq \|\chi_i(P_i^{m+1}v - v)\|_{V_i} + \|\chi_i(v - P_i^{m+2}v)\|_{V_i} \\
&\leq 2C_{\text{conv}}^{\omega_i} (\lambda_{l_i^{m+1}+1}^{\omega_i})^{-\frac{1}{2}} \|v\|_{V_i},
\end{aligned}$$

which implies

$$I_2 \leq 2C_{\text{conv}}^{\omega_i} (\lambda_{l_i^{m+1}+1}^{\omega_i})^{-1} \|R_i\|_{V_i^*}.$$

Combining results and using (III.30), we get

$$\begin{aligned}
S_{m+1}(\omega_i) &\leq \left(\frac{\lambda_{l_i^{m+1}+1}^{\omega_i}}{\lambda_{l_i^{m+1}+1}^{\omega_i}}\right)^{\frac{1}{2}} S_m(\omega_i) + C_{\text{stab}}^{\omega_i} (\lambda_{l_i^{m+1}+1}^{\omega_i})^{-\frac{1}{2}} \|u_{\text{ms}}^{m+1} - u_{\text{ms}}^m\|_{V_i} \\
&\quad + 2C_{\text{conv}}^{\omega_i} (\lambda_{l_i^{m+1}+1}^{\omega_i})^{-1} \|R_i\|_{V_i^*}.
\end{aligned}$$

Using (III.25) and the definition of $S_m(\omega_i)$,

$$\begin{aligned} S_{m+1}(\omega_i) \leq & (1 + 2C_{\text{conv}}^{\omega_i}(\lambda_{l_i^m+1}^{\omega_i})^{-\frac{1}{2}}(\lambda_{l_i^{m+1}+1}^{\omega_i})^{-\frac{1}{2}})(\frac{\lambda_{l_i^m+1}^{\omega_i}}{\lambda_{l_i^{m+1}+1}^{\omega_i}})^{\frac{1}{2}}S_m(\omega_i) \\ & + C_{\text{stab}}^{\omega_i}(\lambda_{l_i^{m+1}+1}^{\omega_i})^{-\frac{1}{2}}(1 + 2C_{\text{conv}}^{\omega_i}(\lambda_{l_i^{m+1}+1}^{\omega_i})^{-\frac{1}{2}})\|u_{\text{ms}}^{m+1} - u_{\text{ms}}^m\|_{V_i}. \end{aligned}$$

Hence, (III.27) is proved. \square

Next, we consider the L^2 -based residual Q_i and prove similar inequalities. We define

$$S_m(\omega_i) = (\tilde{\kappa}_i \lambda_{l_i^m+1}^{\omega_i})^{-\frac{1}{2}} \sup_{v \in L^2(\omega_i)} \frac{|Q_i(v - P_i^{m+1}v)|}{\|v\|_{L^2(\omega_i)}}, \quad (\text{III.31})$$

which is a measure on how small $(v - P_i^{m+1}v)$ is. Notice that the residual Q_i is computed using the solution u_{ms}^m obtained at enrichment level m . We omit the index m in Q_i to simplify notations. We also note that we have used the same notation $S_m(\omega_i)$ as the case for the H^{-1} -based residual to again simplify notations. It will be clear which residual we are referring to when the notation $S_m(\omega_i)$ appears in the text. We define the jump of the coefficient in each coarse region by

$$\beta_i = \frac{\max_{x \in \omega_i} \kappa(x)}{\min_{x \in \omega_i} \kappa(x)}.$$

Next, we will prove the following lemma.

Lemma III.6.3. *We have*

$$\|Q_i\|^2 (\tilde{\kappa}_i \lambda_{l_i^m+1}^{\omega_i})^{-1} \leq 2(C_{\text{inv}} \beta_i^{\frac{1}{2}} h^{-1})^2 (\lambda_{l_i^m+1}^{\omega_i})^{-1} \|u_{\text{ms}}^{m+1} - u_{\text{ms}}^m\|_{V_i}^2 + 2S_m(\omega_i)^2. \quad (\text{III.32})$$

Proof. By linearity

$$Q_i(v) = Q_i(P_i^{m+1}v) + Q_i(v - P_i^{m+1}v).$$

By the definition of Q_i and (III.10), we have

$$\begin{aligned} Q_i(P_i^{m+1}v) &= \int_{\omega_i} f(P_i^{m+1}v)\chi_i - \int_{\omega_i} a\nabla u_{\text{ms}}^m \cdot \nabla((P_i^{m+1}v)\chi_i) \\ &= \int_{\omega_i} a\nabla u_{\text{ms}}^{m+1} \cdot \nabla((P_i^{m+1}v)\chi_i) - \int_{\omega_i} a\nabla u_{\text{ms}}^m \cdot \nabla((P_i^{m+1}v)\chi_i), \end{aligned}$$

which implies

$$Q_i(P_i^{m+1}v) \leq \|u_{\text{ms}}^{m+1} - u_{\text{ms}}^m\|_{V_i} \|(P_i^{m+1}v)\chi_i\|_{V_i}.$$

Using the inverse inequality,

$$\|(P_i^{m+1}v)\chi_i\|_{V_i} \leq C_{\text{inv}}h^{-1}\|\tilde{\kappa}^{\frac{1}{2}}P_i^{m+1}v\|_{L^2(\omega_i)} \leq C_{\text{inv}}h^{-1}\|\tilde{\kappa}^{\frac{1}{2}}v\|_{L^2(\omega_i)},$$

where C_{inv} is independent of the mesh size. Thus, we obtain

$$(\tilde{\kappa}_i)^{-\frac{1}{2}}\|Q_i\|_{V_i^*} \leq C_{\text{inv}}\beta_i^{\frac{1}{2}}h^{-1}\|u_{\text{ms}}^{m+1} - u_{\text{ms}}^m\|_{V_i} + (\tilde{\kappa}_i)^{-\frac{1}{2}} \sup_{v \in L^2(\omega_i)} \frac{|Q_i(v - P_i^{m+1}v)|}{\|v\|_{L^2(\omega_i)}}. \quad (\text{III.33})$$

The inequality (III.32) follows from the definition of $S_m(\omega_i)$. \square

Next we will prove the following recursive property for $S_m(\omega_i)$. The proof follows from the same lines as Lemma III.6.2.

Lemma III.6.4. *For any $\alpha_Q > 0$, we have*

$$S_{m+1}(\omega_i)^2 \leq (1 + \alpha_Q)C_Q \frac{\lambda_{l_i^m+1}^{\omega_i}}{\lambda_{l_i^{m+1}+1}^{\omega_i}} S_m(\omega_i)^2 + (1 + \alpha_Q^{-1})D_Q(\lambda_{l_i^{m+1}+1}^{\omega_i})^{-1} \|u_{\text{ms}}^{m+1} - u_{\text{ms}}^m\|_{V_i}^2, \quad (\text{III.34})$$

where the enrichment level dependent constants C_R and D_R are defined by

$$C_Q = (1 + \beta_i^{\frac{1}{2}})^2 \quad \text{and} \quad D_Q = C_{\text{inv}}\beta_i^{\frac{1}{2}}h^{-1}(2\tilde{\kappa}_i + \beta_i^{\frac{1}{2}}).$$

Proof. By direct calculation, we have

$$\begin{aligned}
& \int_{\omega_i} f(v - P_i^{m+2}v)\chi_i - \int_{\omega_i} a\nabla u_{\text{ms}}^{m+1} \cdot \nabla((v - P_i^{m+2}v)\chi_i) \\
&= \int_{\omega_i} f(v - P_i^{m+1}v)\chi_i - \int_{\omega_i} a\nabla u_{\text{ms}}^m \cdot \nabla((v - P_i^{m+1}v)\chi_i) \\
&\quad - \int_{\omega_i} a\nabla(u_{\text{ms}}^{m+1} - u_{\text{ms}}^m) \cdot \nabla((v - P_i^{m+2}v)\chi_i) \\
&\quad + \int_{\omega_i} f(P_i^{m+1}v - P_i^{m+2}v)\chi_i - \int_{\omega_i} a\nabla u_{\text{ms}}^m \cdot \nabla((P_i^{m+1}v - P_i^{m+2}v)\chi_i).
\end{aligned} \tag{III.35}$$

By definition of $S_m(\omega_i)$, we have

$$S_m(\omega_i) = (\tilde{\kappa}_i \lambda_{l_i^m+1}^{\omega_i})^{-\frac{1}{2}} \sup_{v \in L^2(\omega_i)} \frac{|\int_{\omega_i} f(v - P_i^{m+1}v)\chi_i - \int_{\omega_i} a\nabla u_{\text{ms}}^m \cdot \nabla((v - P_i^{m+1}v)\chi_i)|}{\|v\|_{L^2(\omega_i)}}. \tag{III.36}$$

Multiplying (III.35) by $(\tilde{\kappa}_i \lambda_{l_i^{m+1}+1}^{\omega_i})^{-\frac{1}{2}} \|v\|_{L^2(\omega_i)}^{-1}$ and taking supremum with respect to v , we have

$$S_{m+1}(\omega_i) \leq \left(\frac{\lambda_{l_i^{m+1}+1}^{\omega_i}}{\lambda_{l_i^m+1}^{\omega_i}}\right)^{\frac{1}{2}} S_m(\omega_i) + I_1 + I_2, \tag{III.37}$$

where

$$I_1 = (\tilde{\kappa}_i \lambda_{l_i^{m+1}+1}^{\omega_i})^{-\frac{1}{2}} \sup_{v \in L^2(\omega_i)} \frac{|-\int_{\omega_i} a\nabla(u_{\text{ms}}^{m+1} - u_{\text{ms}}^m) \cdot \nabla((v - P_i^{m+2}v)\chi_i)|}{\|v\|_{L^2(\omega_i)}}$$

and

$$I_2 = (\tilde{\kappa}_i \lambda_{l_i^{m+1}+1}^{\omega_i})^{-\frac{1}{2}} \sup_{v \in L^2(\omega_i)} \frac{|Y_i(v)|}{\|v\|_{L^2(\omega_i)}}.$$

Here,

$$Y_i(v) = \int_{\omega_i} f(P_i^{m+1}v - P_i^{m+2}v)\chi_i - \int_{\omega_i} a\nabla u_{\text{ms}}^m \cdot \nabla((P_i^{m+1}v - P_i^{m+2}v)\chi_i).$$

To estimate I_1 , we use the inverse inequality to obtain

$$\int_{\omega_i} a \nabla(u_{\text{ms}}^{m+1} - u_{\text{ms}}^m) \cdot \nabla(v - (P_i^{m+2}v)\chi_i) \leq 2C_{\text{inv}} h^{-1} \|u_{\text{ms}}^{m+1} - u_{\text{ms}}^m\|_{V_i} \|\tilde{\kappa}^{\frac{1}{2}} v\|_{L^2(\omega_i)},$$

which implies

$$I_1 \leq 2C_{\text{inv}} (\tilde{\kappa}_i \lambda_{l_i^{m+1}+1}^{\omega_i})^{-\frac{1}{2}} \beta_i^{\frac{1}{2}} h^{-1} \|u_{\text{ms}}^{m+1} - u_{\text{ms}}^m\|_{V_i}.$$

To estimate I_2 , we use the definition of Q_i to obtain

$$I_2 \leq (\tilde{\kappa}_i \lambda_{l_i^{m+1}+1}^{\omega_i})^{-\frac{1}{2}} \|Q_i\| \sup_{v \in L^2(\omega_i)} \frac{\|P_i^{m+1}v - P_i^{m+2}v\|}{\|v\|_{L^2(\omega_i)}},$$

which implies

$$I_2 \leq (\tilde{\kappa}_i \lambda_{l_i^{m+1}+1}^{\omega_i})^{-\frac{1}{2}} \beta_i^{\frac{1}{2}} \|Q_i\|.$$

Combining results and using (III.37), we get

$$\begin{aligned} S_{m+1}(\omega_i) &\leq \left(\frac{\lambda_{l_i^{m+1}+1}^{\omega_i}}{\lambda_{l_i^{m+1}+1}^{\omega_i}}\right)^{\frac{1}{2}} S_m(\omega_i) + 2C_{\text{inv}} (\tilde{\kappa}_i \lambda_{l_i^{m+1}+1}^{\omega_i})^{-\frac{1}{2}} \beta_i^{\frac{1}{2}} h^{-1} \|u_{\text{ms}}^{m+1} - u_{\text{ms}}^m\|_{V_i} \\ &\quad + (\tilde{\kappa}_i \lambda_{l_i^{m+1}+1}^{\omega_i})^{-\frac{1}{2}} \beta_i^{\frac{1}{2}} \|Q_i\|. \end{aligned}$$

Using (III.33),

$$S_{m+1}(\omega_i) \leq (1 + \beta_i^{\frac{1}{2}}) \left(\frac{\lambda_{l_i^{m+1}+1}^{\omega_i}}{\lambda_{l_i^{m+1}+1}^{\omega_i}}\right)^{\frac{1}{2}} S_m(\omega_i) + C_{\text{inv}} (\lambda_{l_i^{m+1}+1}^{\omega_i})^{-\frac{1}{2}} \beta_i^{\frac{1}{2}} h^{-1} (2\tilde{\kappa}_i + \beta_i^{\frac{1}{2}}) \|u_{\text{ms}}^{m+1} - u_{\text{ms}}^m\|_{V_i}.$$

Hence, (III.34) is proved. \square

III.6.3 Proof of Theorem III.3.3

In this section, we prove the convergence of the adaptive enrichment algorithm.

We will give a unified proof for both the L^2 -based and H^{-1} -based residuals. First of

all, we use η_i as a unified notation for the residuals, namely,

$$\eta_i^2 = \begin{cases} \|Q_i\|^2 (\tilde{\kappa}_i \lambda_{l_i^m+1}^{\omega_i})^{-1}, & \text{for } L^2\text{-based residual,} \\ \|R_i\|_{V_i^*}^2 (\lambda_{l_i^m+1}^{\omega_i})^{-1}, & \text{for } H^{-1}\text{-based residual.} \end{cases}$$

Then Lemma III.6.1 and Lemma III.6.3 can be written as

$$\eta_i^2 \leq B_i (\lambda_{l_i^m+1}^{\omega_i})^{-1} \|u_{\text{ms}}^{m+1} - u_{\text{ms}}^m\|_{V_i}^2 + 2S_m(\omega_i)^2, \quad (\text{III.38})$$

where the constant B_i is given by

$$B_i = \begin{cases} 2(C_{\text{inv}} \beta_i^{\frac{1}{2}} h^{-1})^2, & \text{for } L^2\text{-based residual} \\ 2(C_{\text{stab}}^{\omega_i, m+1})^2, & \text{for } H^{-1}\text{-based residual.} \end{cases}$$

We remark that the definitions of $S_m(\omega_i)$ are given in (III.31) and (III.23) for the L^2 -based and H^{-1} -based residuals respectively. Moreover, Lemma III.6.2 and Lemma III.6.4 can be unified as

$$S_{m+1}(\omega_i)^2 \leq (1 + \alpha_S) C_S \frac{\lambda_{l_i^{m+1}+1}^{\omega_i}}{\lambda_{l_i^{m+1}+1}^{\omega_i}} S_m(\omega_i)^2 + (1 + \alpha_S^{-1}) D_S (\lambda_{l_i^{m+1}+1}^{\omega_i})^{-1} \|u_{\text{ms}}^{m+1} - u_{\text{ms}}^m\|_{V_i}^2, \quad (\text{III.39})$$

where $\alpha_S = \alpha_Q, C_S = C_Q$ and $D_S = D_Q$ for the L^2 -based residual while $\alpha_S = \alpha_R, C_S = C_R$ and $D_S = D_R$ for the H^{-1} -based residual. Notice that $\alpha_S > 0$ is a constant defined uniformly over coarse regions and is to be determined. The convergence proof is based on (III.38) and (III.39).

Let $0 < \theta < 1$. We choose an index set I so that

$$\theta^2 \sum_{i=1}^N \eta_i^2 \leq \sum_{i \in I} \eta_i^2. \quad (\text{III.40})$$

We also assume there is a real number γ with $0 < \gamma < 1$ satisfies

$$\gamma^2 \sum_{i=1}^n S_m(\omega_i)^2 \leq \sum_{i \in I} S_m(\omega_i)^2. \quad (\text{III.41})$$

We will then add basis function for those ω_i with $i \in I$. Then, using Theorem III.3.1 and (III.40), we have

$$\theta^2 \|u - u_{\text{ms}}^m\|_V^2 \leq \theta^2 C_{\text{err}} \sum_{i=1}^N \eta_i^2 \leq C_{\text{err}} \sum_{i \in I} \eta_i^2.$$

By (III.38),

$$\theta^2 \|u - u_{\text{ms}}^m\|_V^2 \leq 2C_{\text{err}} \sum_{i=1}^N S_m(\omega_i)^2 + L_1 \|u_H^{m+1} - u_H^m\|_V^2,$$

where

$$L_1 = C_{\text{err}} \max_{1 \leq i \leq N} \left(B_i(\lambda_{l_i^m+1}^{\omega_i})^{-1} \right). \quad (\text{III.42})$$

Note that, by Galerkin orthogonality, we have

$$\|u_{\text{ms}}^{m+1} - u_{\text{ms}}^m\|_V^2 = \|u - u_{\text{ms}}^m\|_V^2 - \|u - u_{\text{ms}}^{m+1}\|_V^2.$$

So, we have

$$\theta^2 \|u - u_{\text{ms}}^m\|_V^2 \leq 2C_{\text{err}} \sum_{i=1}^N S_m(\omega_i)^2 + L_1 (\|u - u_H^m\|_V^2 - \|u - u_H^{m+1}\|_V^2),$$

which implies

$$\|u - u_{\text{ms}}^{m+1}\|_V^2 \leq \left(1 - \frac{\theta^2}{L_1}\right) \|u - u_{\text{ms}}^m\|_V^2 + \frac{2C_{\text{err}}}{L_1} \sum_{i=1}^N S_m(\omega_i)^2. \quad (\text{III.43})$$

On the other hand,

$$\sum_{i=1}^N S_{m+1}(\omega_i)^2 = \sum_{i \in I} S_{m+1}(\omega_i)^2 + \sum_{i \neq I} S_{m+1}(\omega_i)^2.$$

By (III.39) and that $S_{m+1}(\omega_i) = S_m(\omega_i)$ for $i \neq I$, we have

$$\begin{aligned} \sum_{i=1}^N S_{m+1}(\omega_i)^2 &\leq \sum_{i \in I} \left((1 + \alpha_S) C_S \frac{\lambda_{l_i^m+1}^{\omega_i}}{\lambda_{l_i^{m+1}+1}^{\omega_i}} S_m(\omega_i)^2 \right. \\ &\quad \left. + (1 + \alpha_S^{-1}) D_S (\lambda_{l_i^{m+1}+1}^{\omega_i})^{-1} \|u_{\text{ms}}^{m+1} - u_{\text{ms}}^m\|_{V_i}^2 \right) + \sum_{i \neq I} S_m(\omega_i)^2. \end{aligned}$$

We assume the enrichment is obtained so that

$$\delta = C_S \max_{1 \leq i \leq N} \frac{\lambda_{l_i^m+1}^{\omega_i}}{\lambda_{l_i^{m+1}+1}^{\omega_i}} < 1.$$

We then have

$$\sum_{i=1}^N S_{m+1}(\omega_i)^2 \leq (1 + \alpha_S) \sum_{i=1}^N S_m(\omega_i)^2 - (1 + \alpha_S)(1 - \delta) \sum_{i \in I} S_m(\omega_i)^2 + \delta L_2 \|u_{\text{ms}}^{m+1} - u_{\text{ms}}^m\|_V^2,$$

where

$$L_2 = (1 + \alpha_S^{-1}) \max_{1 \leq i \leq N} \left(D_S C_S^{-1} (\lambda_{l_i^m+1}^{\omega_i})^{-1} \right). \quad (\text{III.44})$$

By assumption on γ ,

$$\sum_{i=1}^N S_{m+1}(\omega_i)^2 \leq (1 + \alpha_S) \sum_{i=1}^N S_m(\omega_i)^2 - (1 + \alpha_S)(1 - \delta) \gamma^2 \sum_{i=1}^N S_m(\omega_i)^2 + \delta L_2 \|u_{\text{ms}}^{m+1} - u_{\text{ms}}^m\|_V^2.$$

Let $\rho = (1 + \alpha_S)(1 - (1 - \delta)\gamma^2)$. We choose $\alpha_S > 0$ small so that $0 < \rho < 1$. The

above is then written as

$$\sum_{i=1}^N S_{m+1}(\omega_i)^2 \leq \rho \sum_{i=1}^N S_m(\omega_i)^2 + \delta L_2 (\|u - u_{\text{ms}}^m\|_V^2 - \|u - u_{\text{ms}}^{m+1}\|_V^2). \quad (\text{III.45})$$

Next, we take a constant τ so that

$$\tau > 0, \quad \frac{2C_{\text{err}}}{\tau L_1} + \rho < 1.$$

Finally, we combine (III.43) and (III.45) to obtain the following

$$\begin{aligned} \|u - u_{\text{ms}}^{m+1}\|_V^2 + \tau \sum_{i=1}^N S_{m+1}(\omega_i)^2 &\leq (1 - \frac{\theta^2}{L_1}) \|u - u_{\text{ms}}^m\|_V^2 + \frac{2C_{\text{err}}}{L_1} \sum_{i=1}^N S_m(\omega_i)^2 \\ &+ \tau \rho \sum_{i=1}^N S_m(\omega_i)^2 + \tau \delta L_2 (\|u - u_{\text{ms}}^m\|_V^2 - \|u - u_{\text{ms}}^{m+1}\|_V^2). \end{aligned}$$

Rearranging the terms, we have

$$\begin{aligned} (1 + \tau \delta L_2) \|u - u_{\text{ms}}^{m+1}\|_V^2 + \tau \sum_{i=1}^N S_{m+1}(\omega_i)^2 &\leq (1 - \frac{\theta^2}{L_1} + \tau \delta L_2) \|u - u_{\text{ms}}^m\|_V^2 \\ &+ (\frac{2C_{\text{err}}}{L_1} + \tau \rho) \sum_{i=1}^N S_m(\omega_i)^2. \end{aligned}$$

Hence we obtain

$$\begin{aligned} \|u - u_{\text{ms}}^{m+1}\|_V^2 + \frac{\tau}{1 + \tau \delta L_2} \sum_{i=1}^N S_{m+1}(\omega_i)^2 &\leq (1 - \frac{\theta^2}{L_1(1 + \tau \delta L_2)}) \|u - u_{\text{ms}}^m\|_V^2 \\ &+ \frac{\tau}{1 + \tau \delta L_2} (\frac{2C_{\text{err}}}{\tau L_1} + \rho) \sum_{i=1}^N S_m(\omega_i)^2. \end{aligned}$$

III.7 Concluding remarks

In this chapter, we derive an a posteriori error estimate for the Generalized Multiscale Finite Element Method (GMsFEM). In particular, we study an adaptive spectral enrichment procedure and derive an error indicator which gives an estimate of the local error over coarse grid regions.

We consider two kinds of error indicators where one is based on the L^2 -norm of the local residual and the other is based on the weighted H^{-1} -norm of the local residual, where the weight is related to the coefficient of the elliptic equation. We show that the use of weighted H^{-1} -norm residual gives a more robust error indicator which works well for cases with high contrast multiscale problems. The convergence analysis of the method is given.

Numerical results are presented that demonstrate the robustness of the proposed error indicators. We show the convergence of the proposed indicators and their similarities to the ones when exact solution is used in the indicator. We compare the performance of the weighted H^{-1} -based indicator with that of the L^2 -based indicator for high-contrast problems. Our numerical results show that the former is more appropriate for high-contrast multiscale problems.

Although the results presented in this chapter are encouraging, there is scope for further exploration. As our intent here was to derive and demonstrate the robustness of error indicators for challenging high-contrast multiscale problems, we did not consider the fine-grid discretization error and assumed that the coarse-grid error is the main contributor, and thus assuming that the fine-grid solution is the desired quantity. In general when solving continuous PDEs, one can also add fine-grid discretization errors due to basis computations. This will be a subject of our future research.

IV. GENERALIZED MULTISCALE FINITE ELEMENT METHODS. NONLINEAR ELLIPTIC PROBLEMS

IV.1 Introduction

In this chapter, we extend the GMsFEM to nonlinear elliptic problems in heterogeneous high-contrast media (see [39]). We apply a Picard iteration and treat an upscaled quantity of a previous solution iterate as a parameter in the problem. With this convention, we follow an offline-online procedure in which the coarse space construction is split into two distinct stages; offline and online (see [14, 16, 29, 62, 68]).

The main goal of this approach is to allow for the efficient construction of an online space (and an online solution) for each fixed parameter value and iteration. In the process, we precompute a larger-dimensional, *parameter-independent* offline space that accounts for an appropriate range of parameter values that may be used in the online stage. As construction of the offline space will constitute a one-time preprocessing step, only the online space will require additional work within the solution procedure. In the offline stage we first choose a fixed set of parameter values and generate an associated set of “snapshot” functions by solving localized problems on specified coarse subdomains. The functions obtained through this step constitute a snapshot space which will be used in the offline space construction. To construct the offline space we solve localized eigenvalue problems that use averaged quantities of the parameter(s) of interest within the space of snapshots. We then keep a certain number of eigenfunctions (based on some criterion) to form the offline space. At the online stage we solve similar localized problems using a fixed parameter value within the offline space, and keep a certain number of eigenfunctions for the online space construction.

We remark that the underlying machinery of the proposed technique incorporates some ideas from the reduced-basis (RB) community (see, e.g., [6, 7, 29, 27, 57]), where computations are split into offline and online stages. In particular, the concept of the offline stage is typically devoted to the construction of a reduced basis set which captures the relevant behavior of the parameter dependence. As a result, the online solutions may be quickly obtained through the use of a precomputed (or adaptively computed) surrogate space. The proposed method may be regarded as a local model reduction approach for nonlinear elliptic equations (see also [6, 4, 29] for some related work). In [6] the authors present a related approach for treating linear problems, in which reduced-basis computations are performed to increase the efficiency of solving localized cell problems. As a result, for the local online computations the authors are able to quickly obtain effective cell properties that are required of the high-order coarse scale discretizations. A reduced-basis approach for treating nonlinear problems (parabolic and hyperbolic) is offered in [29]. In this work, the authors decompose the nonlinear operator into distinct contributions (parameter-independent and -dependent) using so-called empirical operator interpolation. The reduced-basis spaces are then constructed for the approximation of the operator, such that they are able to accurately capture the time evolution of parabolic and hyperbolic equations.

In this chapter, we consider the continuous Galerkin (CG) and discontinuous Galerkin (DG) formulations for the global coupling of the online basis functions. We show that each method offers a suitable solution technique, however, at this point we highlight some distinguishing characteristics of the respective methods as motivation for considering both formulations. For the nonlinear elliptic equation considered in this chapter, the CG coupling yields a bilinear form that closely resembles the standard finite element method (FEM). In particular, the integrations that define the CG formulation are taken over the whole domain, and result in a reduced-order

system of equations that is similar in nature to the fine-scale system. As such, the ease of implementation, classical FEM analogues, and well understood structure make CG a tractable method for coupling the coarse basis functions in order to solve the global problem [50]. While the discontinuous Galerkin formulation is arguably more delicate than its CG counterpart, DG offers an attractive feature such as it does not require partition of unity functions to couple basis functions. DG methods also allow for flexible meshing, and directly yield a local mass conservation property that is required for coupling to transport problems. As for the accuracy of these approaches, we observe that the error between the online and the offline solutions is comparable for CG and DG GMsFEM except in the case of very low dimensional coarse spaces. In this case, DG GMsFEM gives larger errors which are due to the penalty error. The flexibility of the coarse space enrichment, along with the choice of using CG or DG as the global coupling mechanism, makes GMsFEM a robust and suitable technique for solving the model equation that we consider. A variety of numerical examples are presented to validate the performance of the proposed method.

We note that some numerical results for GMsFEM in the context of continuous Galerkin methods for nonlinear equations are presented in [36]. These numerical results are mostly presented to demonstrate the main concepts of GMsFEM and we do not have careful studies for nonlinear problems in [36]. Moreover, the numerical results presented in [36] use reduced basis approach to identify dominant eigenmodes which is different from the local mode decomposition approach presented here. Moreover, the current chapter also studies DG approach for nonlinear equations.

The organization of the remaining of this chapter is as follows. In Section IV.2 we introduce the model problem, the iterative procedure, and notations. In Section IV.3, we carefully describe the coarse space enrichment procedure, and introduce

the continuous and discontinuous Galerkin global coupling formulations. In particular, SubSection IV.3.1 is devoted to the offline-online coarse space construction, and in SubSection IV.3.2 we describe the CG and DG global coupling procedures. A variety of numerical examples are presented in Section IV.4 to validate the performance of the proposed approaches, and in Section IV.5, we offer some concluding remarks.

IV.2 Preliminaries

We consider non-linear, elliptic equations of the form

$$-\operatorname{div}(\kappa(x; u) \nabla u) = f \text{ in } D, \quad (\text{IV.1})$$

where $u = 0$ on ∂D . We assume that u is bounded above and below, i.e., $u_0 \leq u(x) \leq u_N$, where u_0 and u_N are pre-defined constants.

In order to solve Eq. (IV.1) we will consider a Picard iteration

$$-\operatorname{div}(\kappa(x; u^n(x)) \nabla u^{n+1}(x)) = f \text{ in } D, \quad (\text{IV.2})$$

where superscripts involving n denote respective iteration levels. To discretize (IV.2), we follow the notions of fine and coarse grids introduced in Chapter II.

Next, we briefly outline the global coupling and the role of coarse basis functions for the respective formulations that we consider. For the discontinuous Galerkin (DG) formulation, we will use a coarse element K as the support for basis functions, and for the continuous Galerkin (CG) formulation, we will use ω_i as the support of basis functions. In turn, throughout this chapter, we use the notation

$$\tau = \begin{cases} \omega_i & \text{for CG} \\ K & \text{for DG} \end{cases} \quad (\text{IV.3})$$

when referring to a coarse region where respective local computations are performed (see Figure II.3). To further motivate the coarse basis construction, we offer a brief outline of the global coupling associated with the CG formulation below. For the purposes of this description, we formally denote the CG basis functions by $\psi_k^{\omega_i}$. In particular, we note that the proposed approach will employ the use of multiple basis functions per coarse neighborhood. In turn, the CG solution at n -th iteration will be sought as $u_{\text{ms}}^{\text{CG}}(x; \mu) = \sum_{i,k} c_k^i \psi_k^{\omega_i}(x; \mu)$, where $\psi_k^{\omega_i}(x; \mu)$ are the basis functions for n -th iteration, and μ is used to denote dependence on the previous solution. We note that a main consideration of our method is to allow for rapid calculations of basis functions at each iteration.

IV.3 CG and DG GMsFEM for nonlinear problems

IV.3.1 Local basis functions

To motivate the local basis construction, we introduce an approximation to the solution of Eq. (IV.2) given by

$$-\text{div}(\kappa(x; \bar{u}^n(x)) \nabla u^{n+1}(x)) = f \text{ in } D, \quad (\text{IV.4})$$

where \bar{u} denotes the average of u in each coarse region τ (recall Eq. (IV.3)) depending on the global formulation. Since the nonlinearity of the problem depends only on the solution, u^n may be treated as a scalar in each coarse subregion. As the solution is a smooth function, we can assume u^n to be approximately constant in these regions (and we use \bar{u}^n as the value). As a result, the nonlinearity may be treated through introduction of an auxiliary scalar parameter which represents the nearly constant solution dependence within the iteration. Because the variation in \bar{u}^n is not known a priori, we will use μ to represent the dependence of the solution on \bar{u}^n in the following

sections.

As part of the iterative solution process, multiscale basis functions will be computed for a selected number of the parameter values at the offline stage, and we will compute multiscale basis functions for each new value of \bar{u}^n at the online stage. For the sake of brevity, we refer to Chapter II for the construction of snapshot space, local offline space and online space. We denote the derived local online space over τ as $V_{\text{on}}^\tau(\mu)$ with dimension of M_{on}^τ . Note that we maintain the convention of denoting \bar{u} by the parameter μ . We omit the iterative index n (and $n + 1$) for additional notational brevity, although note that the iterative process should be clearly implied.

IV.3.2 Global coupling

In this section, we illustrate the global basis generation for CG and DG, separately. We will also show those two global formulations in detail.

IV.3.2.1 Continuous Galerkin coupling

In this subsection, we aim to create an appropriate solution space and variational formulation that is suitable for a continuous Galerkin approximation of Eq. (IV.4). We begin with an initial coarse space $V_0^{\text{init}}(\mu) = \text{span}\{\chi_i\}_{i=1}^{N_v}$, where the χ_i are the standard multiscale partition of unity functions defined in Eq. (II.17). We then multiply the partition of unity functions by the eigenfunctions in the online space $V_{\text{on}}^{\omega_i}(\mu)$ to construct the resulting basis functions

$$\psi_{i,k}^{\text{CG}} = \chi_i \psi_k^{\omega_i, \text{on}} \quad \text{for } 1 \leq i \leq N_v \text{ and } 1 \leq k \leq M_{\text{on}}^{\omega_i}, \quad (\text{IV.5})$$

where $M_{\text{on}}^{\omega_i}$ denotes the number of online eigenvectors that are chosen for each coarse node i . We note that the construction in Eq. (IV.5) yields inherently continuous basis functions due to the multiplication of online eigenvectors with the initial (continuous)

partition of unity. This convention is not necessary for the discontinuous Galerkin global coupling, and is a focal point of contrast between the respective methods. However, with the continuous basis functions in place, we define the continuous Galerkin spectral multiscale space as

$$V_{\text{on}}^{\text{CG}}(\mu) = \text{span}\{\psi_{i,k}^{\text{CG}} : 1 \leq i \leq N_v \text{ and } 1 \leq k \leq M_{\text{on}}^{\omega_i}\}. \quad (\text{IV.6})$$

Using a single index notation, we may write $V_{\text{on}}^{\text{CG}}(\mu) = \text{span}\{\psi_i^{\text{CG}}\}_{i=1}^{N_c}$, where N_c denotes the total number of basis functions that are used in the coarse space construction. We also construct an operator matrix $R_0^T = [\psi_1^{\text{CG}}, \dots, \psi_{N_c}^{\text{CG}}]$ (where ψ_i^{CG} are used to denote the nodal values of each basis function defined on the fine grid), for later use in this subsection.

Before introducing the continuous Galerkin formulation, we recall that the parameter μ is used to denote a solution that is computed at a previous iteration level (see Eq. (IV.4)). In turn, to update the solution at the current iteration level we seek $u_{\text{ms}}^{\text{CG}}(x; \mu) = \sum_i c_i \psi_i^{\text{CG}}(x; \mu) \in V_{\text{on}}^{\text{CG}}(\mu)$ such that

$$a^{\text{CG}}(u_{\text{ms}}^{\text{CG}}, v; \mu) = (f, v) \quad \text{for all } v \in V_{\text{on}}^{\text{CG}}(\mu), \quad (\text{IV.7})$$

where $a^{\text{CG}}(u, v; \mu) = \int_D \kappa(x; \mu) \nabla u \cdot \nabla v \, dx$, and $(f, v) = \int_D f v \, dx$. We note that variational form in (IV.7) yields the following linear algebraic system

$$A_0 U_0^{\text{CG}} = F_0, \quad (\text{IV.8})$$

where U_0^{CG} denotes the nodal values of the discrete CG solution, and

$$A_0(\mu) = [a_{IJ}] = \int_D \kappa(x; \mu) \nabla \psi_I^{\text{CG}} \cdot \nabla \psi_J^{\text{CG}} \, dx \quad \text{and} \quad F_0 = [f_I] = \int_D f \psi_I^{\text{CG}} \, dx.$$

Using the operator matrix R_0^T , we may write $A_0(\mu) = R_0 A(\mu) R_0^T$ and $F_0 = R_0 F$, where $A(\mu)$ and F are the standard, fine scale stiffness matrix and forcing vector corresponding to the form in Eq. (IV.7). We also note that the operator matrix may be analogously used in order to project coarse scale solutions onto the fine grid.

IV.3.2.2 Discontinuous Galerkin coupling

One can also use the discontinuous Galerkin (DG) approach (see also [12, 31, 67]) to couple multiscale basis functions. This may avoid the use of the partition of unity functions; however, a global formulation needs to be chosen carefully. Here, we would like to briefly mention a general global coupling that can be used. The global formulation is given by

$$a^{\text{DG}}(u, v; \mu) = f(v) \quad \text{for all} \quad v = \{v_K \in V^K\}, \quad (\text{IV.9})$$

where

$$a^{\text{DG}}(u, v; \mu) = \sum_K a_K^{\text{DG}}(u, v; \mu) \quad \text{and} \quad f(v) = \sum_K \int_K f v_K dx, \quad (\text{IV.10})$$

for all $u = \{u_K\}, v = \{v_K\}$ with K being the coarse element depicted in Figure II.3. Each local bilinear form a_K^{DG} is given as a sum of three bilinear forms:

$$a_K^{\text{DG}}(u, v; \mu) := a_K(u, v; \mu) + r_K(u, v; \mu) + p_K(u, v; \mu), \quad (\text{IV.11})$$

where a_K is the bilinear form,

$$a_K(u, v; \mu) := \int_K \kappa_K(x; \mu) \nabla u_K \cdot \nabla v_K dx, \quad (\text{IV.12})$$

where $\kappa_K(x; \mu)$ is the restriction of $\kappa(x; \mu)$ in K ; r_K is the symmetric bilinear form,

$$r_K(u, v; \mu) := \sum_{E \subset \partial K} \frac{1}{l_E} \int_E \tilde{\kappa}_E(x; \mu) \left(\frac{\partial u_K}{\partial n_K} (v_K - v_{K'}) + \frac{\partial v_K}{\partial n_K} (u_{K'} - u_K) \right) ds,$$

where $\tilde{\kappa}_E(x; \mu)$ is the harmonic average of $\kappa(x; \mu)$ along the edge E , $l_E = 1$ if $E \subset \partial D$, and $l_E = 2$ if $E \subset \mathcal{T}^H \setminus \partial D$. Here, K' and K are two coarse elements sharing the common edge E . Recall that \mathcal{T}^H is the coarse grid mesh. p_K is the penalty bilinear form,

$$p_K(u, v; \mu) := \sum_{E \subset \partial K} \frac{1}{l_E} \frac{1}{h_E} \delta_E \int_E \tilde{\kappa}_E(x; \mu) (u_{K'} - u_K)(v_{K'} - v_K) ds. \quad (\text{IV.13})$$

Here h_E is harmonic average of the length of the edge E and E' , δ_E is a positive penalty parameter that needs to be selected and its choice affects the performance of GMsFEM.

The inherent unconformal property of DG formulation determines the removal of the partition of unity functions while constructing basis functions in Eq. (IV.5). Similarly, we can obtain the discontinuous Galerkin spectral multiscale space as

$$V_{\text{on}}^{\text{DG}}(\mu) = \text{span}\{\psi_k^{K, \text{on}} : 1 \leq k \leq M_{\text{on}}^K, \forall \text{ coarse element } K \subset D\}. \quad (\text{IV.14})$$

Using the same process as in the continuous Galerkin formulation, we can obtain an operator matrix constructed by the basis functions of $V_{\text{on}}^{\text{DG}}(\mu)$. For the consistency of the notation, we denote the matrix as R_0 , and $R_0^T = [\psi_1^{\text{DG}}, \dots, \psi_{N_c}^{\text{DG}}]$. Recall that N_c denote the total number of coarse basis functions.

Solving the problem (IV.1) in the coarse space $V_{\text{on}}^{\text{DG}}(\mu)$ using the DG formulation described in Eq. (IV.9) is equivalent to seeking $u_{\text{ms}}^{\text{DG}}(x; \mu) = \sum_i c_i \psi_i^{\text{DG}}(x; \mu) \in$

$V_{\text{on}}^{\text{DG}}(\mu)$ such that

$$a^{\text{DG}}(u_{\text{ms}}^{\text{DG}}, v; \mu) = f(v) \quad \text{for all } v \in V_{\text{on}}^{\text{DG}}(\mu), \quad (\text{IV.15})$$

where $a^{\text{DG}}(u, v; \mu)$ and $f(v)$ are defined in Eq. (IV.10). Similar as the CG case, we can obtain a coarse linear algebra system

$$A_0 U_0^{\text{DG}} = F_0, \quad (\text{IV.16})$$

where U_0^{DG} denotes the discrete coarse DG solution, and

$$A_0(\mu) = R_0 A(\mu) R_0^T \quad \text{and} \quad F_0 = R_0 F.$$

Here, $A(\mu)$ and F are the standard, fine scale stiffness matrix and forcing vector corresponding to the form in Eq. (IV.10). After solving the coarse system, we can use the operator matrix R_0 to obtain the fine-scale solution in the form of $R_0^T U_0^{\text{DG}}$.

We emphasize that using either GMsFEM formulation offers a computational gain as compared to solving the fine scale problem directly. This is partially due to the fact that the offline stage involves the independent construction of the partition of unity and offline basis functions. In particular, all quantities required of the online computation are pre-computed offline. Furthermore, the size of online system is typically much smaller than the fine scale system, and the online construction only involves a stiffness matrix assembly and local basis computations. An advantage of local approaches in the studied problems is that the solution can be treated as a scalar within each coarse region. In turn, it is cost effective to represent the stiffness matrix via pre-computed matrices. We note that this matrix summation is automatic for the case when the coefficient has a linear representation, however, the discrete

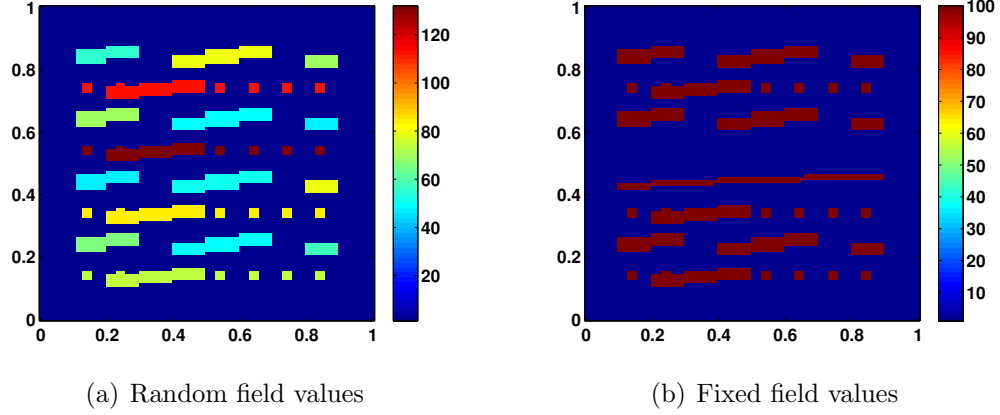


Figure IV.1: High-contrast permeability fields

empirical interpolation method (see, e.g., [21]) allows for a similar (but approximate) representation for more general cases.

IV.4 Numerical Results

In this section we solve the nonlinear elliptic equation given in Eq. (IV.1) using both the continuous (CG) and discontinuous Galerkin (DG) GMsFEM formulations described in Section IV.3. More specifically, we consider the equation

$$-\operatorname{div} \left(e^{\kappa(x)u(x)} \nabla u(x) \right) = f \text{ in } D \quad (\text{IV.17a})$$

$$u = 0 \text{ on } \partial D, \quad (\text{IV.17b})$$

where the general coefficient from (IV.1) is taken to be $\kappa(x; u) = e^{\kappa(x)u(x)}$. For the coefficient $\kappa(x)$, we consider the high-contrast permeability fields as illustrated in Figure IV.1. Figure IV.1(a) represents a field whose high-permeability values are randomly assigned, while the field in Figure IV.1(b) has a different channelized structure with fixed maximum values. We use a source term $f = 0.1$, and solve the problem on the unit two-dimensional domain $D = [0, 1] \times [0, 1]$.

To solve Eq. (IV.17) we first linearize it by using a Picard iteration. In particular, for a given initial guess u^0 we solve

$$-\operatorname{div} (e^{\kappa(x)u^n(x)} \nabla u^{n+1}(x)) = f \text{ in } D \quad (\text{IV.18a})$$

$$u^{n+1} = 0 \text{ on } \partial D, \quad (\text{IV.18b})$$

for $n \geq 0$.

In our simulations, we take the initial guess $u^0 = 0$, and terminate the iterative loop when $\|A(u^{n+1})u^{n+1} - b\| \leq \delta \|b\|$, where δ is the tolerance for the iteration and we select $\delta = 10^{-3}$. We note that A and b correspond to the linear system resulting from either the CG or DG global formulations. In particular, we solve the problem as follows,

$$A(u^n)u^{n+1} = b \text{ for } n = 0, 1, \dots \quad (\text{IV.19})$$

We note that since u^n and u^{n+1} will not necessarily be computed in coarse spaces of the same dimension, we cannot directly use the residual criterion listed above. Actually, we use the Galerkin projection of the fine solution to the corresponding coarse space to calculate the residual error from above. For all cases presented in this section, the global iteration resulting from the linearization converges in 4 or 5 iterations.

Remark IV.4.1. *In this section we will consider two types of coefficients $\kappa(x)$ to be used in Eq. (IV.17). We recall that throughout this chapter we have used an auxiliary variable $\mu = \bar{u}^n$ to denote the solution dependence of the nonlinear problem. As such, we have referred to the model equation as parameter-dependent while describing the iterative solution procedure. Consequently, we are careful to introduce (and*

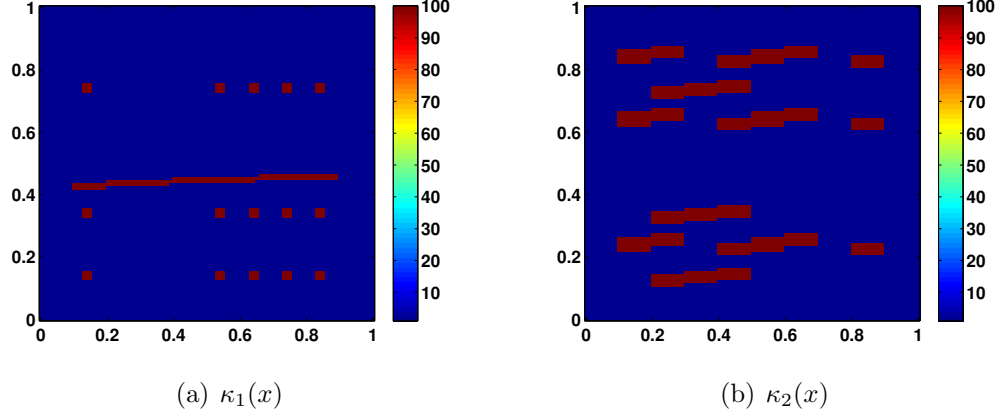


Figure IV.2: Decomposition of permeability field IV.1(b)

distinguish) a related case where we use a “physical” parameter μ^p for the purpose of constructing a field of the form $\kappa(x) = \mu^p \kappa_1(x) + (1 - \mu^p) \kappa_2(x)$. See Figure IV.2 for an illustration of $\kappa_1(x)$ and $\kappa_2(x)$. We note that the coefficient will be constructed by summing contributions that depend on the physical parameter μ^p , in addition to the auxiliary parameter dependence from the iterative form. In SubSection IV.4.1 we use a field that does not depend on μ^p , and in SubSection IV.4.2 we use a field that does depend on μ^p .

IV.4.1 Parameter-independent permeability field

In the following simulations we first generate a snapshot space, use a spectral decomposition to obtain the offline space, and then for an initial guess apply a similar spectral decomposition to obtain the online space. We recall that in order to construct the snapshot space we choose a specified number of eigenfunctions (denoted by M_{snap}) on either a coarse neighborhood or coarse element depending on whether we use continuous (CG) or discontinuous Galerkin (DG) global coupling, respectively. In our simulations, we select the range of solutions $[u_{\min}, u_{\max}]$ that correspond to

solving the fine scale equation using a source term that ranges from $f \in [0.1, 1]$. For the first set of simulations we divide the domain $[u_{\min}, u_{\max}]$ into $N_s - 1$ equally spaced subdomains to obtain N_s discrete points u_1, \dots, u_{N_s} . For these simulations we fix a value of $N_s = 9$.

For either formulation, we solve a localized eigenvalue problem as defined in SubSection IV.3.1 for each point u_j on a coarse neighborhood and keep a specified number of eigenfunctions. For example, in the CG case we keep $l_{\max} = 3$ snapshot eigenfunctions, and this construction leads to a local space of dimension $M_{\text{snap}} = l_{\max} \times N_s = 3 \times 9 = 27$. In the DG case, we adaptively choose the number of eigenfunctions based on a consideration of the eigenvalue differences. In the offline space construction we fix \bar{u} as the average of the previously defined fixed snapshot values. We then solve the offline eigenvalue problem and construct the offline space by keeping the eigenvectors corresponding to a specified number of dominant eigenvalues. At the online stage we use the initial guess $u^0 = 0$ in order to solve the respective eigenvalue problem required for the space construction. We note that the size of our online space and the associated solution accuracy will depend on the number of eigenvectors that we keep in the online space construction.

In the CG formulation, we recall that the online eigenfunctions are multiplied by the corresponding partition of unity functions with support in the same neighborhood of the respective coarse node. We then solve Eq. (IV.17) iteratively within the online space. In particular, for each iteration we update the online space and solve Eq. (IV.17) using the previously computed solution.

In the simulations using the CG formulation, we discretize our domain into coarse elements of size $H = 1/10$, and fine elements of size $h = 1/100$. The results corresponding to the permeability fields from Figures IV.1(a) and IV.1(b) are shown in Tables IV.1 and IV.2, respectively. The first column shows the dimension of the

online solution space, and the second column shows the eigenvalue λ^* which corresponds to the first eigenfunction that is discarded from space enrichment. We note that this eigenvalue is an important consideration in error estimates of enriched multiscale spaces ([42]). As a formal consideration, we mention that the error analysis typically yields estimates of the form $\|u - u_{\text{ms}}\| \sim \mathcal{O}(H^\gamma \lambda^*)$ when the dominant eigenvalues are taken to be small. The next two columns correspond to the L^2 -weighted relative error $\|u - u_{\text{ms}}\|_{L_\kappa^2(D)} / \|u\|_{L_\kappa^2(D)} \times 100\%$ and energy relative error $\|u - u_{\text{ms}}\|_{H_\kappa^1(D)} / \|u\|_{H_\kappa^1(D)} \times 100\%$ between the GMsFEM solution u_{ms} and the fine-scale solution u . We note that as the dimension of the online space increases (i.e., we keep more eigenfunctions in the space construction), the relative errors decrease accordingly. As an example, for the field in Figure IV.1(a), we encounter L^2 relative errors that decrease from 1.43 – 0.24%, and energy relative errors that decrease from 16.12 – 6.85% as the online space is systematically enriched. In the tables, analogous errors between the online GMsFEM solution and the offline solution are computed. The dimension of the offline space is taken to be the maximum dimension of the online space. We note that in this case the Picard iteration converges in 4 steps for all simulations. In Figure IV.3 we also plot the fine and coarse-scale CG solutions that correspond to the field in Figure IV.1(b). We note that the fine solution, and the coarse solutions corresponding to the largest and smallest online spaces are nearly indistinguishable.

We also illustrate the relation between the online-offline energy errors and λ^* in Figure IV.4 for the same permeability fields considered above. From the plots in Figure IV.4, we see that the energy error predictably decreases as λ^* decreases, thus following the appropriate error behavior.

In order to solve the model problem using the DG formulation, we note that the space of snapshots is constructed in a slightly different fashion. In this case, the se-

$\dim(V_{\text{on}}^{\text{CG}})$	λ^*	GMsFEM Relative Error (%)		Online-Offline Relative Error (%)	
		$L_{\kappa}^2(D)$	$H_{\kappa}^1(D)$	$L_{\kappa}^2(D)$	$H_{\kappa}^1(D)$
319	0.0021	1.43	16.12	1.25	16.33
497	0.0010	0.69	11.71	0.48	10.66
770	3.36×10^{-4}	0.40	9.13	0.20	7.30
1043	1.06×10^{-4}	0.31	7.76	0.09	4.43
1270	—	0.24	6.85	0.00	0.00

Table IV.1: CG relative errors corresponding to the permeability field in Figure IV.1(a)

$\dim(V_{\text{on}}^{\text{CG}})$	λ^*	GMsFEM Relative Error (%)		Online-Offline Relative Error (%)	
		$L_{\kappa}^2(D)$	$H_{\kappa}^1(D)$	$L_{\kappa}^2(D)$	$H_{\kappa}^1(D)$
316	0.0026	1.36	15.28	1.18	15.74
482	0.0010	0.71	11.89	0.51	11.17
722	3.18×10^{-4}	0.43	9.53	0.22	7.77
996	1.02×10^{-4}	0.33	8.02	0.11	4.72
1236	—	0.26	7.05	0.00	0.00

Table IV.2: CG relative errors corresponding to the permeability field in Figure IV.1(b)

lection of eigenvectors hinges on a comparison between the difference of consecutive eigenvalues resulting from the localized computations. In contrast to the CG case, the initial number of eigenfunctions (call this number l_{init}^K) used in the snapshot space construction are adaptively chosen based on the relative size of consecutive eigenvalues. We note that either way for choosing eigenfunctions is relevant for both global formulations, and both constructions yield a predictable snapshot space dimension. For the results corresponding to the DG formulation, we note that two configurations for the snapshot space construction are used. In particular, we consider a case when the original number of eigenfunctions l_{init}^K are used in the construction, and a case

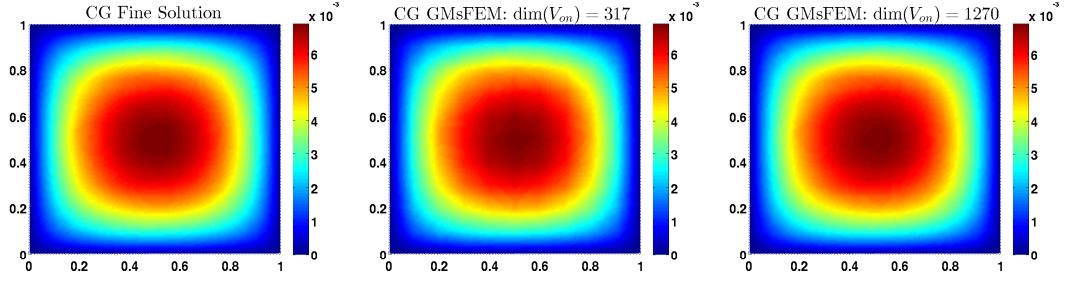


Figure IV.3: Comparison of fine and coarse CG solutions corresponding to Figure IV.1(b)

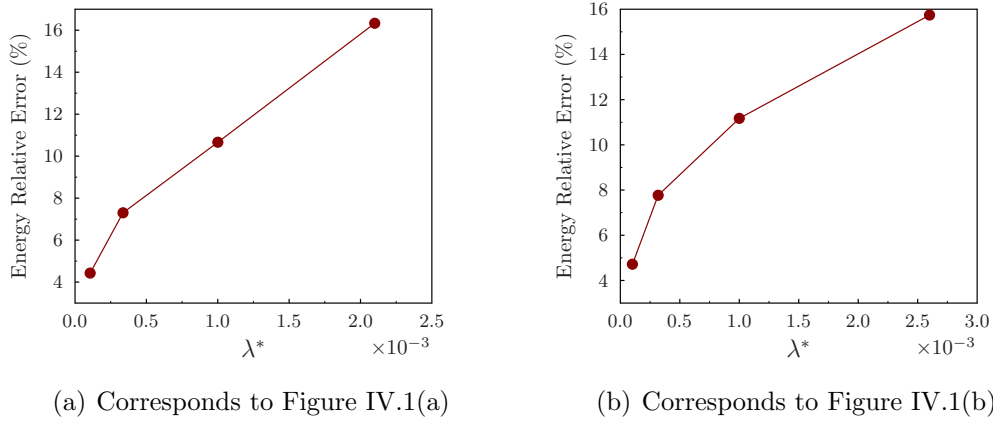


Figure IV.4: Relation between the first discarded eigenvalue and the CG relative energy error; permeability from Figure IV.1(a) (left), permeability from Figure IV.1(b) (right)

when $l_{\max}^K = l_{\text{init}}^K + 3$ are used in the construction.

In the simulations using the DG formulation, we partition the original domain using a coarse mesh of size $H = 1/10$, and use a fine mesh composed of uniform triangular elements of mesh size $h = 1/100$. The numerical results for permeability fields IV.1(a) and IV.1(b) are represented in Tables IV.3 and IV.4, respectively. The first column shows the dimension of the online space, the second column represents

the corresponding eigenvalue (λ^*) of the first eigenfunction discarded from the online space, and the next two columns illustrate the interior energy relative error (E_{int}) and the boundary energy relative error (E_{∂}) between the fine scale solution and DG GMsFEM solution. We follow the definition of E_{int} and E_{∂} as in [37] and using the notation introduced in SubSection IV.3.2.2,

$$T = \sum_{K \subset D} \left\| \kappa_K^{\frac{1}{2}}(x; u) \nabla u \right\|_{L^2(K)}^2 + \sum_{K \subset D} \sum_{E \subset \partial K} \frac{1}{l_E} \frac{1}{h_E} \int_E \tilde{\kappa}_E(x; u) (u_K - u_{K'})^2 ds,$$

$$E_{\text{int}} = \left(\sum_{K \subset D} \left\| \kappa_K^{\frac{1}{2}}(x; u) \nabla e \right\|_{L^2(K)}^2 / T \right)^{\frac{1}{2}}, \quad (\text{IV.20})$$

$$E_{\partial} = \left(\sum_{K \subset D} \sum_{E \subset \partial K} \frac{1}{l_E} \frac{1}{h_E} \int_E \tilde{\kappa}_E(x; u) (e_K - e_{K'})^2 ds / T \right)^{\frac{1}{2}}. \quad (\text{IV.21})$$

Here, $e = u - u_{ms}$.

The errors between the offline and online solutions are offered in the final two columns. We note that as the dimension of the online space increases (i.e., we keep more eigenfunctions in the space construction), the relative errors decrease accordingly. For example, the DG solution corresponding to Figure IV.1(a) yields interior relative energy errors that decrease from 55.08 – 34.86%, and boundary relative energy errors that decrease from 8.94 – 6.40%. We note that in this case the Picard iteration converges in 4 or 5 steps for all simulations. In Figure IV.5 we also plot the fine and coarse DG solutions that correspond to the field in Figure IV.1(b). We note that the fine solution and the coarse solution corresponding to the smallest online space show some slight differences. However, the discrepancies noticeably diminish when the coarse DG solution is computed within the largest online space.

As in the CG case, we also illustrate the relation between the DG online-offline interior errors and λ^* in Figure IV.6. From the plots in Figure IV.6, we see that the

$\dim(V_{\text{on}}^{\text{DG}})$	λ^*	GMsFEM Relative Error (%)		Online-Offline Relative Error (%)	
		E_{int}	E_{∂}	E_{int}	E_{∂}
271	1.53×10^{-4}	55.08	8.94	44.38	8.43
331	1.24×10^{-4}	36.59	6.63	10.05	3.08
466	3.03×10^{-5}	35.57	6.56	7.00	1.67
624	1.72×10^{-5}	34.90	6.48	2.12	0.40
716	—	34.86	6.40	0.00	0.00

Table IV.3: DG relative errors corresponding to the permeability field in Figure IV.1(a); snapshot space uses l_{init}^K eigenfunctions

$\dim(V_{\text{on}}^{\text{DG}})$	λ^*	GMsFEM Relative Error (%)		Online-Offline Relative Error (%)	
		E_{int}	E_{∂}	E_{int}	E_{∂}
270	1.56×10^{-4}	56.29	10.30	46.37	9.75
331	1.05×10^{-4}	36.72	6.71	9.54	3.32
444	3.12×10^{-5}	35.67	6.56	6.48	1.67
582	1.21×10^{-5}	35.06	6.48	2.14	0.41
663	—	35.03	6.48	0.00	0.00

Table IV.4: DG relative errors corresponding to the permeability field in Figure IV.1(b); snapshot space uses l_{init}^K eigenfunctions

relative errors decrease as λ^* decreases. However, we elaborate on two distinctions between these results and the CG results. In particular, we first note that the snapshot error for the DG solutions is roughly 35% (recall Tables IV.3 and IV.4). Thus, we accept this residual error and use the online-offline error as a measure of convergence. In addition, we omit the error quantity that corresponds to the lowest dimensional online space for the plots in Figure IV.6. In this case, the smallest space does not offer an adequate representation of the solution because of the dominant penalty.

Remark IV.4.2. *When solving the nonlinear equation using the discontinuous Galerkin*

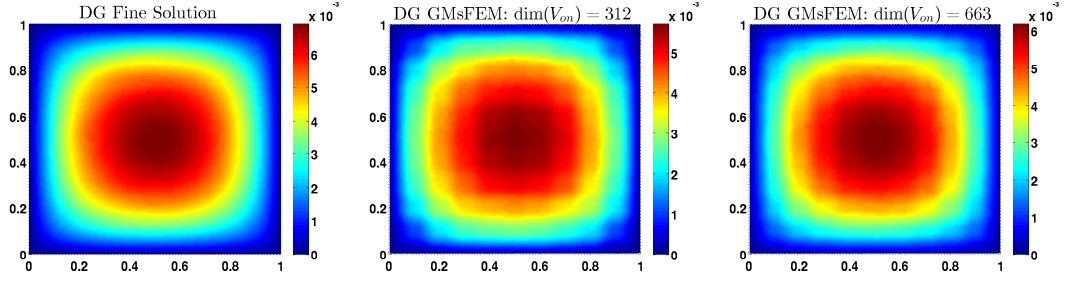


Figure IV.5: Comparison of fine and coarse DG solutions corresponding to Figure IV.1(b)

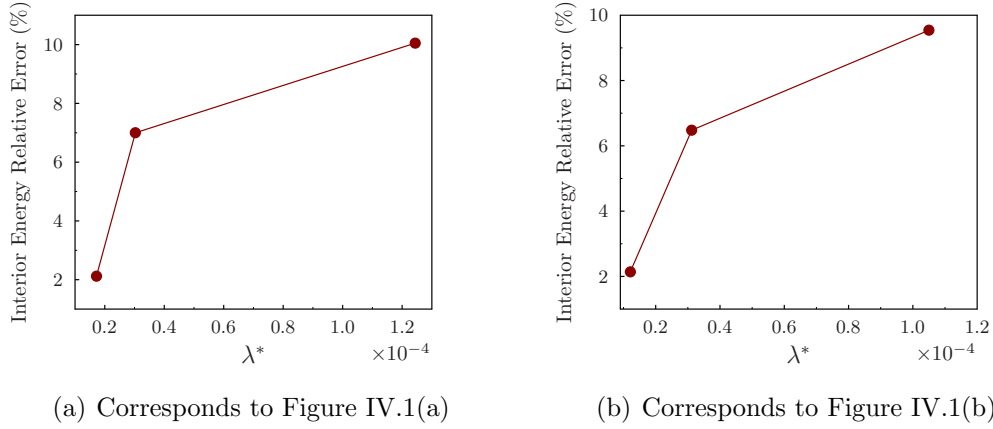


Figure IV.6: Relation between the first discarded eigenvalue and the DG relative interior energy error; permeability from Figure IV.1(a) (left), permeability from Figure IV.1(b) (right) IV.1(a) and IV.1(b)

approach, we use different penalty parameters for fine-grid problem and coarse-grid problem (refer back to SubSection IV.3.2.2). However, we observe that for different coarse penalty parameters that yield a convergent solution, the number of iterations and the relative errors (both interior and boundary) stay the same.

Remark IV.4.3. *Recall that we use the Galerkin projection of the previous coarse solution onto the current online space as the approximation of the previous coarse*

$\dim(V_{\text{on}}^{\text{DG}})$	λ^*	GMsFEM Relative Error (%)		Online-Offline Relative Error (%)	
		E_{int}	E_{∂}	E_{int}	E_{∂}
381	1.47×10^{-4}	37.34	7.42	22.80	6.00
440	1.54×10^{-4}	35.92	6.16	20.07	4.36
707	9.54×10^{-5}	32.80	5.29	13.64	2.90
958	2.71×10^{-5}	29.44	5.48	4.80	0.98
1352	—	28.98	5.39	0.00	0.00

Table IV.5: DG relative errors corresponding to the permeability field in Figure IV.1(b); snapshot space uses $l_{\text{max}}^K = l_{\text{init}}^K + 3$ eigenfunctions

solution to obtain the terminal condition. If the coarse penalty parameter is changed, we should use the current coarse penalty parameter to construct the Galerkin projection.

We observe from Tables IV.1-IV.4 that the offline spaces for DG formulation are much smaller than those obtained through CG formulation. As a result, in Table IV.5 we use more eigenfunctions (more specifically, we set $l_{\text{max}}^K = l_{\text{init}}^K + 3$) in the snapshot space construction to yield a larger offline space. For these examples, we use the permeability field from Figure IV.1(b). Due to the increase of the offline (and corresponding online) space dimensions, we see more accurate results than those offered in Table IV.4.

IV.4.2 Parameter-dependent permeability field

For the next set of numerical results, we consider solving the nonlinear elliptic problem in Eq. (IV.17) with a coefficient of the form

$$\kappa(x, u, \mu^p) = \exp [(\mu^p \kappa_1(x) + (1 - \mu^p) \kappa_2(x)) u(x)].$$

For $\kappa_1(x)$ and $\kappa_2(x)$ we use the fields shown in Figure IV.2(a) and IV.2(b), respectively.

As for the parameter-dependent simulation, we are careful to distinguish the difference between the auxiliary parameter $\mu = \bar{u}^n$ which is used to denote a previous solution iterate, and a “physical” parameter μ^p that is used in the construction of a new permeability field. We take the range of μ^p to be $[0, 1]$, and use three equally spaced values in order to construct the snapshot space in this case. We use the same $[u_{\min}, u_{\max}]$ interval from the previous results, yet use four equally spaced values in this case. In particular, we use the pairs (u_j, μ_l^p) , where $1 \leq j \leq 4$, and $1 \leq l \leq 3$ as the fixed parameter values for the snapshot space construction. At the online stage we use the initial guess $u^0 = 0$ and a fixed value of $\mu^p = 0.2$ while solving the respective eigenvalue problem required for the continuous or discontinuous Galerkin online space construction.

In Table IV.6 we offer results corresponding to the CG formulation, and in Tables IV.7 and IV.8 we offer results corresponding to the DG formulation. In all cases we encounter very similar error behavior compared to the examples offered earlier in the section. In particular, an increase of the dimension of the online space yields predictably smaller errors, and smaller values of λ^* correspond to the error decrease. And while it suffices to refer back to related discussions earlier in the section, we emphasize that this distinct set of results serves to further illustrate the robustness of the proposed method. In particular, we show that the solution procedure allows for a suitable treatment of nonlinear problems that involve auxiliary parameters that are used to represent the nearly constant solution behavior on a coarse subregion, and physical parameters that are explicitly used in the permeability field construction.

$\dim(V_{\text{on}}^{\text{CG}})$	λ^*	GMsFEM Relative Error (%)		Online-Offline Relative Error (%)	
		$L_{\kappa}^2(D)$	$H_{\kappa}^1(D)$	$L_{\kappa}^2(D)$	$H_{\kappa}^1(D)$
309	0.0027	1.30	14.89	1.10	15.32
492	0.0010	0.59	10.82	0.39	9.76
580	6.76×10^{-4}	0.45	9.55	0.24	7.92
728	3.33×10^{-4}	0.34	7.87	0.12	5.23
991	—	0.28	6.74	0.00	0.00

Table IV.6: CG relative errors corresponding to the parameter-dependent field constructed from Figure IV.2(a) and IV.2(b)

$\dim(V_{\text{on}}^{\text{DG}})$	λ^*	GMsFEM Relative Error (%)		Online-Offline Relative Error (%)	
		E_{int}	E_{∂}	E_{int}	E_{∂}
300	1.02×10^{-4}	37.56	7.94	10.15	3.16
313	6.25×10^{-5}	37.55	7.81	10.00	2.85
403	2.58×10^{-5}	36.81	7.35	5.83	1.38
497	1.22×10^{-5}	36.37	7.21	0.84	0.10
517	—	36.36	7.21	0.00	0.00

Table IV.7: DG relative errors corresponding to the parameter-dependent field constructed from Figure IV.2(a) and IV.2(b); snapshot space uses l_{init}^K eigenfunctions

IV.5 Concluding remarks

In this chapter, we implement the Generalized Multiscale Finite Element (GMsFEM) framework to nonlinear elliptic equations in high-contrast heterogeneous media. In order to solve this type of problem we linearize the equation such that upscaled quantities of previous solution iterates can be regarded as auxiliary coefficient parameters in the problem formulation. As a result, we are able to construct a respective set of coarse basis functions using an offline-online procedure in which the precomputed offline space allows for the efficient computation of a smaller-dimensional online space for any parameter value at each iteration.

$\dim(V_{\text{on}}^{\text{DG}})$	λ^*	GMsFEM Relative Error (%)		Online-Offline Relative Error (%)	
		E_{int}	E_{∂}	E_{int}	E_{∂}
300	2.13×10^{-4}	37.59	7.94	22.54	6.40
440	1.54×10^{-5}	35.78	5.92	18.89	3.74
668	7.69×10^{-5}	32.54	5.39	11.62	2.58
902	1.51×10^{-5}	30.23	5.29	3.87	1.06
1093	—	29.88	5.29	0.00	0.00

Table IV.8: DG relative errors corresponding to the parameter-dependent field constructed from Figure IV.2(a) and IV.2(b); snapshot space uses $l_{\text{max}}^K = l_{\text{init}}^K + 3$ eigenfunctions

The coarse space construction involves solving a set of localized eigenvalue problems that are tailored to either continuous Galerkin (CG) or discontinuous Galerkin (DG) global coupling mechanisms. In particular, the respective coarse spaces are formed by keeping a set of eigenfunctions that correspond to the localized eigenvalue behavior. Using either formulation, we show that the process of systematically enriching the coarse solution spaces yields a predictable error decline between the fine and coarse-grid solutions. As a result, the proposed methodology is shown to be an effective and flexible approach for solving the nonlinear, high-contrast elliptic equation that we consider in this chapter.

Similar to the reduced basis (RB) method, the main computation lies in the calculations of the offline space. The latter depends on the choice of representative solutions to generate each local snapshot space. It is of great interest and importance if we can get a series of representative solutions with minimal efforts. There are several strategies, e.g., greedy sampling algorithm, for this type of problems. Further, we can replace the Picard iteration method with Newton’s method for a faster convergence rate. Adaptive enrichment algorithm presented in Chapter III can be extended to nonlinear elliptic problems for a smaller online space.

V. GENERALIZED MULTISCALE FINITE ELEMENT METHODS. BRINKMAN FLOW

V.1 Introduction

In this chapter, we investigate Brinkman flow in high-contrast heterogeneous permeability fields as analyzed in [46].

The Brinkman model can be written as

$$\begin{aligned}\nabla p - \mu \Delta u + \kappa^{-1} u &= f && \text{in } D, \\ \operatorname{div} u &= 0 && \text{in } D,\end{aligned}\tag{V.1}$$

where p is the fluid pressure and u represents the velocity. Here, μ is the viscosity and $\kappa = \kappa(x)$ is a heterogeneous multiscale coefficient that models the permeability of the porous medium.

We assume that the variations of κ occur within a very fine scale and therefore a direct simulation of this model is costly. As mentioned in Chapter I, one of the main advantages of the Brinkman model is that it can capture Stokes and Darcy type flow behavior depending on the value of κ without the usage of a complex interface condition as needed in the Stokes-Darcy interface model. This is very convenient when modeling complicated porous scenarios such as a vuggy medium. However, this advantage of the Brinkman model does not come for free: it brings the challenge of effectively designing numerical homogenization or upscaling methodologies since the resulting upscaling method must capture the correct flow behavior in corresponding regions. This difficulty increases in the case of high-contrast media due to the fact that, in a single coarse region, the permeability field can have variations of several orders of magnitude that make it difficult to compute effective coefficient or boundary

conditions using classical multiscale finite element methods.

We present several numerical examples to illustrate the performance of the proposed approach. In particular, four different high-contrast multiscale permeability fields, which are representative of Brinkman flow scenarios: a fast Darcy flow going through the slower region; a slower Darcy flow past Darcy flow regions; a free flow going across the Darcy flow region; and a Darcy flow passing the strong free flow region. All the numerical results indicate that the proposed GMsFEM is robust and accurate.

The rest of this chapter is organized as follows. In Section V.2, we present preliminaries on the Brinkman model and the GMsFEM. The construction of the coarse spaces for the GMsFEM is displayed in Section V.3. In Section V.4, numerical results for several representative examples are showed. The proofs of our main results, including stability and a priori error estimates, are exhibited in Section V.5. At last, we end this chapter with a conclusion in Section V.6.

V.2 Preliminaries

Let D be a polygonal domain in \mathbb{R}^d ($d = 2, 3$) with a boundary ∂D in the Brinkman problem (V.1). Here the source term $f \in (L^2(D))^d$, the boundary condition $g \in (H^{\frac{1}{2}}(\partial D))^d$, and κ^{-1} is a positive definite heterogeneous tensor field with high-contrast. Without loss of generality, we assume the viscosity parameter $\mu = 1$ and $g = 0$ throughout.

To simplify the notation, we denote by $V(D) = (H_0^1(D))^d$ and $W(D) = L_0^2(D)$. The variational formulation of the problem is given by: find $u \in V(D)$ and $p \in W(D)$

such that

$$\begin{aligned} a(u, v) + b(v, p) &= l_f(v) & \text{for all } v \in V(D), \\ b(u, q) &= 0 & \text{for all } q \in W(D), \end{aligned}$$

where the bilinear forms $a(\cdot, \cdot)$ and $b(\cdot, \cdot)$ are respectively defined by

$$\begin{aligned} a(u, v) &= \langle \nabla u, \nabla v \rangle_D + \langle \kappa^{-1} u, v \rangle_D, & \text{for all } u, v \in V(D), \\ b(u, p) &= \langle \operatorname{div} u, p \rangle_D, & \text{for all } u \in V(D), p \in W(D), \end{aligned}$$

and the linear form l_f is given by

$$l_f(v) = \langle f, v \rangle_D, \text{ for all } v \in V(D),$$

where $\langle \cdot, \cdot \rangle_D$ denotes the L^2 inner product over D .

Let \mathcal{T}_H be a coarse-grid partition of the domain D and \mathcal{T}_h be a conforming fine triangulation of D . We assume that \mathcal{T}_h is a refinement of \mathcal{T}_H , where h and H represent the mesh size of a fine and coarse cell, respectively. Typically we assume that $0 < h \ll H < 1$, and that the triangulation \mathcal{T}_h is fine enough to fully resolve the spatial variations of the coefficient κ , while H is too coarse to accurately resolve this spatial variations inside a coarse element, and the coefficient κ may have large variations within the coarse block. On the triangulation \mathcal{T}_h , we introduce the following finite element spaces

$$\begin{aligned} V_h &:= \{v \in V(D) | v|_K \in (P^2(K))^d \text{ for all } K \in \mathcal{T}_h\}, \\ W_h &:= \{q \in W(D) | q|_K \in P^0(K), \text{ for all } K \in \mathcal{T}_h\}. \end{aligned}$$

The standard mixed finite element method for problem (V.1) is to seek an approximation (u_h, p_h) in the finite element space $V_h \times W_h \subset V(D) \times W(D)$ such that

$$\begin{aligned} a(u_h, v) + b(v, p_h) &= l_f(v) & \text{for all } v \in V_h, \\ b(q, u_h) &= 0 & \text{for all } q \in W_h, \end{aligned}$$

or which is equivalent to the solution of the following linear system

$$\begin{pmatrix} A & B \\ B^T & 0 \end{pmatrix} \begin{pmatrix} u \\ p \end{pmatrix} = \begin{pmatrix} F \\ 0 \end{pmatrix}.$$

Here the matrices denote

$$v^T A u = a(u, v), \quad \text{for all } u, v \in V_h, \tag{V.2}$$

$$q^T B u = b(u, q), \quad \text{for all } u \in V_h \text{ and } q \in W_h. \tag{V.3}$$

Note that here and below, in order to simplify notation, we are using the same notation for finite element functions and their corresponding vector representations.

It is well known the mixed finite element formulation described above is stable; see for instance [73]. In the case of high-contrast media, a very refined grid is needed in order to fully resolve small scale features, and thus it is prohibitively expensive to solve the resulting system. Meanwhile, if we naively apply P^2/P^0 finite element spaces over the coarse mesh \mathcal{T}_H , the resulting system is small but obviously the solution can only represent a poor approximation to the exact solution. To turn around the dilemma, we follow the GMsFEM framework proposed in [36].

In the GMsFEM methodology, one divides the computations into onffline and

online computations. The offline computations are based upon a preliminary dimension reduction of the fine-scale finite element spaces (that may include dealing with additionally important physical parameters, uncertainties and nonlinearities), and then the online procedure (if needed) is applied to construct a reduced order model on the offline space. We start by constructing offline spaces.

We construct the coarse function space

$$V^{\text{off}} := \text{span}\{\phi_i\}_{i=1}^{N_c},$$

where N_c is the number of coarse basis functions. Each ϕ_i is supported in some coarse neighborhood w . For the pressure field p , we use the space of piecewise constant functions over the coarse triangulation \mathcal{T}_H , that is,

$$W^{\text{off}} := \{q \in L_0^2(D) | q|_K \in P^0(K), \text{ for all } K \in \mathcal{T}_H\}. \quad (\text{V.4})$$

We denote $N_H = \dim W^{\text{off}}$.

The idea is then to work on the reduced spaces $V^{\text{off}} \times W^{\text{off}}$ instead of the original spaces $V(D) \times W(D)$. In the general GMsFEM methodology, these offline spaces are used in the online computations where a further reduction may be performed; see [42, 36] for details. The overall performance of the resulting GMsFEM depends on the approximation properties of the resulting offline and online coarse spaces. In this chapter, we focus on the construction of the offline spaces only. We mention that this is sufficient for the effective numerical upscaling of the Brinkman model proposed above where neither parameters nor nonlinearities are considered. The more general case with additional parameters can also be studied using the proposed method, but it requires online dimension reduction ([42, 36, 41]) and thus defer to a future study.

The GMsFEM seeks an approximation $(u_0, p_0) \in V^{\text{off}} \times W^{\text{off}}$ which satisfies the coarse scale offline formulation,

$$a(u_0, v) + b^t(p_0, v) = l_f(v) \quad \text{for all } v \in V^{\text{off}}, \quad (\text{V.5a})$$

$$b(u_0, q) = 0 \quad \text{for all } q \in W^{\text{off}}. \quad (\text{V.5b})$$

We can interpret the method in the following way using matrix representations. Recall that both coarse basis functions $\{\phi_i\}_{i=1}^{N_c}$ and $\{q_i\}_{i=1}^{N_H}$ are defined on the fine grid, and can be represented by the fine grid basis functions. Specifically, we introduce the following matrices,

$$R_0^T = [\phi_1, \dots, \phi_{N_c}] \quad \text{and} \quad Q_0^T = [q_1, \dots, q_{N_H}],$$

where we identify the basis ϕ_i and q_i with their coefficient vectors in the fine grid basis. Then the matrix analogue of the system (V.5) can be equivalently written as

$$\begin{pmatrix} R_0 A R_0^T & R_0 B Q_0^T \\ Q_0 B^T R_0^T & 0 \end{pmatrix} \begin{pmatrix} u_0 \\ p_0 \end{pmatrix} = \begin{pmatrix} R_0 F \\ 0 \end{pmatrix}. \quad (\text{V.6})$$

Further, once we solve the coarse system (V.6), we can recover the fine scale solution by $R_0^T u_0$ and $Q_0^T p_0$. In other words, R_0^T and Q_0^T can be regarded as the transformation (also known as interpolation, extension, and downscaling) matrix from the space V^{off} to the space V_h and W^{off} to the space W_h .

The accuracy of the GMsFEM relies crucially on the coarse basis functions $\{\phi_i\}$. We shall present one novel construction of suitable basis functions for the Brinkman equation in Section V.3.

V.3 The construction of the space V^{off}

In this section, we present the construction of the space V^{off} in detail. For the pressure field p , we simply use piecewise constant functions over the coarse grid as defined in (V.4). Therefore the focus below is on the construction of the offline velocity space V^{off} . To this end, we first introduce the concept of (harmonic) extension of boundary data in the Brinkman sense, which will play an important role in the construction. The precise definition is given below.

Definition V.3.1 (Brinkman Extension). *For a domain $K \subset \mathbb{R}^d$, we define the Brinkman extension of any $v \in (H^{\frac{1}{2}}(\partial K))^d$, denoted by $\mathcal{H}(v) \in (H^1(K))^d$, to be the unique solution of the following homogeneous Brinkman equation (with $|K|$ being the measure of K)*

$$\begin{aligned} \nabla p - \mu \Delta \mathcal{H}(v) + \kappa^{-1} \mathcal{H}(v) &= 0 && \text{in } K, \\ \text{div } \mathcal{H}(v) &= \frac{1}{|D|} \int_{\partial D} v \cdot n && \text{in } K, \\ \mathcal{H}(v) &= v && \text{on } \partial K. \end{aligned}$$

Remark V.3.2. *In practice, the extension $\mathcal{H}(v)$ is the numerical solution of the equation in the fine-scale finite element space $V_h(K) \times W_h(K)$, where K is a coarse block (see Figure (V.1) for an illustration of coarse block and coarse neighborhood). This computation can be efficiently performed due to the moderated size of the coarse regions. Besides, the computations can be carried out in parallel, if the computations are required over all coarse regions.*

Now we are ready to state the detailed construction of the offline velocity space V^{off} . Our construction consists of the following three steps. We defer the analysis of the resulting GMsFEM method to Section V.5.

V.3.0.0.1 Building multiscale partition of unity functions. First we introduce a set of generalized global partition of unity functions on the coarse grid. We denote the set of all coarse edges by \mathcal{E}_H , and consider the following finite element space:

$$M_H := \{v \in C^0(\mathcal{E}_H) : v|_F \in P^2(F), \quad \text{for all } F \in \mathcal{E}_H\}.$$

Let \mathcal{P}_H be the set of the shape functions of the space M_H . Then \mathcal{P}_H also forms a set of partition of unity functions over the skeleton \mathcal{E}_H .

Next we introduce the set of multcale partition of unity functions for a two-dimensional domain ω . We remark that the construction for the three-dimensional case is similar. For any $\chi \in \mathcal{P}_H$, let ω denote the support of χ , and we call ω a coarse neighborhood associated with χ . In Figure V.1, we sketch all three possible types of the coarse neighborhood, ω_1 , ω_2 and ω_3 , respectively. ω_1 corresponds to partition of unity function χ having nodal value 1 at the coarse node i ; ω_2 represents the support of χ valuing 1 at node j , and ω_3 stands for support of χ equaling to 1 at node k .

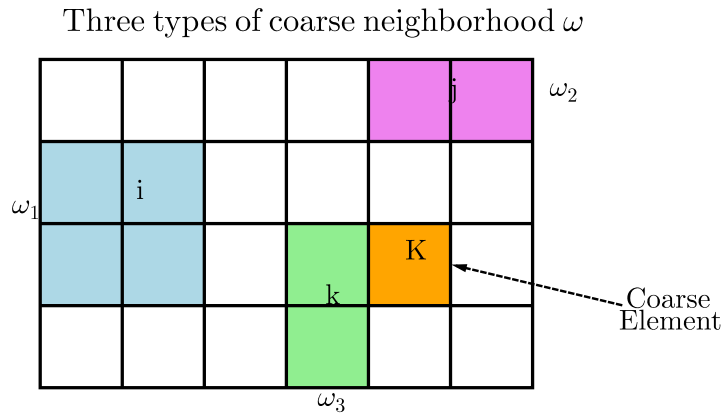


Figure V.1: Illustration of three types of coarse neighborhoods and coarse element: ω_1 , ω_2 and ω_3 denote the support of partition of unity functions χ .

For each $\chi \in \mathcal{P}_H$, we have two Brinkman extensions of χ : $\mathcal{H}(\chi^x)$ and $\mathcal{H}(\chi^y)$. Here $\mathcal{H}(\chi^x)$ is the Brinkman extension of the Dirichlet data $\chi^x = (\chi, 0)$, and it is defined on each coarse block $K \subset \omega$. The extension $\mathcal{H}(\chi^y)$ is defined similarly, with $\chi^y = (0, \chi)$. We note that these vector functions can be extended by 0 to the entire domain D , since χ vanishes over $\partial\omega$. Finally, the generated partition of unity functions associated with χ is $\chi_x = \frac{1}{2}(\mathcal{H}(\chi^x))_x$, $\chi_y = \frac{1}{2}(\mathcal{H}(\chi^y))_y$, where $(\cdot)_x$ and $(\cdot)_y$ denote the first component and second component of a vector, respectively. Thus, for each $\chi \in \mathcal{P}_H$, we generate two partition of unity functions supported on ω . All these extensions together form a set of multiscale partition of unity functions, which are denoted by:

$$\mathcal{P}_{\text{ext}} = \{\chi_i\}_{i=1}^{N_p},$$

where N_p is the number of multiscale partition of unity functions. We note that the set \mathcal{P}_{ext} does not have the default property of partition of unity over the domain D , but only over the skeleton \mathcal{E}_H , i.e.,

$$\sum_{i=1}^{N_p} \chi_i \equiv 1 \quad \text{on } \mathcal{E}_H. \quad (\text{V.7})$$

V.3.0.0.2 Constructing local snapshot space V_{snap}^ω . In this step, we construct the local snapshot spaces. Proceeding as before, for each $\chi \in \mathcal{P}_{\text{ext}}$, we let ω denote its support set, and call it the coarse neighborhood associated with χ , which consists of either two or four coarse blocks, cf. Figure II.3. The construction of the local snapshots is further divided into two substeps: generating the snapshot space over all coarse neighborhoods ω and then improving their linear independence.

Step 2.1. Computing snapshots: For each coarse neighborhood ω , let $J_h(\partial\omega)$ denote the set of fine nodes on $\partial\omega$. Let $\delta_k \in C^0(\partial\omega)$ denote the shape function

associated with the node $x_k \in J_h(\partial\omega)$. i.e., $\delta_k \in C^0(\partial\omega)$ is the piecewise linear function that takes value 1 on the node x_k and vanishes on all other nodes. For each δ_k , it generates two Brinkman extensions:

$$\psi_{k,x} = \mathcal{H}((\delta_k, 0)) \quad \text{and} \quad \psi_{k,y} = \mathcal{H}((0, \delta_k)).$$

Now the raw snapshot space on ω is given by

$$\tilde{V}_{\text{snap}}^\omega = \text{span}\{\psi_{i,x}, \psi_{i,y} : \text{for all } x_i \in J_h(\partial\omega)\} + \text{span}\{(1, 0), (0, 1)\}.$$

Here, we artificially add two constant vectors in the basis; see Remark V.3.3 below for the discussions.

Step 2.2: Improving linear independence of snapshots: After obtaining a family of local functions for each coarse neighborhood, we need to discard the possible linearly dependent local snapshots. To this end, we use a spectral problem based on the Euclidian inner product. Specifically, Let U be a matrix with columns being the local snapshots vector representation. We extract the important modes of U through the spectral decomposition of $U^T U$. In this manner, we keep the linearly independent snapshots for each coarse neighborhood ω and denote the resulting space by

$$V_{\text{snap}}^\omega = \text{span}\{\psi_l^{\omega, \text{snap}} : 1 \leq l \leq L^\omega\},$$

with L^ω being the number of local basis functions for the coarse neighborhood ω .

V.3.0.0.3 Step 3: Building the offline space V^{off} . In this final step, we build the global offline space V^{off} from the snapshot spaces V_{snap}^ω , and it involves two substeps: constructing local offline space and constructing global offline space.

Step 3.1: Local multiscale space $\tilde{V}_{\text{off}}^\omega$. The idea at this step is to extract only important information from the computed local snapshots V_{snap}^ω corresponding to each coarse neighborhood ω . This can be achieved by performing a dimension reduction procedure in the space V_{snap}^ω . Namely, we consider the following spectral eigenvalue problem:

$$A\hat{\Psi}_k^{\omega,\text{off}} = \lambda_k S\hat{\Psi}_k^{\omega,\text{off}}, \quad (\text{V.8})$$

where the matrices A and S are defined by

$$\begin{aligned} A = [a_{mn}] &= \int_{\omega} \kappa(x) \nabla \psi_m^{\omega,\text{snap}} \cdot \nabla \psi_n^{\omega,\text{snap}}, \quad 1 \leq m, n \leq L^\omega \\ S = [s_{mn}] &= \int_{\omega} \kappa(x) \psi_m^{\omega,\text{snap}} \psi_n^{\omega,\text{snap}}, \quad 1 \leq m, n \leq L^\omega. \end{aligned}$$

Then we reorder the eigenvalues λ_k are in an ascending order, and denote $\hat{\Psi}_k^{\omega,\text{off}}$ as the corresponding eigenvectors.

To generate the offline space, we then choose the M_{off} smallest eigenvalues of (V.8) and the corresponding eigenvectors in the respective space of snapshots by setting $\tilde{\Psi}_k^{\omega,\text{off}} = \sum_j \hat{\Psi}_{kj}^{\text{off}} \psi_j^{\omega,\text{snap}}$, where $\hat{\Psi}_{kj}^{\text{off}}$ are the coordinates of the vector $\hat{\Psi}_k^{\omega,\text{off}}$. We then construct the offline space $\tilde{V}_{\text{off}}^\omega$ corresponding to the coarse neighborhood ω as

$$\tilde{V}_{\text{off}}^\omega = \text{span} \left(\tilde{\Psi}_1^{\omega,\text{off}}, \dots, \tilde{\Psi}_{M_{\text{off}}}^{\omega,\text{off}} \right).$$

We note that this step is performed only on each coarse neighborhood ω . The dimensionality of the space $\tilde{V}_{\text{off}}^\omega$ solely depends on the eigenvalue problem (V.8) within the neighborhood ω . It is known that this space is related to important features of the media (cf. [42]) such as high-conductivity channels and inclusions, and thus its dimensionality depends on the structure of the heterogeneities.

Remark V.3.3. *In the construction of the local snapshot space, we have added constant functions in addition to spectral basis functions. Hence, the constant function, which is the eigenvectors corresponding to the zero eigenvalue of (V.8), will always be in the offline space. By the construction of the offline space, each offline space contains the partition of unity functions, and the smallest offline space consists of those partition of unity functions only. This will be crucial in the stability analysis of the methods in Section V.5.*

Step 3.2: Construction of the global offline space V^{off} by partition of unity.

The local multiscale spaces $\tilde{V}_{\text{off}}^{\omega}$ are defined only on each neighborhood ω . However, it is not conforming if we simply extend the functions by 0 to the whole domain. We obtain a global conforming offline space V^{off} as follows.

First, we multiply each local offline space $\tilde{V}_{\text{off}}^{\omega}$ by the corresponding partition of unity function χ :

$$\chi\tilde{V}_{\text{off}}^{\omega} = \text{span} \left(\chi\tilde{\Psi}_1^{\omega, \text{off}}, \dots, \chi\tilde{\Psi}_{M_{\text{off}}}^{\omega, \text{off}} \right).$$

Then the space $\chi\tilde{V}_{\text{off}}^{\omega} \subset H_0^1(\omega)$, and we can extend the functions in $\chi\tilde{V}_{\text{off}}^{\omega}$ to the whole domain D by zero, which is still denoted as $\chi\tilde{V}_{\text{off}}^{\omega}$. Finally, we need to make a correction of the divergence of the resulting functions to satisfy the following condition:

$$\nabla \cdot V^{\text{off}} \subset W^{\text{off}}.$$

To this end, for each basis function $\chi\tilde{\Psi}_i^{\omega, \text{off}}$, within each coarse block $K \subset \omega$, we keep its trace along ∂K and modify its interior values to be the Brinkman extension $\mathcal{H}(\chi\tilde{\Psi}_i^{\omega, \text{off}}|_{\partial K})$. We denote this modified space by $\mathcal{H}(\chi\tilde{V}_{\text{off}}^{\omega})$. The global offline space V^{off} results from assembling all these modified local spaces as:

$$V^{\text{off}} := \{v \in (H_0^1(D))^d : v|_{\omega} \in \mathcal{H}(\chi\tilde{V}_{\text{off}}^{\omega})\}.$$

This completes the construction of the offline space V^{off} . Finally, we refer to Section V.2 for the coupling of the offline basis functions.

V.4 Numerical results

Now we test our framework with several examples. In our experiments, we take the domain $D = [0, 1] \times [0, 1]$, the source term $f = 0$, and the boundary condition is the constant horizontal velocity:

$$g = (1, 0) \quad \text{on} \quad \partial D.$$

We study the model with different (inverse) permeability fields κ^{-1} depicted in Figure V.2. Figure V.2(a) shows a fast Darcy flow goes through the slower region; in Figure V.2(b), we exhibit a slower Darcy flow past Darcy flow regions; in Figure V.2(c), a free flow going across the Darcy flow region is represented; and in Figure V.2(d), a Darcy flow passing the strong free flow region is shown.

We divide the computational domain $D = [0, 1] \times [0, 1]$ into $N_f = 1/h^2$ equal squares (where each square is further divided into two triangles), and use P_2/P_0 elements on the fine mesh with $h = 1/100$. We use a coarse-mesh size $H = 1/10$, where we divide the domain $D = [0, 1] \times [0, 1]$ into $1/H^2$ squares.

We depict the fine-scale solution, and three coarse-scale solutions with coarse spaces of dimensions 798, 1110 and 2726 in Figure V.3. The dimension of the fine scale velocity space V_h is 80802. In these numerical tests, we use the value of the inverse of permeability field κ^{-1} from Figure V.2(a). We observe that a larger coarse space yields a better approximation of the fine-scale solution. Further, we have the following observations.

- (a) The use of one single basis function for each node gives large errors and thus

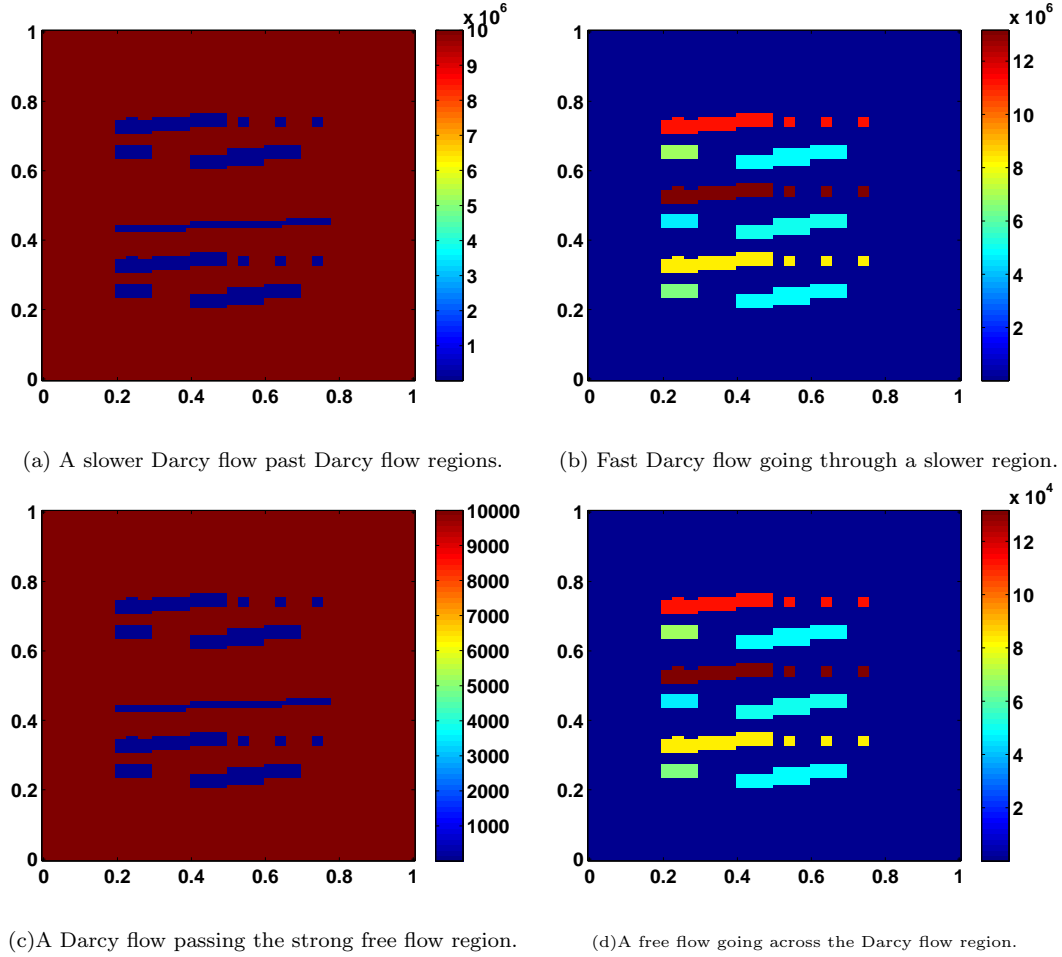


Figure V.2: Four representative inverse permeability fields κ^{-1} .

it is necessary to add spectral basis functions.

- (b) The error decreases as more spectral basis functions are added in each coarse-grid block.
- (c) The error decreases if the solution displays fast flow in some regions instead of Darcy flow over the whole region under the same contrast.

In Tables V.1-V.4, we present the results with the multiscale partition of unity functions as required by the conforming Galerkin formulation corresponding to per-

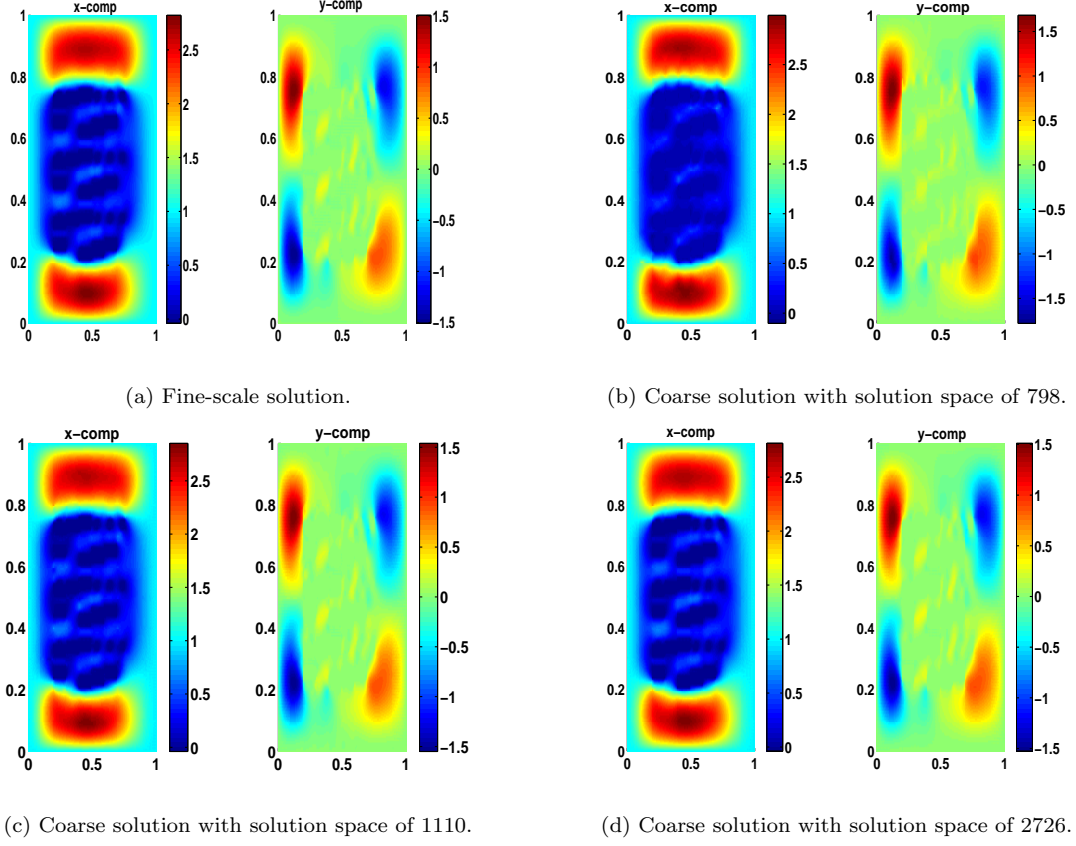


Figure V.3: The fine-scale solution and three coarse-scale solutions with different dimensions of coarse spaces using the inverse permeability field κ^{-1} in Figure V.2 (b).

meability fields in Figure V.2. In the tables, the first column shows the dimension of the offline space V^{off} , and the L^2 -weighted error between the offline solution u^{off} and the fine-scale solution u and the H^1 -weighted energy error are calculated respectively by

$$\|u - u^{\text{off}}\|_{L^2_\kappa(D)} = \frac{\|\kappa^{-1/2}(u - u^{\text{off}})\|_{L^2(D)}}{\|\kappa^{-1/2}u\|_{L^2(D)}} \quad \text{and} \quad \|u - u^{\text{off}}\|_{H^1_\kappa(D)} = \frac{\|\kappa^{-1/2}\nabla(u - u^{\text{off}})\|_{L^2(D)}}{\|\kappa^{-1/2}\nabla u\|_{L^2(D)}}.$$

In Table V.1, we display the velocity error results using a values of κ^{-1} larger

Table V.1: Numerical results for problem (V.1) with κ^{-1} in Figure V.2(b). The L^2 -weighted error and energy error are 66.34% and 99.73% for the MsFEM solution. In the simulation, the dimension of the snapshot space is fixed at 4498 with a weighted L^2 and energy relative error 1.26% and 2.13%.

$\dim(V_{\text{off}})$	$\ u - u^{\text{off}}\ $ (%)	
	$L^2_{\kappa}(D)$	$H^1_{\kappa}(D)$
888	35.46	74.91
1372	26.62	58.25
2028	11.79	26.05
2204	8.61	19.47

in the background, with smaller inclusions values, cf. Figure V.2(a). For simplicity, we set a threshold value λ^{off} for selecting eigenvectors in the construction of the offline space. Specifically, for each coarse neighborhood ω , the offline space consists of those eigenvectors in Eq. (V.8) with eigenvalues $\lambda_k \geq \lambda^{\text{off}}$. Notice that the smaller is λ^{off} , the larger is the velocity offline space. In the simulation, the choices $\lambda^{\text{off}} = 1/3, 1/4, 1/7$, and $1/10$ give the offline spaces of dimension 888, 1372, 2028 and 2204, respectively. It is observed from Table V.1 that the error decreases from 74.91% to 19.47%.

Table V.2: Numerical results for problem (V.1) with κ^{-1} in Figure V.2(a). The L^2 -weighted error and energy error are 74.68% and 130.42% for the MsFEM solution. In the simulation, the dimension of the snapshot space is fixed at 4498 with a weighted L^2 and energy relative error 1.33% and 13.03%.

$\dim(V_{\text{off}})$	$\ u - u^{\text{off}}\ $ (%)	
	$L^2_{\kappa}(D)$	$H^1_{\kappa}(D)$
682	7.86	36.90
1512	1.85	18.37
2230	1.51	15.27
2744	1.38	13.84

The results in Table V.2 are calculated with values of κ^{-1} that are large in inclusions, and small in the background, cf. Figure V.2(b). Compared with results in Table V.1, the errors in Table V.2 are slightly better in the sense that the relative energy errors are smaller when using the same dimensional offline space. In this numerical test, we take $\lambda^{\text{off}} = 1/3, 1/4, 1/7$, and $1/10$ with the offline space of dimension 682, 1512, 2230 and 2744 respectively. From Table V.2, the energy errors decrease from 36.90% to 13.84%.

Table V.3: Numerical results for problem (V.1) with κ^{-1} in Figure V.2(d). The L^2 -weighted error and energy error are 85.25% and 73.85% for the MsFEM solution. In the simulation, the dimension of the snapshot space is fixed at 4498 with a weighted L^2 and energy relative error 1.94% and 3.54%.

$\dim(V_{\text{off}})$	$\ u - u^{\text{off}}\ $ (%)	
	$L_{\kappa}^2(D)$	$H_{\kappa}^1(D)$
834	35.58	38.10
1512	14.34	19.41
2084	6.81	9.90
2306	4.54	7.65

In Tables V.3 and V.4, we employ certain inverse permeability fields κ^{-1} to get fast flow and Darcy flow simultaneously. In Table V.3, we use the value of κ^{-1} small in inclusions, and large in the background, cf. Figure V.2(c). In this numerical test, we take $\lambda^{\text{off}} = 1/3, 1/4, 1/7$, and $1/10$ with the offline space of dimension 834, 1512, 2084 and 2316 respectively. From Table V.3, the energy errors decrease from 38.10% to 7.65%. In Table V.4, we experimented with values of κ^{-1} large in inclusions, and small in the background as shown in Figure V.2(d). In this numerical test, we take $\lambda^{\text{off}} = 1/3, 1/4, 1/7$, and $1/10$ with the offline space of dimension 682, 1090, 1992 and 3344 respectively. From Table V.4, the energy error decreases from 43.26% to

5.38%.

Table V.4: Numerical results for problem (V.1) with κ^{-1} in Figure V.2(c). The L^2 -weighted error and energy error are 74.68% and 130.42% for the MsFEM solution. In the simulation, the dimension of the snapshot space is fixed at 4498 with a weighted L^2 and energy relative error 1.47% and 3.75%.

$\dim(V_{\text{off}})$	$\ u - u^{\text{off}}\ $ (%)	
	$L^2_{\kappa}(D)$	$H^1_{\kappa}(D)$
682	46.80	43.26
1090	30.92	30.30
1992	13.49	13.15
3344	6.36	5.38

In Table V.3, the solution represents fast flow in the inclusions (with high permeability value) and Darcy flow in the background, whereas in Table V.4, the solution is a fast flow in the background (with high permeability value) and Darcy flow in the inclusions. The results in these four tables indicate that the errors are smaller when fast flow exists.

V.5 Convergence analysis

In this section, we present a priori error estimates for the multiscale method proposed above. we first derive the stability argument. Then we show the approximation property of the method. For the sake of simplicity, we assume a homogeneous boundary condition $g = 0$ in the Brinkman equation (V.1).

V.5.1 Stability argument

To prove the stability of the method, we apply the well known *inf-sup* argument. First, we define a norm on $V(D)$ by

$$\|u\|_{V,D}^2 = a(u, u) + M \langle \operatorname{div} u, \operatorname{div} u \rangle_D, \quad (\text{V.9})$$

and the norm on $W(D)$ is defined by

$$\|p\|_{P,D} = M^{-\frac{1}{2}} \|p\|_{L^2(D)}, \quad (\text{V.10})$$

where $M = \max(\|\kappa^{-1}\|_{L^\infty(D)}, 1)$. We also define the following two null spaces:

$$\begin{aligned} Z &:= \{v \in V(D) : b(v, p) = 0, \quad \text{for all } p \in W(D)\}, \\ Z^{\text{off}} &:= \{v \in V^{\text{off}} : b(v, p) = 0, \quad \text{for all } p \in W^{\text{off}}\}. \end{aligned}$$

Under these definitions and the construction of V^{off} and W^{off} , it holds:

$$Z^{\text{off}} \subset Z, \quad a(v, v) \succeq \|v\|_{V,D}^2 \quad \text{for all } v \in Z. \quad (\text{V.11})$$

Here, and in what follows, we use the notation $A \succeq B$ to represent $A \geq \mathcal{C}B$ with a constant \mathcal{C} independent of the contrast and the functions involve, and a similar interpretation applies to the notation \preceq . The above two results imply that the bilinear form $a(\cdot, \cdot)$ is also coercive on Z^{off} .

We first verify that the continuous problem (V.1) satisfies the *inf-sup* condition.

Lemma V.5.1. *Let $\|\cdot\|_{V,D}$ and $\|\cdot\|_{P,D}$ be defined in (V.9) and (V.10). Then the*

following inf-sup condition holds independent of the contrast

$$\sup_{v \in V(D) \setminus \{0\}} \frac{\langle \operatorname{div} v, q \rangle_D}{\|v\|_{V,D}} \succeq \|q\|_{P,D}, \text{ for all } q \in W(D). \quad (\text{V.12})$$

Proof. It is well known [19] that the operator $b(\cdot, \cdot)$ satisfies the *inf-sup* condition under the standard norms, i.e.,

$$\sup_{v \in V(D) \setminus \{0\}} \frac{\langle \operatorname{div} v, q \rangle_D}{\|v\|_{H^1(D)}} \succeq \|q\|_{L^2(D)}, \text{ for all } q \in W(D). \quad (\text{V.13})$$

By the definition of $\|\cdot\|_{V,D}$ and $\|\cdot\|_{P,D}$, we have $\|v\|_{V,D} \leq M^{\frac{1}{2}} \|v\|_{H^1(D)}$, and $\|q\|_{L^2(D)} = M^{\frac{1}{2}} \|q\|_{P,D}$ for all $(v, q) \in V(D) \times W(D)$. Combining these facts with (V.13) completes the proof. \square

Next, we show that the discrete problem (V.5) also satisfies this type of inf-sup condition with a constant independent of the contrast for every offline space $V^{\text{off}} \times W^{\text{off}}$. First, we consider the following auxiliary space:

$$V_H(D) := \{v \in H^1(D) \mid v|_K \in Q^2(K), \forall K \in \mathcal{T}_H\},$$

$$W_H(D) := \{q \in L_0^2(D) \mid q|_K \in Q^0(K), \forall K \in \mathcal{T}_H\}.$$

For the Brinkman model, we have the following inf-sup condition in $V_H(D) \times W_H(D)$ (see [17]),

$$\sup_{v \in V_H(D) \setminus \{0\}} \frac{\langle \operatorname{div} v, q \rangle_D}{\|v\|_{H^1(D)}} \succeq \|q\|_{L^2(D)}, \text{ for all } q \in W_H(D). \quad (\text{V.14})$$

Following the proof of Lemma V.5.1, we can obtain the discrete inf-sup condition in

$V_H(D) \times W_H(D)$ with $\|\cdot\|_{V,D}$ and $\|\cdot\|_{P,D}$, i.e.,

$$\sup_{v \in V_H(D) \setminus \{0\}} \frac{\langle \operatorname{div} v, q \rangle_D}{\|v\|_{V,D}} \succeq \|q\|_{P,D}, \quad \text{for all } q \in W_H(D). \quad (\text{V.15})$$

To prove the *inf-sup* condition for the space $V^{\text{off}} \times W^{\text{off}}$, we need the following result, which states the stability of the Brinkman extension with respect to the weighted norm defined in (V.9).

Lemma V.5.2. *For any $w \in (H^1(K))^d$, the Brinkman extension $\mathcal{H}(w)$ of w on K satisfies*

$$\|\mathcal{H}(w)\|_{V,K} \preceq \|w\|_{V,K}. \quad (\text{V.16})$$

Proof. By the definition of the Brinkman extension, $(\mathcal{H}(w), p) \in (H(K))^d \times L_0^2(K)$ satisfies

$$\begin{aligned} \nabla p - \Delta \mathcal{H}(w) + \kappa^{-1} \mathcal{H}(w) &= 0, \quad \text{in } K, \\ \operatorname{div} \mathcal{H}(w) &= \frac{\int_{\partial K} w \cdot n}{|K|} \quad \text{in } K, \\ \mathcal{H}(w) &= w, \quad \text{on } \partial K. \end{aligned}$$

Denote $v = \mathcal{H}(w) - w$, then v satisfies

$$\begin{aligned} \nabla p - \Delta v + \kappa^{-1} v &= \Delta w - \kappa^{-1} w, \quad \text{in } K, \\ \operatorname{div} v &= \frac{\int_{\partial K} w \cdot n}{|K|} - \operatorname{div} w \quad \text{in } K, \\ v &= 0, \quad \text{on } \partial K. \end{aligned} \quad (\text{V.17})$$

Since $p \in L_0^2(K)$, by Lemma 11.2.3 in [17], there exists $\phi \in (H_0^1(K))^d$ such that

$$p = -\operatorname{div} \phi \quad \text{and} \quad \|\phi\|_{H^1(K)} \preceq \|p\|_{L^2(K)}. \quad (\text{V.18})$$

Multiplying Eq. (V.17) by ϕ and integrating by parts, we obtain,

$$\langle p, p \rangle_K + \langle \nabla v, \nabla \phi \rangle_K + \langle \kappa^{-1} v, \phi \rangle_K = -\langle \nabla w, \nabla \phi \rangle_K - \langle \kappa^{-1} w, \phi \rangle_K.$$

Thus

$$\langle p, p \rangle_K = -\langle \nabla v, \nabla \phi \rangle_K - \langle \kappa^{-1} v, \phi \rangle_K - \langle \nabla w, \nabla \phi \rangle_K - \langle \kappa^{-1} w, \phi \rangle_K.$$

Using the Cauchy-Schwarz inequality and (V.18), we arrive at,

$$\begin{aligned} \|p\|_{L^2(K)}^2 &\preceq (\|\nabla v\|_{L^2(K)} + \|\kappa^{-1} v\|_{H^{-1}(K)} + (\|\nabla w\|_{L^2(K)} + \|\kappa^{-1} w\|_{H^{-1}(K)})) \|p\|_{L^2(K)} \\ &\preceq (\|\nabla v\|_{L^2(K)} + M \|\kappa^{-\frac{1}{2}} v\|_{L^2(K)} + \|\nabla w\|_{L^2(K)} + M \|\kappa^{-\frac{1}{2}} w\|_{L^2(K)}) \|p\|_{L^2(K)}. \end{aligned}$$

Then it yields the pressure estimate

$$\|p\|_{L^2(K)} \preceq \|\nabla v\|_{L^2(K)} + M \|\kappa^{-\frac{1}{2}} v\|_{L^2(K)} + \|\nabla w\|_{L^2(K)} + M \|\kappa^{-\frac{1}{2}} w\|_{L^2(K)}. \quad (\text{V.19})$$

Multiplying Eq. (V.17) by v and integrating by parts, yields,

$$-\langle p, \operatorname{div} v \rangle_K + \langle \nabla v, \nabla v \rangle_K + \langle \kappa^{-1} v, v \rangle_K = \langle \Delta w - \kappa^{-1} w, v \rangle_K.$$

Using Cauchy-Schwarz inequality and the fact that p has zero mean on K , it follows

that,

$$\begin{aligned}
\langle \nabla v, \nabla v \rangle_K + \langle \kappa^{-1} v, v \rangle_K &= \langle \Delta w - \kappa^{-1} w, v \rangle_K + \langle p, \operatorname{div} v \rangle_K \\
&= \langle \Delta w - \kappa^{-1} w, v \rangle_K + \langle p, \operatorname{div} (\mathcal{H}(w) - w) \rangle_K \\
&= \langle \Delta w - \kappa^{-1} w, v \rangle_K - \langle p, \operatorname{div} w \rangle_K \\
&\leq \|\nabla w\|_{L^2(K)} \|\nabla v\|_{L^2(K)} + \left\| \kappa^{-\frac{1}{2}} w \right\|_{L^2(K)} \left\| \kappa^{-\frac{1}{2}} v \right\|_{L^2(K)} + \|p\|_{L^2(K)} \|\operatorname{div} w\|_{L^2(K)}.
\end{aligned}$$

Inserting the pressure estimate (V.19) and Young's inequality, we deduce

$$\begin{aligned}
\langle \nabla v, \nabla v \rangle_K + \langle \kappa^{-1} v, v \rangle_K &\leq \frac{1}{2\delta} (\|\nabla w\|_{L^2(K)}^2 + \left\| \kappa^{-\frac{1}{2}} w \right\|_{L^2(K)}^2) \\
&\quad + \frac{\delta}{2} \left(\|\nabla v\|_{L^2(K)}^2 + \left\| \kappa^{-\frac{1}{2}} v \right\|_{L^2(K)}^2 \right) \\
&\quad + \frac{\delta}{2M} \left(\|\nabla v\|_{L^2(K)}^2 + M \left\| \kappa^{-\frac{1}{2}} v \right\|_{L^2(K)}^2 + \|\nabla w\|_{L^2(K)}^2 \right. \\
&\quad \left. + M \left\| \kappa^{-\frac{1}{2}} w \right\|_{L^2(K)}^2 \right) + \frac{M}{2\delta} \|\operatorname{div} w\|_{L^2(K)}^2.
\end{aligned}$$

Now the choice $\delta = \frac{1}{4}$ yields

$$\langle \nabla v, \nabla v \rangle_K + \langle \kappa^{-1} v, v \rangle_K \preceq \|\nabla w\|_{L^2(K)}^2 + \left\| \kappa^{-\frac{1}{2}} w \right\|_{L^2(K)}^2 + M \|\operatorname{div} w\|_{L^2(K)}^2 = \|w\|_{V,K}^2.$$

Recall that $\mathcal{H}(w) = v + w$. By triangle inequality, we have

$$\langle \nabla \mathcal{H}(w), \nabla \mathcal{H}(w) \rangle_K + \langle \kappa^{-1} \mathcal{H}(w), \mathcal{H}(w) \rangle_K \preceq \|w\|_{V,K}^2.$$

It suffices to show

$$M^{\frac{1}{2}} \|\operatorname{div} \mathcal{H}(w)\|_{L^2(K)} \preceq \|w\|_{V,K}. \tag{V.20}$$

Indeed from the compatibility condition, we obtain: $\operatorname{div} \mathcal{H}(w) = \frac{1}{|K|} \int_K \operatorname{div} w$. Hence,

$$|\operatorname{div} \mathcal{H}(w)| = \left| \frac{1}{|K|} \int_K \operatorname{div} w \right| \leq \frac{1}{|K|} \int_K |\operatorname{div} w| \leq \|\operatorname{div} w\|_{L^2(K)} |K|^{-\frac{1}{2}},$$

where in the last step we used Cauchy-Schwarz inequality. Consequently

$$\|\operatorname{div} \mathcal{H}(w)\|_{L^2(K)}^2 \preceq \|\operatorname{div} w\|_{L^2(K)}^2 |K|^{-1} |K| = \|\operatorname{div} w\|_{L^2(K)}^2,$$

This completes the proof. \square

We are now ready to show the *inf-sup* condition in the space $V^{\text{off}} \times W^{\text{off}}$.

Lemma V.5.3. *For $\|\cdot\|_{V,D}$ and $\|\cdot\|_{P,D}$ defined in (V.9) and (V.10), we have the following inf-sup condition with inf-sup constant independent of the contrast*

$$\sup_{v \in V^{\text{off}}(D) \setminus \{0\}} \frac{\langle \operatorname{div} v, q \rangle_D}{\|v\|_{V,D}} \succeq \|q\|_{P,D}, \quad \text{for all } q \in W^{\text{off}}(D). \quad (\text{V.21})$$

Proof. First note $W^{\text{off}} = W_H(D)$. By (V.15), we have

$$\sup_{v \in V_H(D) \setminus \{0\}} \frac{\langle \operatorname{div} v, q \rangle_D}{\|v\|_{V,D}} \succeq \|q\|_{P,D}, \quad \text{for all } q \in W^{\text{off}}.$$

For any $v \in V_H(D)$, let $\mathcal{H}(v)$ be the Brinkman extension of $v|_{\mathcal{E}_H}$, i.e., $\mathcal{H}(v)$ takes the value of v on the skeleton \mathcal{E}_H and is extended to the interior by Brinkman extension within each coarse block. Then $v|_F \in [P^2(F)]^2$, $\forall F \in \mathcal{E}_H$. According to the construction of the offline space V^{off} in Section V.3, we have

$$\mathcal{H}(v) \in V^{\text{off}}.$$

Moreover, for any $q \in W^{\text{off}}$, q is piecewise constant on each coarse block. By combining this fact and the definition of Brinkman extension, we have

$$\langle \operatorname{div} v, q \rangle_K = \langle \operatorname{div} \mathcal{H}(v), q \rangle_K,$$

for every coarse block K . Finally, we complete the proof by using Lemma V.5.2:

$$\begin{aligned} \|q\|_{P,D} &\preceq \sup_{v \in V_H(D) \setminus \{0\}} \frac{\langle \operatorname{div} v, q \rangle_D}{\|v\|_{V,D}} = \sup_{v \in V_H(D) \setminus \{0\}} \frac{\langle \operatorname{div} \mathcal{H}(v), q \rangle_D}{\|v\|_{V,D}} \\ &\preceq \sup_{v \in V_H(D) \setminus \{0\}} \frac{\langle \operatorname{div} \mathcal{H}(v), q \rangle_D}{\|\mathcal{H}(v)\|_{V,D}} \preceq \sup_{v \in V^{\text{off}}(D) \setminus \{0\}} \frac{\langle \operatorname{div} v, q \rangle_D}{\|v\|_{V,D}}. \end{aligned}$$

□

Now by combining Lemma V.5.1, Lemma V.5.3 and (V.11), we obtain the following stability result, by repeating the proof of Theorem 3.2 in [73].

Theorem V.5.4. *Let $(u, p) \in V(D) \times W(D)$ and $(u_0, p_0) \in V^{\text{off}}(D) \times W^{\text{off}}(D)$ be the Galerkin solutions of problem (V.1) and problem (V.5) respectively. We have*

$$\|u - u_0\|_{V,D} \preceq \inf_{w \in V^{\text{off}}(D)} \|u - w\|_{V,D}. \quad (\text{V.22})$$

V.5.2 Convergence results

Now we derive an error estimate for our method. To this end, we first give several basic estimates on the Brinkman extension.

Lemma V.5.5. *For each partition of unity function χ_i with support ω_i , let $(u_c, p_c) \in$*

$(H^1(\omega_i))^d \times L_0^2(\omega_i)$ solve

$$\begin{aligned} \nabla p_c - \Delta u_c + \kappa^{-1} u_c &= 0 & \text{in } \omega_i, \\ \operatorname{div} u_c &= \frac{\int_{\partial\omega_i} g \cdot n}{|\omega_i|} & \text{in } \omega_i, \\ u_c &= g & \text{on } \partial\omega_i. \end{aligned}$$

Then the following a priori estimate holds

$$\int_{\omega_i} \chi_i^2 |\nabla u_c|^2 + \int_{\omega_i} \kappa^{-1} \chi_i^2 |u_c|^2 \preceq \int_{\omega_i} |\nabla \chi_i|^2 |u_c|^2 + \int_{\omega_i} \kappa^{-2} |u_c|^2 + \int_{\omega_i} |\operatorname{div} u_c|^2 + \|p_c\|_{L^2(\omega_i)}^2. \quad (\text{V.23})$$

Proof. Multiplying the equation by $\chi_i^2 u_c$ yields

$$-\langle p_c, \operatorname{div}(\chi_i^2 u_c) \rangle_{\omega_i} + \langle \nabla u_c, \nabla(\chi_i^2 u_c) \rangle_{\omega_i} + \langle \kappa^{-1} u_c, \chi_i^2 u_c \rangle_{\omega_i} = 0.$$

Some simple algebraic manipulations give

$$\begin{aligned} & \int_{\omega_i} \chi_i^2 |\nabla u_c|^2 + \int_{\omega_i} \kappa^{-1} \chi_i^2 u_c^2 \\ &= \langle p_c, 2\chi_i \nabla \chi_i \cdot u_c \rangle_{\omega_i} + \langle p_c, \chi_i^2 \operatorname{div} u_c \rangle_{\omega_i} - \langle \nabla u_c, 2\chi_i \nabla \chi_i \cdot u_c \rangle_{\omega_i}, \\ &\preceq \|p_c\|_{L^2(\omega_i)} (\|\nabla \chi_i \cdot u_c\|_{L^2(\omega_i)} + \|\operatorname{div} u_c\|_{L^2(\omega_i)}) + \|\chi_i \nabla u_c\|_{L^2(\omega_i)} \|\nabla \chi_i \cdot u_c\|_{L^2(\omega_i)}, \\ &\leq \frac{\delta}{2} (\|p_c\|_{L^2(\omega_i)}^2 + \|\chi_i \nabla u_c\|_{L^2(\omega_i)}^2) + \frac{1}{2\delta} (\|\nabla \chi_i \cdot u_c\|_{L^2(\omega_i)}^2 + \|\operatorname{div} u_c\|_{L^2(\omega_i)}^2). \end{aligned}$$

Taking $\delta = \frac{1}{4}$, we obtain the desired inequality. \square

Lemma V.5.6. *Let $\omega_i \subset \mathcal{T}_H$ be an arbitrary coarse neighborhood. Let $(u_N, p_N) \in$*

$(H_0^1(\omega_i))^d \times L_0^2(\omega_i)$ solve

$$\nabla p_N - \Delta u_N + \kappa^{-1} u_N = f \quad \text{in } \omega_i,$$

$$\operatorname{div} u_N = 0 \quad \text{in } \omega_i,$$

$$u_N = 0 \quad \text{on } \partial\omega_i.$$

Then there holds

$$\|u_N\|_{V, \omega_i} \preceq H \|f\|_{L^2(\omega_i)}. \quad (\text{V.24})$$

Proof. By multiplying the first equation by u_N , integrating by parts and the divergence free property of u_N , we obtain

$$\|\nabla u_N\|_{L^2(\omega_i)}^2 + \left\| \kappa^{-\frac{1}{2}} u_N \right\|_{L^2(\omega_i)}^2 = \langle f, u_N \rangle_{\omega_i}.$$

In view of the boundary condition, we can apply Poincaré's inequality,

$$\|u_N\|_{L^2(\omega_i)} \preceq H \|\nabla u_N\|_{L^2(\omega_i)}.$$

Thus

$$\|\nabla u_N\|_{L^2(\omega_i)}^2 + \left\| \kappa^{-\frac{1}{2}} u_N \right\|_{L^2(\omega_i)}^2 = \langle f, u_N \rangle_{\omega_i} \preceq H \|\nabla u_N\|_{L^2(\omega_i)} \|f\|_{L^2(\omega_i)}.$$

Finally, we complete the proof by the Young's inequality. \square

Now we are ready to state our main error estimate.

Theorem V.5.7. *Let $\Lambda_* = \min_{\omega_i} \lambda_{L_i+1}^{\omega_i}$. Then*

$$\|u - u_0\|_{V,D}^2 \preceq \frac{1}{\Lambda_*} \|\nabla u\|_{L^2(D)}^2 + H^2 \|f(x)\|_{L^2(D)}^2 + \|p_c\|_{L^2(D)}^2.$$

where p_c is defined by (V.25) below.

Proof. In view of the linearity of the equation (V.1), on each coarse neighborhood $\omega_i \subset \mathcal{T}_H$, u can be decomposed into $u = \mathcal{H}(u) + u_N$, where $\mathcal{H}(u)$ is the Brinkman extension of u and u_N is the residual in Lemma V.5.6. For each χ_i , let $I^0 u$ be the local interpolant of u in the local offline space $\tilde{V}_{\text{off}}^{\omega_i}$. Then there exists $p_c \in L^2(\omega_i)$, s.t.

$$\begin{aligned} \nabla p_c - \Delta(u - I^0 u) + \kappa^{-1}(u - I^0 u) &= 0 & \text{in } \omega_i, \\ \operatorname{div}(u - I^0 u) &= \frac{\int_{\partial\omega_i} h_i \cdot n}{|\omega_i|} & \text{in } \omega_i, \\ (u - I^0 u) &= h_i & \text{on } \partial\omega_i, \end{aligned} \tag{V.25}$$

since $I^0 u$ equals 0 over $\partial\omega_i$ (the support of χ_i is ω_i) and each basis in $\tilde{V}_{\text{off}}^{\omega_i}$ has the properties of divergence constant. Here, h_i denotes the boundary value of $u - I^0 u$ over $\partial\omega_i$.

By the construction of the offline space V^{off} , $\mathcal{H}(\chi_i I^0 u) \in V^{\text{off}}$. By Theorem V.5.4,

we have

$$\begin{aligned}
\|u - u_0\|_{V,D}^2 &\preceq \inf_{v \in V^{\text{off}}} \|u - v\|_{V,D}^2 \\
&\preceq \left\| u - \sum_{i=1}^{N_c} \mathcal{H}(\chi_i I^0 u) \right\|_{V,D}^2 \preceq \left\| \mathcal{H}(u) - \sum_{i=1}^{N_c} \mathcal{H}(\chi_i I^0 u) \right\|_{V,D}^2 + \|u_N\|_{V,D}^2, \\
&\preceq \left\| \mathcal{H}\left(\sum_{i=1}^{N_c} \chi_i u\right) - \sum_{i=1}^{N_c} \mathcal{H}(\chi_i I^0 u) \right\|_{V,D}^2 + H^2 \|f(x)\|_{L^2(\omega_i)}^2.
\end{aligned}$$

Here the last step follows from the estimate in Lemma V.5.6. For the first term, we have

$$\begin{aligned}
\left\| \mathcal{H}\left(\sum_{i=1}^{N_c} \chi_i u\right) - \sum_{i=1}^{N_c} \mathcal{H}(\chi_i I^0 u) \right\|_{V,D}^2 &= \left\| \mathcal{H}\left(\sum_{i=1}^{N_c} (\chi_i u - \chi_i I^0 u)\right) \right\|_{V,D}^2 \\
&\preceq \sum_{i=1}^{N_c} \left\| \mathcal{H}(\chi_i u - \chi_i I^0 u) \right\|_{V,\omega_i}^2 \preceq \sum_{i=1}^{N_c} \left\| \chi_i (u - I^0 u) \right\|_{V,\omega_i}^2,
\end{aligned}$$

where at the last step we have applied Lemma V.5.2 on each coarse neighborhood ω_i . Consequently,

$$\begin{aligned}
\|u - u_0\|_{V,D}^2 &\preceq \sum_{i=1}^{N_c} \left\| \chi_i (u - I^0 u) \right\|_{V,\omega_i}^2 + H^2 \|f\|_{L^2(\omega_i)}^2 \\
&\preceq \sum_{i=1}^{N_c} \int_{\omega_i} \chi_i^2 |\nabla(u - I^0 u)|^2 + \int_{\omega_i} \kappa^{-1} \chi_i^2 |u - I^0 u|^2 \\
&\quad + M \int_{\omega_i} \chi_i^2 |\operatorname{div}(u - I^0 u)|^2 + M \int_{\omega_i} |\nabla \chi_i|^2 |u - I^0 u|^2 + H^2 \|f\|_{L^2(\omega_i)}^2.
\end{aligned}$$

By applying Lemma V.5.5 to the term $u - I^0 u$ in Eqn. (V.25), we deduce

$$\begin{aligned} \|u - u_0\|_{V,D}^2 &\preceq \sum_i M \int_{\omega_i} |\nabla \chi_i|^2 |u - I^0 u|^2 + \int_{\omega_i} (\kappa^{-1})^2 |u - I^0 u|^2 \\ &\quad + M \int_{\omega_i} \chi_i^2 |\operatorname{div}(u - I^0 u)|^2 + H^2 \|f\|_{L^2(\omega_i)}^2 + \|p_c\|_{L^2(\omega_i)}^2. \end{aligned}$$

Finally, using the spectral problem (V.8), with A and S defined by

$$\begin{aligned} A &= [a_{mn}] = \int_{\omega_i} (\chi_i)^2 \nabla \psi_m^{\omega, \text{snap}} \cdot \nabla \psi_n^{\omega, \text{snap}}, \\ S &= [s_{mn}] = \int_{\omega_i} (\kappa(x)^{-2} + M(\nabla \chi_i)^2) \psi_m^{\omega, \text{snap}} \cdot \psi_n^{\omega, \text{snap}} \\ &\quad + M \int_{\omega_i} (\chi_i)^2 \operatorname{div} \psi_m^{\omega, \text{snap}} \operatorname{div} \psi_n^{\omega, \text{snap}}, \end{aligned} \tag{V.26}$$

we have

$$\begin{aligned} &\int_{\omega_i} M(\nabla \chi_i)^2 |u - I^0 u|^2 + \int_{\omega_i} (\kappa^{-1})^2 |u - I^0 u|^2 + M \int_{\omega_i} (\chi_i)^2 |\operatorname{div}(u - I^0 u)|^2 \\ &\leq \frac{1}{\lambda_{L_i+1}^{\omega_i}} \int_{\omega_i} (\chi_i)^2 |\nabla(u - I^0 u)|^2. \end{aligned}$$

Hence,

$$\|u - u_0\|_{V,D}^2 \preceq \sum_i \frac{1}{\lambda_{L_i+1}^{\omega_i}} \int_{\omega_i} (\chi_i)^2 |\nabla(u - I^0 u)|^2 + H^2 \|f(x)\|_{L^2(\omega_i)}^2 + \|p_c\|_{L^2(\omega_i)}^2.$$

Upon denoting $\Lambda_* = \min_{\omega_i} \lambda_{L_i+1}^{\omega_i}$, we deduce

$$\|u - u_0\|_{V,D}^2 \preceq \frac{1}{\Lambda_*} \sum_i \int_{\omega_i} (\chi_i)^2 |\nabla(u - I^0 u)|^2 + H^2 \|f(x)\|_{L^2(\omega_i)}^2 + \|p_c\|_{L^2(\omega_i)}^2.$$

Using the inequality $\|\nabla I^0 u\|_{L^2(\omega_i)} \preceq \|\nabla u\|_{L^2(\omega_i)}$,

$$\|u - u_0\|_{V,D}^2 \preceq \frac{1}{\Lambda_*} \sum_i \|\nabla u\|_{L^2(\omega_i)}^2 + H^2 \|f(x)\|_{L^2(\omega_i)}^2 + \|p_c\|_{L^2(\omega_i)}^2,$$

and thus

$$\|u - u_0\|_{V,D}^2 \preceq \frac{1}{\Lambda_*} \|\nabla u\|_{L^2(D)}^2 + H^2 \|f(x)\|_{L^2(D)}^2 + \|p_c\|_{L^2(D)}^2.$$

This completes the proof of the theorem. \square

Remark V.5.8. *We note that in the analysis, we have used the spectral problem (V.26), instead of (V.8) in the numerical simulation. In view of the inequality $\|\operatorname{div} u\|_{L^2(D)} \leq \|\nabla u\|_{L^2(D)}$ for any $u \in (H^1(D))^d$ and the fact that χ_i is bounded, these two spectral problems are equivalent provided that M is bounded. Hence our analysis does provide partial justification for the algorithm. The constant M appears as a result of the definition of the velocity and pressure norms, cf. (V.9) and (V.10), which is needed for the inf-sup condition. It remains unclear how to get rid of the constant M in the norm definition in the convergence analysis.*

V.6 Concluding remarks

In this chapter, we have developed a mixed generalized multiscale finite element method for the Brinkman flow in high-contrast media, which capture both the Stokes flow and the Darcy flow in respective regions. In the fine grid, we approximate the velocity and pressure with piecewise quadratic and piecewise constant functions. We develop a novel approach to construct a coarse approximation for the velocity snapshot space, and a robust low-dimensional offline space for the velocity. The main feature of our approach is to select the important modes by solving certain appropriate local eigenvalue problem. The stability of the mixed GMsFEM and a priori error

estimates are derived. The two-dimensional numerical examples illustrate clearly the robustness and efficiency of our method. Besides, it also shows the consistency with the convergence analysis.

In our discussion, we have focused on the approximation of the velocity space, and simply take the piecewise constant space as the approximation space for pressure. This may not be the best choice. The mixed finite element space may get better results with a better pressure space and accordingly an enriched velocity space. Further, it is natural to extend the proposed method to the Stokes model in perforated domains ([24]).

There are many important open problems related to the Brinkman model. The first one is on the model reduction of Stokes flow in the perforated domain. Recently, Muljadi et al. [60] developed and tested a novel MsFEM for solving Stokes flow in heterogeneous media based on Crouzeix-Raviart elements. In their approach, the basis functions are calculated within each coarse element using stabilized $Q1-Q1$ elements. The results are very encouraging in terms of the L^2 error; however, the H^1 relative error of the velocity can be fairly large, especially when the number of holes in the medium is large. One possible solution to this issue is to enrich the velocity basis. Since the velocity error depends on the pressure space, and thus we need to enrich the pressure space as well. The key idea is to balance the velocity space and the pressure space in order to derive the stability estimate as required by the mixed method. This will be a subject of my future research.

Secondly, one challenge with the Brinkman model is the construction of a stable finite element discretization [73, 60]. There are many interesting works on stable FEMs for Brinkman flow. However, the definition of the norms unavoidably involves the maximum of the high contrast coefficient (i.e., the inverse of the permeability field). Hence, the convergence analysis deteriorates for the high-contrast problem,

and they can not be applied to Brinkman flow in high-contrast media directly. Further, the convergence analysis of the multiscale algorithm in [46] with optimal rate remains completely open.

VI. CONCLUSIONS

GMsFEMs for partial differential equations in high-contrast heterogeneous media are investigated in this dissertation. The general framework is provided in Chapter II for linear elliptic equations. In this chapter, strategies to improve the accuracy and efficiency are introduced and implemented, such as oversampling strategy and randomized snapshot algorithms.

In Chapter III, a posteriori error estimate is shown and two types of error indicators are proposed. Based on the reliability and efficiency of the error indicators, we propose a robust adaptive enrichment algorithm, which involves local basis enrichment instead of the refinement of grids.

In Chapter IV, the GmsFEM is extended to nonlinear elliptic equations in heterogeneous media. In this chapter, continuous Galerkin formulation and Interior Penalty Discontinuous Galerkin formulation are employed separately into the GmsFEM framework. The numerical simulations are presented to demonstrate the convergence of both approaches.

In Chapter V, the GmsFEM framework is applied to Brinkman flows in high-contrast heterogeneous media. A new type of local basis generation is proposed and analyzed. We build new norms for this problem using mixed element method, and a stability argument is derived.

REFERENCES

- [1] J.E. Aarnes. On the use of a mixed multiscale finite element method for greater flexibility and increased speed or improved accuracy in reservoir simulation. *SIAM J. Multiscale Modeling and Simulation*, 2:421–439, 2004.
- [2] J.E. Aarnes and Y. Efendiev. Mixed multiscale finite element for stochastic porous media flows. *SIAM J. Sci. Comput.*, 30 (5):2319–2339, 2008.
- [3] J.E. Aarnes, S. Krogstad, and K.-A. Lie. A hierarchical multiscale method for two-phase flow based upon mixed finite elements and nonuniform grids. *SIAM J. Multiscale Modeling and Simulation*, 5(2):337–363, 2006.
- [4] A. Abdulle and G. Vilmart. Analysis of the finite element heterogeneous multiscale method for quasilinear elliptic homogenization problems. *Math. Comp.*, 83:513–536, 2014.
- [5] Assyr Abdulle and Yun Bai. Adaptive reduced basis finite element heterogeneous multiscale method. *Comput. Methods Appl. Mech. Engrg.*, 257:203–220, 2013.
- [6] A. Adbulle and Y. Bai. Reduced basis finite element heterogeneous multiscale method for high-order discretizations of elliptic homogenization problems. *J. Comput. Phys.*, 231:7014–7036, 2012.
- [7] F. Albrecht, B. Haasdonk, M. Oehlberger, and S. Kaulmann. The localized reduced basis multiscale method. *Proceedings of Algorithmy*.
- [8] T. Arbogast. Implementation of a locally conservative numerical subgrid upscaling scheme for two-phase Darcy flow. *Comput. Geosci*, 6:453–481, 2002.
- [9] T. Arbogast and K.J. Boyd. Subgrid upscaling and mixed multiscale finite elements. *SIAM J. Numer. Anal.*, 44(3):1150–1171 (electronic), 2006.

- [10] T. Arbogast and M.S.M. Gomez. A discretization and multigrid solver for a Darcy-Stokes system of three dimensional vuggy porous media. *Comput. Geosci.*, 13(2):331–343, 2009.
- [11] T. Arbogast, G. Pencheva, M.F. Wheeler, and I. Yotov. A multiscale mortar mixed finite element method. *SIAM J. Multiscale Modeling and Simulation*, 6(1):319–346, 2007.
- [12] D. N. Arnold, F. Brezzi, B. Cockburn, and L. D. Marini. Unified analysis of discontinuous Galerkin methods for elliptic problems. *SIAM J. Numer. Anal.*, 39:1749 – 1779, 2001.
- [13] I. Babuška and R. Lipton. Optimal Local Approximation Spaces for Generalized Finite Element Methods with Application to Multiscale Problems. *SIAM Multiscale Modeling and Simulation*, 9:373–406, 2011.
- [14] M. Barrault, Y. Maday, N.C. Nguyen, and A.T. Patera. An ‘Empirical Interpolation’ Method: Application to Efficient Reduced-Basis Discretization of Partial Differential Equations. *C.R. Acad. Sci. Paris, Ser. I*, 339:667–672, 2004.
- [15] L. Borcea, Y. Gorb, and Y. Wang. Asymptotic approximation of the dirichlet to neumann map of high contrast conductive media. *SIAM MMS*, 12(4):1494–1532, 2014.
- [16] S. Boyaval. Reduced-basis approach for homogenization beyond periodic setting. *SIAM J. Multiscale Modeling and Simulation*, 7(1):466–494, 2008.
- [17] S. Brenner and L. Scott. *The Mathematical Theory of Finite Element Methods*. Springer-Verlag, New York, 2007.
- [18] M. Brezina, T. Manteuffel, S. McCormick, J. Ruge, G. Sanders, and P. Vassilevski. A generalized eigensolver based on smoothed aggregation (GES-SA)

- for initializing smoothed aggregation (SA) multigrid. *Numer. Linear Algebra Appl.*, 15(2-3):249–269, 2008.
- [19] F. Brezzi and M. Fortin. *Mixed and hybrid finite element methods*. Springer-Verlag, Berlin - Heidelberg - New York, 1991.
- [20] V. Calo, Y. Efendiev, J. Galvis, and G. Li. Randomized oversampling for generalized multiscale finite element methods. <http://arxiv.org/pdf/1409.7114.pdf>.
- [21] Saifon Chaturantabut and Danny C. Sorensen. Nonlinear model reduction via discrete empirical interpolation. *SIAM J. Sci. Comput.*, 32(5):2737–2764, 2010.
- [22] Y. Chen, L. Durlofsky, M. Gerritsen, and X. Wen. A coupled local-global upscaling approach for simulating flow in highly heterogeneous formations. *Advances in Water Resources*, 26:1041–1060, 2003.
- [23] C.C. Chu, I.G. Graham, and T. Hou. A new multiscale finite element methods for high-contrast elliptic interface problem. *Mathematics of Computation*, 79:1915–1955, 2010.
- [24] E. T. Chung, Y. Efendiev, G. Li, and M. Vasilyeva. Generalized Multiscale Finite Element Method for problems in perforated heterogeneous domains. *submitted*.
- [25] Eric T. Chung, Yalchin Efendiev, and Chak Shing Lee. Mixed generalized multiscale finite element methods and applications. *submitted*, 2014.
- [26] Eric T. Chung, Yalchin Efendiev, and Guanglian Li. An adaptive GMsFEM for high-contrast flow problems. *Journal of Computational Physics*, 273:54–76, 2014.
- [27] D. Knezevic D. Huynh and A. Patera. A static condensation reduced basis element method: approximation and a posteriori error estimation. *ESAIM: M2AN*, 47:213–251, 2013.

- [28] W. Dorfler. A convergent adaptive algorithm for poisson's equation. *SIAM J. Numer. Anal.*, 33:1106 – 1124, 1996.
- [29] M. Drohmann, B. Haasdonk, and M. Ohlberger. Reduced basis approximation for nonlinear parametrized evolution equations based on empirical operator interpolation. *J. Sci. Comput.*, 34(2):937–969, 2012.
- [30] Martin Drohmann, Bernard Haasdonk, and Mario Ohlberger. Reduced basis approximation for nonlinear parametrized evolution equations based on empirical operator interpolation. *SIAM J. Sci. Comput.*, 34(2):A937–A969, 2012.
- [31] M. Dryja. On discontinuous Galerkin methods for elliptic problems with discontinuous coefficients. *Comput. Methods Appl. Math.*, 3:76–85, 2003.
- [32] L. Durlofsky and J. F. Brady. Analysis of the brinkman equation as a model for flow in porous media. *Phys. Fluids*, 30:3329–3341, 1987.
- [33] W. E and B. Engquist. Heterogeneous multiscale methods. *Comm. Math. Sci.*, 1(1):87–132, 2003.
- [34] J. Eberhard and G. Wittum. A coarsening multigrid method for flow in heterogeneous porous media. In *Multiscale methods in science and engineering*, volume 44 of *Lect. Notes Comput. Sci. Eng.*, pages 111–132. Springer, Berlin, 2005.
- [35] Y. Efendiev and J. Galvis. A domain decomposition preconditioner for multiscale high-contrast problems. In Y. Huang, R. Kornhuber, O. Widlund, and J. Xu, editors, *Domain Decomposition Methods in Science and Engineering XIX*, volume 78 of *Lect. Notes in Comput. Science and Eng.*, pages 189–196. Springer-Verlag, 2011.

- [36] Y. Efendiev, J. Galvis, and T. Hou. Generalized multiscale finite element methods. *Journal of Computational Physics*, 251:116–135, 2013.
- [37] Y. Efendiev, J. Galvis, R. Lazarov, M. Moon, and M. Sarkis. Generalized Multiscale Finite Element Method. Symmetric Interior Penalty Coupling. *Journal of Computational Physics*, 255:1–15, 2013.
- [38] Y. Efendiev, J. Galvis, R. Lazarov, and J. Willems. Robust domain decomposition preconditioners for abstract symmetric positive definite bilinear forms. *ESAIM Math. Model. Numer. Anal.*, 46(5):1175–1199, 2012.
- [39] Y. Efendiev, J. Galvis, G. Li, and M. Presho. Generalized multiscale finite element methods. nonlinear elliptic equations. *Commun. Comput. Phys.*, 15:733–755, 2014.
- [40] Y. Efendiev, J. Galvis, G. Li, and M. Presho. Generalized multiscale finite element methods. oversampling strategies. *International Journal for Multiscale Computational Engineering*, 12(6):465–484, 2014.
- [41] Y. Efendiev, J. Galvis, and F. Thomines. A systematic coarse-scale model reduction technique for parameter-dependent flows in highly heterogeneous media and its applications. *Multiscale Model. Simul.*, 10:1317–1343, 2012.
- [42] Y. Efendiev, J. Galvis, and X.H. Wu. Multiscale finite element methods for high-contrast problems using local spectral basis functions. *Journal of Computational Physics*, 230:937–955, 2011.
- [43] Y. Efendiev, V. Ginting, T. Hou, and R. Ewing. Accurate multiscale finite element methods for two-phase flow simulations. *Journal of Computational Physics*, 220:155–174, 2006.

- [44] Y. Efendiev and T. Hou. *Multiscale Finite Element Methods: Theory and Applications*, volume 4 of *Surveys and Tutorials in the Applied Mathematical Sciences*. Springer, New York, 2009.
- [45] Y. Efendiev, T. Hou, and V. Ginting. Multiscale finite element methods for nonlinear problems and their applications. *Comm. Math. Sci.*, 2:553–589, 2004.
- [46] J. Galvis, G. Li, and K. Shi. A generalized multiscale finite element method for the brinkman equation. *Journal of Computational and Applied Mathematics*, 280:294–309, 2015.
- [47] B. Ganis, I. Yotov, and M. Zhong. A stochastic mortar mixed finite element method for flow in porous media with multiple rock types. *SIAM J. Sci. Comput.*, 33(3):1439–1474, 2011.
- [48] A.F. Gulbransen, V.L. Hauge, and K.-A. Lie. A multiscale mixed finite-element method for vuggy and naturally-fractured reservoirs. *SPE*.
- [49] N. Halko, P. G. Martinsson, and J. A. Tropp. Finding structure with randomness: probabilistic algorithms for constructing approximate matrix decompositions. *SIAM Rev.*, 53(2):217–288, 2011.
- [50] T. Hou and X.H. Wu. A multiscale finite element method for elliptic problems in composite materials and porous media. *J. Comput. Phys.*, 134:169–189, 1997.
- [51] T. Hughes, G. Feijoo, L. Mazzei, and J. Quincy. The variational multiscale method - a paradigm for computational mechanics. *Comput. Methods Appl. Mech. Engrg.*, 166:3–24, 1998.
- [52] D. B. P. Huynh, D. J. Knezevic, and A. T. Patera. A static condensation reduced basis element method: approximation and *a posteriori* error estimation. *ESAIM Math. Model. Numer. Anal.*, 47(1):213–251, 2013.

- [53] O. Iliev, R. Lazarov, and J. Willems. Variational multiscale finite element method for flows in highly porous media. *Multiscale Modeling & Simulation*, 9.4:1350–1372, 2011.
- [54] P. Jenny, S.H. Lee, and H. Tchelepi. Multi-scale finite volume method for elliptic problems in subsurface flow simulation. *J. Comput. Phys.*, 187:47–67, 2003.
- [55] L. Jiang and I.D. Mishev. Mixed multiscale finite volume methods for elliptic problems in two-phase flow simulations. *Commun. Comput. Phys.*, 11(1):19–47, 2012.
- [56] A.-R.A. Khaleda and K. Vafai. The role of porous media in modeling flow and heat transfer in biological tissues. *International Journal of Heat and Mass Transfer*, 46(26):4989–5003, 2003.
- [57] Y. Maday and E. Rønquist. A reduced-basis element method. *J. Sci. Comput.*, 17:447–459, 2002.
- [58] P.-G. Martinsson, V. Rokhlin, and M. Tygert. A randomized algorithm for the approximation of matrices. *Technical report, YALEU/DCS/TR-1361*.
- [59] K. Mekchay and R. H. Nochetto. Convergence of adaptive finite element method for general second order elliptic PDEs. *SIAM J. Numer. Anal.*, 43:1803–1827, 2005.
- [60] B. P. Muljadi, J. Narski, A. Lozinski, and P. Degond. Non-conforming multiscale finite element method for stokes flows in heterogeneous media. part I: methodologies and numerical experiments. *submitted*, 2014.
- [61] S. V. Nepomnyaschikh. Decomposition and fictitious domains methods for elliptic boundary value problems. In *Fifth International Symposium on Domain*

- Decomposition Methods for Partial Differential Equations (Norfolk, VA, 1991)*, pages 62–72, Philadelphia, PA, 1992. SIAM.
- [62] N. C. Nguyen. A multiscale reduced-basis method for parameterized elliptic partial differential equations with multiple scales. *J. Comp. Phys.*, 227(23):9807–9822, 2008.
 - [63] N. C. Nguyen, G. Rozza, D. B. P. Huynh, and A. T. Patera. Reduced basis approximation and a posteriori error estimation for parametrized parabolic PDEs: application to real-time Bayesian parameter estimation. In *Large-scale inverse problems and quantification of uncertainty*, Wiley Ser. Comput. Stat., pages 151–177. Wiley, Chichester, 2011.
 - [64] J.M. Nordbotten and P.E. Bjørstad. On the relationship between the multi-scale finite-volume method and domain decomposition preconditioners. *Comput. Geosci.*, 12(3):367–376, 2008.
 - [65] P. Popov, G. Qin, L. Bi, Y. Efendiev, R. Ewing, Z. Kang, and J. Li. Multiscale methods for modeling fluid flow through naturally fractured carbonate karst reservoirs. In *Proceedings of the SPE Annual Technical Conference and Exhibition*, 2007. SPE 110778.
 - [66] A. Quarteroni, G. Rozza, and A. Manzoni. Certified reduced basis approximation for parametrized partial differential equations and applications. *Journal of Mathematics in Industry*, 1:3, 2011.
 - [67] B. Rivière. Discontinuous Galerkin methods for solving elliptic and parabolic equation. *SIAM*, 35, 2008.
 - [68] G. Rozza, D.B.P Huynh, and A.T. Patera. Reduced basis approximation and a posteriori error estimation for affinely parametrized elliptic coercive partial

- differential equations. application to transport and continuum mechanics. *Arch. Comput. Meth. Engrg.*, 15(3):229–275, 2008.
- [69] Timo Tonn, K. Urban, and S. Volkwein. Comparison of the reduced-basis and POD *a posteriori* error estimators for an elliptic linear-quadratic optimal control problem. *Math. Comput. Model. Dyn. Syst.*, 17(4):355–369, 2011.
- [70] F. J. Valdes-Parada, J. A. Ochoa-Tapia, and J. Alvarez-Ramirez. On the effective viscosity for the darcy-brinkman equation. *Physica A: Statistical Mechanics and its Applications*, 385(1):69 – 79, 2007.
- [71] M.F. Wheeler, T. Wildey, and I. Yotov. A multiscale preconditioner for stochastic mortar mixed finite elements. *Comput. Methods Appl. Mech. Engrg.*, 200(9-12):1251–1262, 2011.
- [72] M.F. Wheeler, G. Xue, and I. Yotov. A multiscale mortar multipoint flux mixed finite element method. *ESAIM Math. Model. Numer. Anal.*, 46(4):759–796, 2012.
- [73] X. Xie, J. Xu, and G. Xue. Uniformly-stable finite element methods for darcy-stokes-brinkman models. *Journal of Computational Mathematics*, 26:437–455, 2008.